

# Charge carrier dynamics at organic interfaces for polymer photovoltaics

THÈSE N° 6638 (2015)

PRÉSENTÉE LE 3 JUILLET 2015

À LA FACULTÉ DES SCIENCES DE BASE  
GROUPE DE DYNAMIQUE PHOTOCHEMIE  
PROGRAMME DOCTORAL EN PHOTONIQUE

ÉCOLE POLYTECHNIQUE FÉDÉRALE DE LAUSANNE

POUR L'OBTENTION DU GRADE DE DOCTEUR ÈS SCIENCES

PAR

**Mariateresa SCARONGELLA**

acceptée sur proposition du jury:

Prof. O. Martin, président du jury  
Prof. J.-E. Moser, Prof. N. R. Banerji, directeurs de thèse  
Prof. C. Silva, rapporteur  
Prof. S. C. Hayes, rapporteur  
Prof. F. Carbone, rapporteur



ÉCOLE POLYTECHNIQUE  
FÉDÉRALE DE LAUSANNE

Suisse  
2015

*A mio padre*



*“Che accade al sapere di un uomo di scienza quando questi s'innamora, si ammala, invecchia o muore? Un pregiudizio tenacemente radicato nella nostra cultura ci induce a ravvisare facilmente un nesso fra una poesia e il dolore o la felicità di chi l'ha composta, e a ritenere invece che una formula matematica o una legge fisica abbiano poco a che vedere con la vita del loro autore o scopritore. Ma anche la formula che dice una forza che tiene l'universo non sarebbe nata, come la lirica, senza quel processo creativo che non è separabile dall'avventura esistenziale del suo scopritore e che, pur non condizionandone la validità scientifica, illumina il più vasto significato culturale della formula stessa, ciò che essa vuol dire per il mondo e per gli uomini.”*

(C. Magris, presentazione a “Ludwig Boltzmann: Una Passione Scientifica” di G. Zanarini)



# Table of Contents

Abstract.....	v
Riassunto.....	vii
<b>CHAPTER ONE Introduction.....</b>	<b>1</b>
<b>1.1 Introduction .....</b>	<b>2</b>
<b>1.2 Outlook on Renewable Energy .....</b>	<b>2</b>
<b>1.3 Objectives of the Thesis .....</b>	<b>5</b>
<b>1.4 Introduction to Conjugated Polymers .....</b>	<b>6</b>
<b>1.5 Radiation-Matter Interactions .....</b>	<b>9</b>
<b>1.6 Charge Carriers in Neat Polymers: Generation and Properties.....</b>	<b>10</b>
<b>1.7 Charge Generation in Polymer: Fullerene Blends .....</b>	<b>14</b>
1.7.1 From Double-Layer to Bulk-Heterojunction Solar Cells.....	14
1.7.2 Charge Generation in the Bulk Heterojunction .....	16
1.7.2.1 <i>Exciton Diffusion</i> .....	16
1.7.2.2 <i>The Free Charge-Generation Process</i> .....	18
1.7.3 Recombination Phenomena in BHJ Blends.....	26
<b>1.8 Investigated Polymers .....</b>	<b>27</b>
<b>1.9 References.....</b>	<b>32</b>
<b>CHAPTER TWO Experimental.....</b>	<b>39</b>
<b>2.1 Spectroscopic Techniques: General Introduction .....</b>	<b>40</b>
<b>2.2 Transient Absorption Spectroscopy (TAS) .....</b>	<b>40</b>
2.2.1 Experimental Apparatus for TAS.....	44
2.2.1.1 <i>The Femtosecond Laser</i> .....	45
2.2.1.2 <i>Generation of the Pump Pulses</i> .....	45
2.2.1.3 <i>Generation and Detection of the Probe Pulses</i> .....	50
2.2.2 Experimental Settings and TAS Data Treatment .....	53
<b>2.3 THz Time Domain Spectroscopy.....</b>	<b>55</b>
2.3.1 Introduction: Why use THz Spectroscopy? .....	55
2.3.1.1 <i>Experimental Layout</i> .....	56
<b>2.4 References.....</b>	<b>64</b>
<b>CHAPTER THREE A Detailed Study of Charge Generation in One- and Two-Phase Microstructures of pBTTT:PCBM.....</b>	<b>67</b>
<b>3.1. Introduction .....</b>	<b>68</b>
<b>3.2. Experimental Methods.....</b>	<b>70</b>
3.2.1. Sample preparation details .....	70
3.2.2. TA spectroscopy: experimental conditions.....	70

3.2.3. Fluorescence up-conversion spectroscopy .....	71
<b>3.3. Steady-State Spectra of the 1:1 and 1:4 Blends .....</b>	<b>72</b>
<b>3.4. Transient Absorption Results of Neat pBTTT Films .....</b>	<b>74</b>
<b>3.5. Charge Generation in pBTTT:PCBM Blends.....</b>	<b>75</b>
3.5.1. Charge generation in the 1:1 blend (540 nm and 390 nm) .....	75
3.5.2. Charge generation in the 1:4 blend (540 nm and 390 nm) .....	80
<b>3.6. Stark effect in the TA data of the 1:1 and 1:4 Blends.....</b>	<b>82</b>
3.6.1. Theoretical background about the Stark effect .....	82
3.6.2. Assignment of the electro-absorption signal (1:1 blend) .....	83
3.6.3. Evolution of the EA signature in the 1:1 blend (540 nm) .....	86
3.6.4. EA in the 1:1 blend for 390 nm and 540 nm excitation .....	87
3.6.5. Evolution of the EA signature in the 1:4 blend .....	88
<b>3.7. Fluorescence Spectroscopy Results.....</b>	<b>89</b>
<b>3.8. Conclusion .....</b>	<b>90</b>
<b>3.9. Appendix - Theoretical Methods .....</b>	<b>91</b>
3.9.1. Electrostatic Simulations.....	91
3.9.2. Analysis of the TA Dynamics: Global Fit Procedure .....	95
<b>3.10. References.....</b>	<b>9</b>

## **CHAPTER FOUR Charge Generation in Two- and Three-Phase Microstructures of pBTTT:PCBM with Partial or Predominant Phase-Separation.....**

<b>4.1. Introduction .....</b>	<b>102</b>
<b>4.2. Experimental Methods.....</b>	<b>104</b>
4.2.1. Sample preparation details .....	104
4.2.2. TA spectroscopy: experimental conditions.....	104
<b>4.3. Steady-State Spectra of the Studied Samples .....</b>	<b>104</b>
<b>4.4. Charge Generation Studied by TA Spectroscopy.....</b>	<b>106</b>
4.4.1. Partially intercalated blends.....	106
4.4.2. Predominantly phase-separated samples.....	110
<b>4.5. Evolution of the Electro-Absorption at 630 nm.....</b>	<b>112</b>
<b>4.6. Conclusion .....</b>	<b>116</b>
<b>4.7. References.....</b>	<b>118</b>

## **CHAPTER FIVE Charge Generation in PBDTPD:PCBM Blends: A Comparison between TA and THz Time-Domain Spectroscopy.....**

<b>5.1 Introduction .....</b>	<b>120</b>
<b>5.2 Experimental Methods.....</b>	<b>122</b>
5.2.1 Sample preparation details .....	122
5.2.2 TA and THz spectroscopy .....	123

<b>5.3 Steady State Absorption Spectra .....</b>	<b>123</b>
<b>5.4 Charge Generation Studied by TA Spectroscopy .....</b>	<b>125</b>
5.4.1 TA results for neat PBDTTPD films.....	125
5.4.2 TA results for PBDTTPD:PCBM blends .....	125
<b>5.5 Results from THz Time Domain Spectroscopy .....</b>	<b>131</b>
5.5.1 Neat PBDTTPD: THz dynamics of excitons.....	132
5.5.2 Photoconductivity spectra of neat PBDTTPD films .....	135
5.5.3 Delayed charge generation in PBDTTPD:PCBM .....	139
5.5.4 Photoconductivity spectra of PBDTTPD:PCBM .....	142
<b>5.6 Conclusions .....</b>	<b>148</b>
<b>5.7 References.....</b>	<b>150</b>
<b>CHAPTER SIX Conclusions .....</b>	<b>155</b>
<b>CURRICULUM VITAE.....</b>	<b>161</b>
<b>Acknowledgements.....</b>	<b>165</b>





# Abstract

The increased energy demand and the importance to find renewable energy resources have been addressed by a scientific effort to improve the power conversion efficiency of organic solar cells. In particular, polymer-based solar cells have experienced a great increase in power conversion efficiency, which recently reached a value over 10%. The possibility to further improve the performance of polymer-based solar cells has encouraged the research to have a close look at the key parameters, which play an important role in the mechanism of charge generation. Specifically, the photo-physical processes and the time scales involved in converting excitons to charges are still poorly understood. Also, the microscopic origin and the nature of the driving force allowing interfacial electron-hole pairs to become free charges and the role played by the sample microstructure in a bulk heterojunction have to be clarified. We have used transient absorption spectroscopy, which provides information about the excited states dynamics with  $<100$  fs time resolution, and THz time domain spectroscopy, which is additionally able to distinguish between bound and free charges and to bring insight to local mobility with a  $< 300$  fs time resolution. We have excited our samples at different wavelengths in order to be able to selectively excite mainly the polymer or the fullerene.

In **Chapter 3**, we present transient absorption measurements for a polymer known for good packing, long-range ordering and high mobility: pBTTT. We have investigated neat pBTTT and pBTTT blended with PCBM, either in 1:1 weight ratio (one-phase microstructure) presenting an intermixed co-crystal phase between polymer and PCBM, or in 1:4 weight ratio (two-phase microstructure) having the intermixed phase and neat fullerene regions. We found that charges are promptly generated in the 1:1 blends, but mostly recombine geminately, while the presence of neat fullerene domains (1:4 blends) is a driving force for free charge generation.

In **Chapter 4**, we present the study of additional pBTTT:PCBM blends, obtained using additives of different lengths and in different quantity. In contrast to the previous 1:1 and 1:4 microstructures, there is now a neat polymer and fullerene phase, and an intermixed phase (three-phase microstructure), or the blend is predominately phase separated (two-phase microstructure). We show that prompt charge generation occurs mainly in the intermixed phase, while the presence of neat polymer domains leads to

delayed exciton dissociation and reduces the yield of charge generation. Neat polymer and fullerene domains contribute nevertheless to the spatial separation of electron-hole pairs.

Finally, in **Chapter 5**, we present the transient absorption and THz investigation of a donor-acceptor co-polymer (PBDTTPD) in the neat phase and blended with PCBM in 1:2 weight ratio. The blend has a three-phase microstructure, consisting of neat amorphous polymer aggregates, amorphous intermixed regions, and neat fullerene domains. Differently from the pBTTT:PCBM systems, the presence of large (8 nm) polymer domains in PBDTTPD:PCBM is not an obstacle to the generation of charges, since the delocalized excitons efficiently dissociate with a 1 ps time constant. The delayed charge separation was also observed by THz-time domain spectroscopy at very low fluence.

**Keywords:** Conjugated polymers, polymer:fullerene blends, THz time-domain spectroscopy, transient absorption, morphology, electron transfer.

# Riassunto

La crescente richiesta nel settore energetico e l'importanza di trovare fonti di energia rinnovabile ha focalizzato lo sforzo della ricerca scientifica sul miglioramento della efficienza di conversione fotovoltaica delle celle solari organiche. In modo specifico, l'efficienza di conversione fotovoltaica delle celle solari costituite da materiale attivo a base polimerica, ha raggiunto un grande aumento che recentemente tocca valori del 10%. La possibilità di ottimizzare ulteriormente le performance delle celle solari polimeriche ha spinto la ricerca ad approfondire i parametri fondamentali che giocano un ruolo determinante nel meccanismo di generazione di carica. In modo specifico, i meccanismi foto-fisici e i tempi caratteristici coinvolti nel processo di generazione di carica a partire dagli eccitoni non sono stati ancora compresi in modo approfondito. Inoltre, ci sono aspetti, come l'origine microscopica e la natura della forza che permette ad una coppia elettrone-lacuna formatasi all'interfaccia di evolvere in carica "libera" all'interno di una *bulk heterojunction*, che meritano una comprensione approfondita. In questo lavoro, si è utilizzata la "*Transient Absorption Spectroscopy*", una tecnica di caratterizzazione ottica ultraveloce, in grado di restituire informazioni sulla dinamica di generazione di carica con una risoluzione temporale di 100 fs. La seconda tecnica sperimentale applicata è il "*THz-time domain spectroscopy*", che è in grado di dare informazioni complementari e di distinguere tra cariche legate e carica "libera" e di indicarci il valore della mobilità di carica con una risoluzione temporale  $< 300$  fs. I campioni studiati sono stati eccitati con due lunghezze d'onda differenti per poter eccitare selettivamente il polimero e il fullerene.

Nel **Capitolo 3**, sono presentati i risultati relativi ad un polimero (pBTTT) che gode delle proprietà di essere un polimero ad alta mobilità di carica, di avere ottime proprietà di *packing* e di organizzarsi in modo da formare una struttura prevalentemente ordinata. Si sono studiati campioni preparati con il polimero puro, e campioni preparati con una miscela di polimero e fullerene (PCBM) con differente rapporto in massa 1:1 (microstruttura ad una fase) e 1:4 (microstruttura a due fasi). Il primo presenta una microstruttura monofasica costituita dal fullerene intimamente intercalato tra le catene polimeriche (regione intermista) il secondo presenta invece una morfologia bifasica costituita da una regione intermista e da una regione formata solo da molecole di fullerene. Le misure di caratterizzazione spettroscopica nel

visibile hanno messo in evidenza che nella microstruttura monofasica la maggior parte della carica si ricombina mentre nella microstruttura bifasica la presenza di regioni di fullerene ha un ruolo determinante nella dinamica di generazione di carica libera.

Nel **Capitolo 4**, vengono presentati i risultati relativi alla caratterizzazione di altri composti del polimero studiato nel capitolo precedente. Questi sono stati preparati aggiungendo additivi nella miscela liquida di fullerene e polimero. L'aggiunta di additivi con differente lunghezza e in diversa quantità permette di creare microstrutture differenti da quelle studiate nel **Capitolo 3**:

- una struttura a tre fasi differenti (costituite da una regione di polimero puro una regione di fullerene pura e una regione intermista)
- una microstruttura composta prevalentemente da due fasi: una regione di polimero puro e una regione di fullerene puro.

I risultati della caratterizzazione spettroscopica mettono in evidenza che la carica viene generata all'interno della fase intermista. Le regioni di polimero e di fullerene puro hanno da un lato un ruolo determinante nel processo di generazione di carica libera, dall'altro contribuiscono a diminuire la quantità netta di carica generata poiché molti eccitoni generati in questa regione si ricombinano e non riescono a raggiungere l'interfaccia per potersi separare.

Nel **Capitolo 5**, si mostrano i risultati di misure messe a punto su un polimero donore-accettore: PBDTPD. Sono state misurate due microstrutture: la fase pura e quella ottenuta attraverso la miscela con il fullerene in un rapporto di massa di 1:2. Il polimero è stato misurato con due tecniche di caratterizzazione ottica differenti che sondano la dinamica di generazione di carica nel range di frequenze del visibile (*Transient Absorption Spectroscopy*) e del THz (*time domain spectroscopy*). La microstruttura del campione è costituita da tre fasi: una regione pura di polimero in fase amorfa, una regione intermista piuttosto amorfa e una regione di fullerene pura. A differenza della dinamica di generazione di carica osservata nelle regioni pure di pBTTT, la presenza di regioni di puro polimero non ostacola il processo di generazione di carica ma, al contrario, lo agevola grazie alla peculiare proprietà di delocalizzazione degli eccitoni che si formano in questo polimero. Questa caratteristica permette agli eccitoni di raggiungere più facilmente l'interfaccia con il fullerene di separarsi in carica libera. Questo processo di generazione di carica ritardata, avviene in un picosecondo e la sua dinamica è stata osservata anche nella regione di frequenza dei THz.

**Parole chiave:** polimeri coniugati, polimero:fullerene blends, spettroscopia THz risolta in tempo, transient absorption, morfologia, trasferimento di elettroni.



# **CHAPTER ONE**

## **Introduction**



## 1.1 Introduction

## 1.2 Outlook on Renewable Energy

The demands for energy at the global level are constantly increasing. As fossil fuels (oil and natural gas) are still widely used to produce energy, there are many problems associated with their use as the primary energy resource. The consumption of these energy sources causes damage to the environment because they release CO<sub>2</sub>, methane, and NO<sub>2</sub>, into the atmosphere, consequently increasing global warming.

As of today, the potential availability of fossil fuels is roughly  $6.9 \cdot 10^{15}$  Kgs and the subsequent consumption would be  $< 10^{14}$  KWh/year. Consequently, on the one hand, if we continue to use fossil fuels alone, we will run out of them in about 100 years (1). On the other hand, the sun is an inexhaustible renewable power source. The first devices to use solar power to convert energy into electricity were inorganic solar cells. Inorganic silicon based photovoltaic cells are used due to their efficiency and consistency. However, the cost of the fabrication of inorganic photovoltaic cells is high, thus making it less attractive. In addition, the cost of converting solar energy into solar electricity, obtained from the most widely commercialized crystalline silicon devices, is still not competitive with the price of fossil fuels.

In recent years, a new generation of organic and hybrid photovoltaics (dye-sensitized, small molecule and polymer solar cells) has offered a cost-efficient alternative to inorganic devices (silicon, cadmium telluride, copper indium gallium selenide, gallium arsenide)(2),(3),(4),(5),(6),(7). An organic solar cell is made up of an active layer sandwiched between two different electrodes. One electrode is transparent so that light can enter through the cathode and reach the active layer, as shown in Figure 1.1. Generally, a glass substrate (which can be replaced by a flexible substrate for large-scale applications) and a transparent ITO electrode are used.

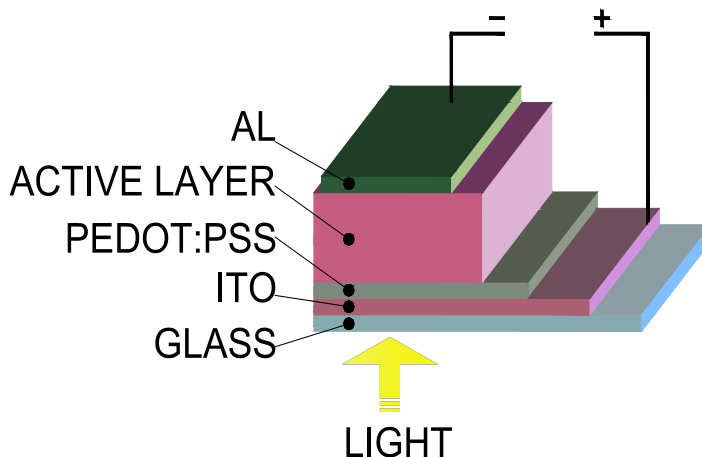


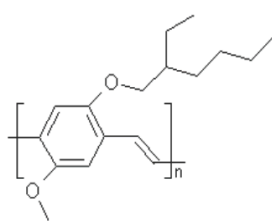
Figure 1.1 Device structure for an organic solar cell.

Light absorption and charge carrier generation occur inside the active layer and then the charges are transported to the electrodes and collected into the external circuit. The PEDOT:PSS layer helps transport the positive charge carriers (holes), smoothens the ITO surface and prevents it from diffusing into the active layer. In some cases, the negative electrons are transported through an additional  $\text{TiO}_2$  layer, which has the role of blocking the holes from reaching the aluminium anode (8). One type of new generation organic photovoltaics uses conjugated polymers in the active layer (9). This organic material has many attractive features that makes it suitable for solar cells, such as an extremely high optical absorption coefficient which offer the possibility for the production of very thin solar cells. Polymer solar cells are also cheap, easy to process, solid-state, lightweight and flexible.

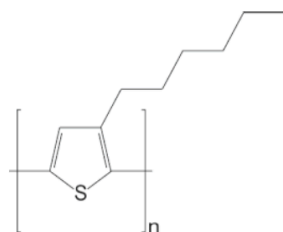
A typical polymer-based solar cell has an active layer that is composed of the polymer as an electron donor (D) and a fullerene derivative as an electron acceptor (A), spontaneously forming an interpenetrating network at the nanoscale called bulk heterojunction (BHJ).

Conjugated polymers have been successfully used in light-emitting devices, transistors, photo-detectors and organic solar cells because they can combine semiconducting properties, high optical absorption in the visible and near-IR range (the band gap of these materials ranges from 1 to 4 eV) and plastic-like mechanical properties. In Figure 1.2, some examples of classic conjugated polymers and some newer types (donor-acceptor copolymers made up of an electron rich unit and an electron poor unit) are shown.

### Classic Conjugated Polymers

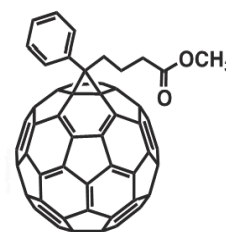


MEH-PPV



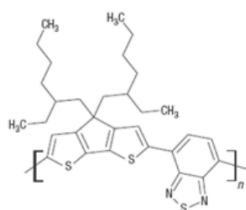
P3HT

### Fullerene Acceptor

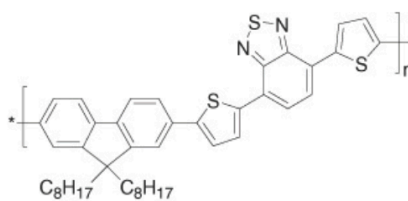


PCBM

### Donor-Acceptor Copolymers



PCPDTBT



APFO-3

Figure 1.2 Molecular structure of different types of polymers and PCBM.

Conjugated polymers were discovered towards the end of the last century; for their discovery and investigation, Alan J. Heeger, Alan G. MacDiarmid and Hideki Shirakawa were awarded the Nobel Prize in Chemistry in 2000. The power conversion efficiency (PCE) for this class of photovoltaics has taken a very encouraging leap forward over the past few years, increasing from around 3% in 2001 to 8.3% in 2010, till reaching 12% in 2013 (10) as shown in the table below.

	1986	2000	2004	2010	2012	2013
<b>Efficiency (%)</b>	1 (Kodak)	2 (U.Cambrige)	4 (Groningen)	8 (Solarmer)	10 (UCLA)	12 (Mitsubishi)

The performance of these conjugated-polymer solar cells can be improved by controlling the optoelectronic properties of the materials, by optimizing the phase-morphology of the BHJ blends, and also by studying the photo-physical processes (charge generation, carrier mobility) that occurs after their photo excitation (8).

### 1.3 Objectives of the Thesis

My research in the development of polymer solar cells is pointing in the direction of improving the efficiency of free charge generation. Although in the last few years many improvements have been made, there still remains much to be learned about the photo-physical mechanisms and models that could connect the efficiency of a solar cell with the microstructure and specific phase-morphology of the BHJ. On the one hand, recently the process of diffusion of excitons and their migration to the polymer/fullerene interface has been investigated, but the ensuing mechanism and the time scale of free-charge generation still needs to be better understood. On the other hand, the main problem with the photo physics of a polymer description is the difficulty in finding a general theoretical model that enables us to describe the structure, the mechanism of exciton transfer and its dissociation, because the polymer is missing a periodic three-dimensional lattice structure.

To understand better the charge generation and recombination processes in conjugated polymer films and polymer: fullerene blends, in this thesis work I have compared the information obtained from two different complementary time resolved experiments: transient absorption spectroscopy (TAS) and THz-time domain spectroscopy.

Specifically I have studied the photo physical properties (exciton dissociation, free charge generation, charges transport) changing the microstructure and phase-morphology of different BHJ samples. This has been experimentally obtained by changing the weight ratio of the polymer and the PCBM ([6,6]-phenyl C<sub>60</sub> butyric acid methyl ester) and by using fatty acid methyl ester processing additives during the film preparation.

I have compared two different polymers with different structures and properties: one with a more crystalline solid-state structure poly(2,5-bis(3-tetradecyl-thiophen-2-yl)thieno[3,2,-b]thiophene) (**pBTTT**), and the other one being a donor-acceptor co-polymer with more amorphous structure (poly(benzo[1,2-b:4,5-b']dithiophene-*alt*-thieno[3,4-c]pyrrole-4,6-dione) (**PBDTPD**). The pBTTT polymer displays long-range ordering and the mobility of positive charges is very high (it is used in transistors because it is so good for transporting charges). Moreover its ordered structure enables us to easily control the phase-morphology in blends with PCBM. I have compared the charge generation mechanism in six different microstructures,

as discussed in detail in Chapter 3. I have also studied the charge generation processes of the donor-acceptor co-polymer PBDTTPD. I show some TAS results on the neat and blended sample and compare these results with those that I obtained with THz time-domain spectroscopy (Chapter 4).

## 1.4 Introduction to Conjugated Polymers

Conjugated polymers (CP) are composed of carbon atom chains in which there are alternating single covalent bonds ( $\sigma$  bonds) and double bonds, consisting of a  $\sigma$  bond and a  $\pi$  bond (for example trans-polyacetylene) as shown in Figure 1.3. Polyacetylene is a very attractive material for determining theoretical properties of a one-dimensional polyconjugated system.

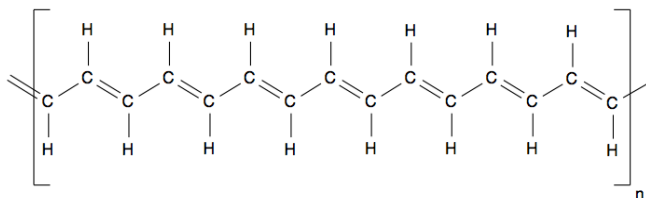


Figure 1.3 Chemical structure of trans-polyacetylene.

The  $\pi$  bonds are characterized by delocalized electrons where  $\pi$  electrons can move along the length of the polymer; this is the reason why it is called conjugated. The conjugation length is the real range of delocalization of  $\pi$  electrons within the molecules.

The carbon atom has four electrons in the most external shells and the electronic configuration is  $2s 2p_x 2p_y$ . These orbitals can mix to form a hybrid orbital in the following way:  $2s 2p_x 2p_y \Rightarrow 3(sp^2) p_z$  (11). The  $(sp^2)$  is coming from the mixing of a  $s$  and  $p$  orbital and forms the  $\sigma$  bonds, whereas the  $p_z$  orbital makes the  $\pi$  bonds. The high mobility of  $\pi$  electrons results in an easy deformability of their distribution by application of an electric field, but the polarizability does not follow the applied field linearly (11).

The delocalization of the  $\pi$  electrons makes the CP similar to semiconductors in some aspects: in the CP, due to the effect of the alternation of single and double bonds in the one-dimensional long chain, the molecules have a completely filled valence band made up of  $\pi$  bonding orbitals, corresponding

to the highest occupied molecular orbital (HOMO), and an empty conduction band corresponding to the unoccupied molecular orbital (LUMO), made up of the  $\pi^*$  antibonding orbitals (Figure 1.4); the two bands are separated by an energy gap,  $E_g$ , typically between 1 and 4 eV.

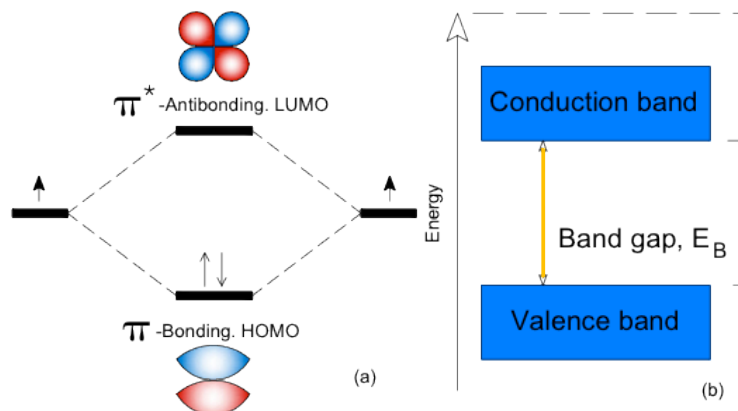


Figure 1.4 a) Energy level schema of a conjugated polymer, showing bonding orbitals HOMO and antibonding LUMO b) Diagram showing semiconductor energy band.

The structure of the CP, where each carbon atom is linked to adjacent ones by only two covalent bonds, is particularly prone to distortion. This induces the formation of one or two states whose energy levels fall in the gap and causes energy absorption values to be even lower than the band gap energy. The presence of these energy states are associated with quasi-particles of different nature, such as solitons, polarons, bipolarons and polaron excitons. Figure 1.5a shows a defected alternation in a polymer chain, a soliton, and the corresponding state in the associated energy gap. Polarons, which can be thought of as two consecutive defects stabilized by a single charge, are associated with two states in the energy gap, equidistant from the valence and conduction bands (Figure 1.5b); in the presence of a high concentration of polarons, distortions occur in the chain, which causes the formation of bipolaron (Figure 1.5c): in this case one of the levels in the gap is occupied by two charges of the same sign (the configuration is made stable by the polarization of the medium). Finally, when the CP absorbs photons with energy higher than that of the gap, excitons are formed, i.e. electron-hole pairs, also called as neutral polaron excitons because they move together and induce spacial relaxation (Figure 1.5d) (12) (13).

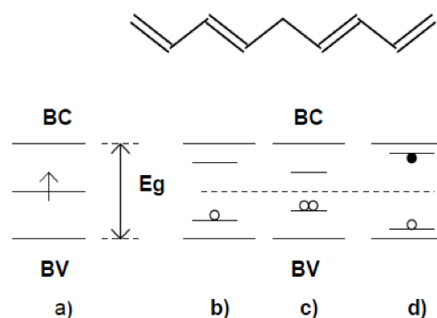


Figure 1.5 Top: schematic representation of a lack of alternation in a polymer chain. Bottom: electronic states in the energy gap: a) a soliton; b) a polaron; c) a bipolaron; d) a polaron exciton (13).

A different approach in understanding the photophysics of a CP, comes from a molecular description of organic materials. Excitons are neutral wavelike excitations made up of an electron and a hole attracted to each other by an electrostatic Coulomb force (14). They are characterized by an exciton binding energy, which is the energy required to separate the electron and hole into free charges (15, 16).

As in organic materials the free charges are almost absent so the electron screening is very low. This property, which is characteristic of organic semiconductors leads to very low relative dielectric constant of the medium ( $\epsilon_r = 2-4$ ). Hence the generated excitons in organic materials are tightly bound with an exciton binding energy much higher with respect to the thermal energy at room temperature ( $K_B T = 25$  meV): experimental measurements have shown that the exciton binding energy in these materials can assume values between 0.5 eV and 1.1 eV (for an electron and a hole with a distance of 1 nm) (14), which are much higher respect to the thermal energy at room temperature. These excitons, called Frenkel excitons, are localized on a single molecule.

The opposite situation occurs in an inorganic semiconductor. In fact, as the relative dielectric constant in these materials, is very high (around 12), the excitons are weakly bound (Wannier-Mott excitons).

The exciton binding energy is thus lower than the thermal energy at room temperature, primarily creating free charge carriers as a result of photoexcitation after light absorption. These excitons are delocalized over a distance larger than the crystal lattice constant.

## 1.5 Radiation-Matter Interactions

As light is electromagnetic radiation, it transports energy when it passes through space and when it hits a material. Atoms or molecules in the medium can absorb a photon when the energy of the single photon corresponds to the characteristic energy difference between the ground state and one of the allowed excited states of the sample. When this process takes place, there is a transition of an electron to a higher excited state.

The absorption spectrum shows a distribution of energies at which different transitions occur in the medium. If there are many transitions of different energies, a broad spectrum will be produced.

The Beer-Lambert law evaluates the number of photons absorbed by the material in terms of the incident radiation ( $I_0$ ) when the transmitted radiation ( $I$ ) is measured.

$$I(\lambda) = I_0(\lambda) * 10^{-\varepsilon(\lambda)cd} \quad 1)$$

where  $\varepsilon(\lambda)$  represents the molar extinction coefficient (in  $M^{-1}cm^{-1}$ ),  $c$  is the molar concentration of the absorbing species ( $M$ ), and  $d$  is the path length of the medium (in  $cm$ ). The optical-density value ( $OD$ ) is defined by the following equation:

$$A = \varepsilon(\lambda) * c * d = -\log\left(\frac{I(\lambda)}{I_0(\lambda)}\right) \quad 2)$$

The formula shows the absorbance dependence upon the molar extinction coefficient, the concentration of absorbing species and the sample thickness ( $d$ ). Different materials are characterized by specific molar-extinction coefficients. In particular, in organic semiconductor films, a linear absorption coefficient ( $\alpha$ ) is usually introduced. It is defined as  $\alpha = \varepsilon(\lambda) * c$ .

The typical value of the absorption coefficient in organic semiconductors is above  $10^5 cm^{-1}$  in the visible spectrum. Due to this property, a very thin, organic layer is enough to harvest solar energy in a very efficient way.



## 1.6 Charge Carriers in Neat Polymers: Generation and Properties

After the primary photo-excitation, an exciton is created in neat conjugated-polymer films (without the addition of fullerene), but typically there is also a small fraction of charge carriers formed. The main problematic of the photo physics of neat polymers not only concerns the mechanism of charge generation in the absence of an acceptor to provide a driving force to break the exciton, but also concerns the nature and properties of excitons and charges immediately after photo-excitation. The excitonic picture of neat polymer films is still not clear and is the object of significant debate. Even though the yield of charge generation has been reported to be very low for the neat polymer phase (<10%), in the last few years good efficiency (around 30%) has been reported for charge generation in P3HT films with semi-crystalline structure. Hence, the influence of the microstructure (crystalline, semicrystalline or completely amorphous) in the process of charge generation is important also for the formation of polarons in the neat phase. On the one hand there is a theory that describes the polymer as a one-dimensional semiconductor. In this situation, the light absorption directly creates the electrons and holes after their localization (12). On the other hand, there is an approach where the polymers are seen as macromolecules: in this approach, the excitons are already created as bound charges (17),(18). It has been found that the “excited state” nature depends on disorder, on the microstructure in the polymer and on the time scale at which we take the snapshot of the moment after the first photo-excitation (19).

There is some experimental evidence that the primary photo-excited species in neat polymer chains are *delocalized* excitons, as supported by Banerji at al. (20). Localization occurs on the 100-200 fs time scale, through different mechanisms of relaxation: structural distortion in the polymer chain, coherent energy transfer between chromophore units, electronic relaxation to a more localized state, as shown in Figure 1.6 (19).



Figure 1.6 Description of the evolution of the polymer excited state in a single chain: initial delocalization, localization of excited states, in the end hops between chromophores. Adapted with permission from (21).

There are several studies (by Sundstroem et al. (22) and Scholes et al. (23)) confirming a primary delocalization of the excited state directly after photo excitation. This delocalization is followed by self-localization into neutral and charged species. Sundstroem et al. show that the structural lattice-relaxation of polymer chains plays a fundamental role in the process of self-localization. They observe a faster ( $<100$  fs) depolarization of anisotropic time-resolved fluorescence and transient absorption data for MEH-PPV polymer chains with a higher conjugation length and initially more delocalized excitons, with respect to the partially conjugated polymer (22). Scholes et al. corroborate this theory by observing that, on the same polymer (MEH-PPV), the ultrafast decay of the photon echo-peak shift, can be explained by rapid dynamic localization of the excitation, due to the relaxation of the electronic structure of the polymer (23),(21).

Also, Banerji et al. have shown experimental evidence of exciton localization in less than 200 fs: they have recorded time-resolved emission spectra of P3HT in chlorobenzene solution and in spin cast films, with a fluorescence up-conversion set-up. Indeed, already at 0.2 ps, the emission spectrum is red-shifted with respect to the absorption spectra as shown in the Figure 1.7 (19). The shape of the 0.2 ps emission spectra is also different from the absorption spectra: this means there is a different nature of the emitting state or a decrease of inhomogeneity.

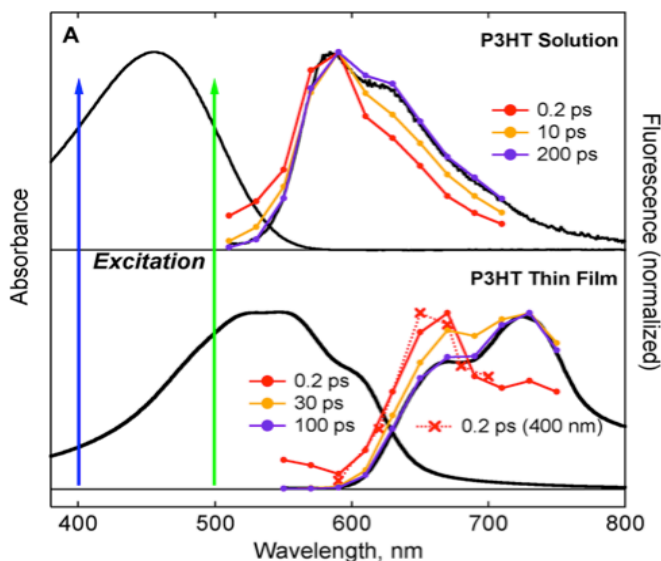


Figure 1.7 Steady state absorption and emission spectra (black curves) and time-resolved emission spectra of P3HT in solution and in thin film. After exciting at 500 nm (dots) and 400 nm (crosses)(19).

Besides the nature of the primary photo-excited species, the mechanism of the photo-generation process of charges - although in small yield - in neat polymers without any applied electric field, is still under debate. Heeger et al., using transient absorption spectroscopy with a visible-pump and an IR-probe, found experimental evidence of polaron generation in a neat polymer, as shown in Figure 1.8 (24).

The spectra show the ultrafast formation of polarons (defined as charges coupling to a structural distortion) in neat PPV and MEH-PPV. They report that the process of direct photo-induced charge carrier generation in neat conjugated polymers occurs on a time scale of 100 fs.

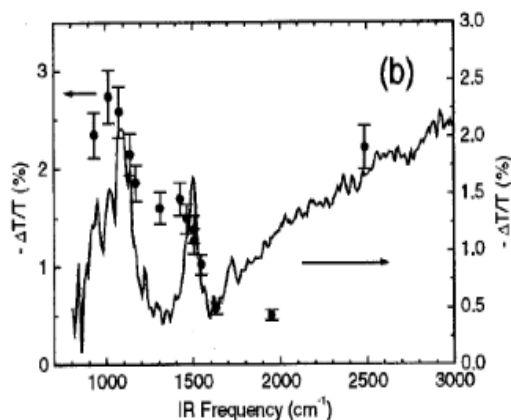


Figure 1.8 Transient IRAV spectrum for a neat MEH-PPV (24).

Other experimental measurements on neat polymer films have shown that it is also possible to generate polarons dissociating the exciton by a two-step excitation mechanism. C. Silva et al. have experimentally demonstrated this process using photoinduced absorption measurements in a model electroluminescent- $\pi$  polymer (25). The mechanism involves a primary photoexcitation followed by a second “push” excitation bringing the exciton on high-energy singlet states. In this condition the exciton can overcome the binding energy and dissociate to a polaron.

However, the process of charge generation is still debated. The measurements of Banerji et al. support the important role of initial delocalization in the process of free-charge generation, after high-energy excitation in neat polymers (20). Upon localization, the primary excitation either becomes a neutral exciton or forms polarons. A contribution to the formation of the polarons can come, also, from the asymmetry in the system (such as the interface of amorphous and crystalline domains in P3HT) or from an intramolecular charge transfer character in donor-acceptor co-polymers (19).

Moreover, several mechanisms for indirect charge generation in neat polymers have been suggested:

- As a by-product of bimolecular exciton-exciton annihilation at high optical excitation densities: this is an excitation intensity dependent mechanism that leads to the relaxation of one exciton into the ground state, whereas the other one is promoted to a higher electronic state from where it is possible to dissociate to a polaron pair (26).
- Hot exciton dissociation: with this mechanism, the exciton dissociation is due to the thermal bath generated by phonons that are emitted upon relaxation of the initial excited state into a bound exciton (27).
- Exciton dissociation at defect sites (28).
- Disorder-mediated charge generation: the disorder can come from different situations, such as fluctuations in the molecular position and the orientation of polymer chromophores, thus changing the molecular interactions and activating low-energy transitions. Or it can cause the breaking down of the polymer chain into smaller chromophores, as shown in Figure 1.9 (19).

The disorder leads to wave function localization and prevents

delocalization in the primary photo-excitation.

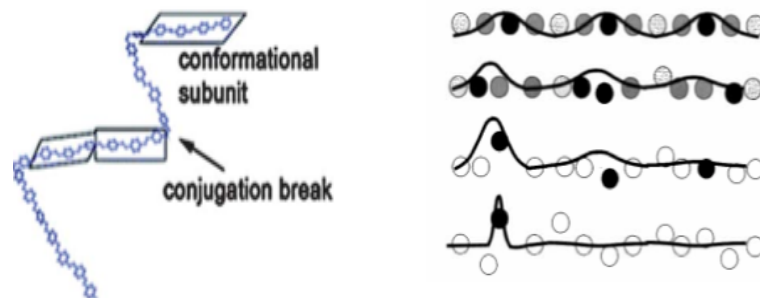


Figure 1.9 Picture of a MEH-PPV chain interrupted into chromophores by conjugation breaks according to the model by Scholes et al.(21). A representation of the exciton localization phenomenon due to disorder (16).

## 1.7 Charge Generation in Polymer: Fullerene Blends

The mechanism of free charge (polaron) generation in polymer: fullerene blends is one of the most debated question in the literature of organic solar cells. In order to better understand all the problematics correlated to this mechanism, let us introduce before the concept of a bulk heterojunction.

### 1.7.1 From Double-Layer to Bulk-Heterojunction Solar Cells

The first organic solar cells were made using a single layer between two electrodes: light was able to enter inside the organic solid through the transparent electrode, creating the excitons that diffuse in the polymer layer. As the absorption coefficient of organic materials is very high, the layer thickness usually has a very small dimension, around 100 nm. The power-conversion efficiency of these solar cells, however, is not good ( $\ll 1\%$ ). This is caused by the fact that the excitons have a diffusion length of 1-10 nm, which is shorter than the device thickness, and because the excitons are strongly bound and only split in a very small yield (see Chapter 1.5). Hence it is more difficult to create free charges using only the polymer phase and the probability of exciton and charge recombination is very high (29).

To improve this situation, double-layer structure solar cells were introduced: they were made by sandwiching an organic material as a donor and a

fullerene as acceptor material (30). In this situation, the excitons are created in the polymer and can travel toward the interface, where they can separate more easily because there are two materials with different ionization potentials. The potential difference is higher than the binding energy of the excitons, thus enabling their dissociation. Nevertheless, the power-conversion efficiency of these solar cells is still not optimum, because the contact surface of the donor and acceptor materials is very small and the exciton-diffusion length is still too short with respect to the thickness of the photoactive layer.

In order to achieve a higher performance in the more recent organic solar cells, the bulk heterojunction (BHJ) concept has been used. Here, the donor (polymer) and acceptor (typically PCBM) are blended together in an interpenetrating network that forms by spontaneous phase segregation when they are cast as a thin film from a common solution. This enables to have a larger D/A surface area for efficient charge separation and a good charge transport in the separate polymer and fullerene phases. After the charges are separated, the holes travel through the polymer, and the electrons travel through the fullerene. A power-conversion efficiency of 10 % has been reached by using polymer: fullerene BHJs with optimized microstructure (obtained by processing control such as annealing) (31).

The most common image of the bulk heterojunction, which can be found in most textbooks, is like the one shown on the left of Figure 1.10. It is comprised of just two phases, the polymer and the fullerene. The real microstructure (phase morphology) of the photoactive layer does not always correspond to this picture, because the fullerenes can intercalate between amorphous or crystalline polymer chains, forming an intimately mixed phase. In fact, the microstructure can correspond for example to a situation in which there are pure fullerene domains and a fully intermixed phase (two phase microstructure), or to a three-phase morphology with pure fullerene domains, neat polymer domains and the intermixed phase. The manipulation of the microstructure is possible either (i) by using additives, which can prevent the intercalation of the polymer and the fullerene, (ii) by using different weight ratios between the polymer and fullerene in order to obtain different phase morphologies, (iii) by using post-processing techniques such as thermal annealing. The manipulation of the microstructure allows obtaining an optimized morphology with improved performances in terms of photon absorption, exciton dissociation and charge transport.

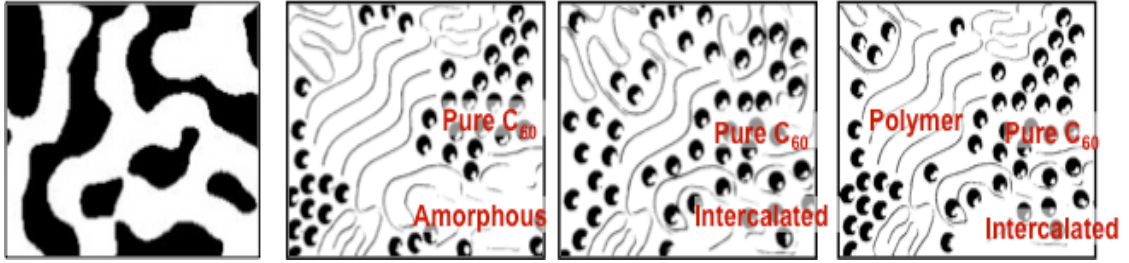


Figure 1.10 Different phase microstructures in polymer: fullerene blends: a) shows the classical cartoon of the bulk heterojunction, b) c) d) show three different phase morphologies obtained using different polymers, polymer: fullerene weight ratios or by optimizing the film processing with additives.

## 1.7.2 Charge Generation in the Bulk Heterojunction

In this thesis, I studied the process of charge generation in polymer: fullerene BHJ blends without the application of an external electric field.

Typically, the process of charge generation in a bulk heterojunction solar cell is comprised of different steps, illustrated in Figure 1.11:

- Light absorption (primary photo-excitation)
- Exciton diffusion to the donor-acceptor interface, in competition with exciton recombination
- Exciton dissociation at the interphase (CS - charge separation)
- Charge transport (electrons through the acceptor and holes through the donor), in competition with charge recombination

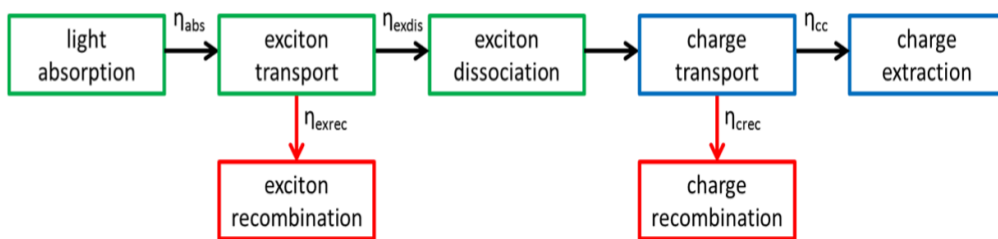


Figure 1.11 Scheme of charge generation (32).

### 1.7.2.1 Exciton Diffusion

We now discuss each of these steps in detail. We begin with the **exciton diffusion** to the interface. One of the most used models in the literature, to describe the process of exciton diffusion in a neat polymer, is the Förster

resonance energy transfer theory (32). Besides, the hopping model has also been recently suggested for exciton and charge transport (33). Some problematic aspect in studying the process of exciton diffusion, comes from the contradiction found between theoretical and experimental results connecting the time scale of charge generation and the distance travelled by the exciton to an interface. In fact, according to the exciton diffusion coefficients published in the literature, the diffusion length of an exciton has a value from 2 to 10 nm. For example, P3HT has an exciton diffusion length of 2.5-8.5 nm (34). In blends with a 10 nm-polymer size region, the time the exciton needs to reach an interface with the fullerene is on the 10-100 ps time scale. However, there are some experimental results showing that charges are generated in the first 100 fs after excitation, but on this time scale, the excitons would diffuse by 0.1 -0.3 nm (according to typical exciton diffusion coefficients) and not by 10 nm (34, 35). It is therefore unclear how an important population of free charges would already be produced after 100 fs (36-39).

The discrepancy between the experimental results and theoretical previsions has been widely discussed and is still the object of much hypothetical interpretation. Banerji et al. have used ultrafast photoluminescence up-conversion spectroscopy in their proposed model, which explains the commonly observed ultrafast charge generation process (<100 fs), in spite of the fact that diffusion of excitons to an interface is much slower. It supposes that the separation of the charges occurs immediately after excitation, during the initial delocalization of the photo-induced exciton and before its self-localization (40). Taking into account this initial delocalization, CS at the donor-acceptor interface can occur directly from the delocalized exciton. The delocalization increases the probability of having free charges, as the binding energy of the electrons and holes is reduced. Hodgkiss et al., using photoluminescence spectroscopy, confirm that most of the charges are generated on an ultrafast time scale and that the free charges are created through delocalized hot excitons. This is also supported by theoretical calculation of Kaake et al.; they suggest that the initial exciton delocalization arises from the uncertainty principle applied to ultrafast time scales (41, 42). Apart from exciton delocalization, the microstructure plays an important role in sustaining ultrafast charge generation. As will be discussed further in this thesis, CS on the 100 fs time scale can occur in intermixed regions, where no exciton diffusion is necessary.



### 1.7.2.2 The Free Charge-Generation Process

We now focus on the second step in the path to generating free charges after the diffusion of the excitons to the donor-acceptor interface. The process of free-charge generation in the blended solar-cell films is different from the one described for the neat polymer. After the photo-generation of an exciton and its diffusion, an exciton dissociates when it reaches the interface between the donor (polymer) and the acceptor (fullerene) (6), thus creating a bound electron-hole pair. The fullerene has a high ionization potential and a good ability to transport electrons (10). The intermediate step, in which the electrons and holes are still bound together across the interface, forming a state in-between an exciton and the free charges, is often called a **charge transfer (CT) state**. The latter can be found in the ground state ( $CT_0$ ) or in an excited state ( $CT_n$ ). According to some recent models, the charges in hot  $CT_n$  states can become free charges (polarons) or, if the driving force at the D-A interface is not enough to dissociate the bound electron-hole pair, they can relax to a state in which the charges remain bound ( $CT_0$ ). From this state they can undergo geminate recombination. A scheme of this situation is shown in Figure 1.12. It has been estimated that the binding energy in the CT state would be around 250-500 meV, two orders of magnitude higher than the thermal energy at room temperature (25 meV) (43).

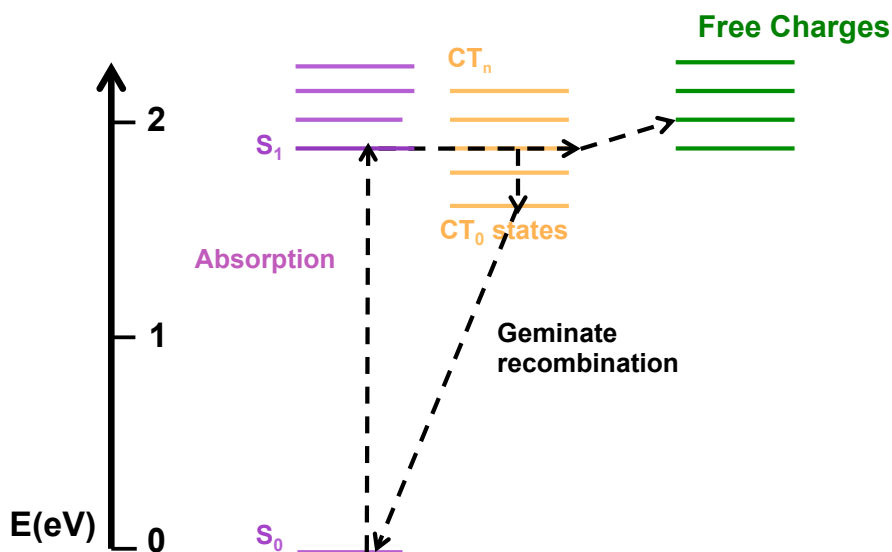


Figure 1.12 Scheme of free charge generation: an exciton is created and after it can go through the  $CT_n$  states and relax to  $CT_0$ , or become a free charge.

The main problem in the current research is understanding how the charge-pairs separate and become free charges (polarons), without the application of any external electric field (intrinsic free charges generation). The difference in energy of LUMO levels, between the donor and the acceptor, is usually insufficient for dissociating the excitons to free charges. Therefore, the research effort in the last few years has been toward designing a bulk heterojunction with optimal physical and chemical characteristics for the best charge-generation efficiency. In order to improve the efficiency of the free charge generation, it is necessary to improve the BHJ phase morphology, to better design the chemical structure of the donor polymers, and to understand the fundamental electronic processes of charge separation.

Until now, there has been much debate about the origin of free charges inside the blended materials. It has been suggested that to improve the probability of exciton dissociation, there are different aspects that could play an important role: for example the excess of excitation energy, the distribution of the density of states, the degree of the disorder at the donor-acceptor interface, the nanoscale mobility of excitons and charges, and the initial delocalization. The question, on one hand, is focused on understanding whether the best efficiency of free charge generation corresponds to a photo-physical pathway where the polarons are formed directly from cold (thermally equilibrated)(18) or hot excitons, or indirectly from a picture where the electron-hole pair has to go through the bound CT state before spatially dissociating. On the other hand, it is still not well understood what the origin of the driving force that enables the separation of the charges is, whether hot CT<sub>n</sub> states are really involved and what the role played by the microstructure is.

Hence the research is to understand which particular chemical-physical properties of polymer: fullerene blends - such as blend morphology, specific microstructure of the donor and the acceptor (crystalline or amorphous), length scale for interfacial charge separation, exciton diffusion, disorder at the D-A interface - need to be optimized in order to improve the charge generation yield and charge transport.

In the last few years, many models describing new experimental results have emerged. Among these, there is the famous Onsager-Braun type model. According to this model, after travelling to an interface, the exciton undergoes charge separation to a Coulomb bound charge-transfer state that relaxes in 100 fs to its lowest vibrational level (CT<sub>0</sub>). After 5 ns, the bound charges can

geminately recombine or completely separate into the polymer and fullerene phases (37). This model predicts that any change in the electric field and the temperature should increase the yield of free charges in fullerene: polymer blends. However, some experimental results do not reflect this previous prediction (37, 44). It has also been shown that Onsager-Braun model is based on the incorrect hypothesis that the process of generation and recombination (geminate recombination) follow exponential dynamics (45). Another model supports the hypothesis that the generation of free charges occurs directly after the excitons are dissociated (for example from hot delocalized  $CT_n$  states before relaxation), in a time less than 100 fs (37, 46). If bound charges in the  $CT_0$  state are formed by relaxation, they will recombine in about 2 ns and cannot be separated into free charges. The comparison between these two models is shown in Figure 1.13 (37).

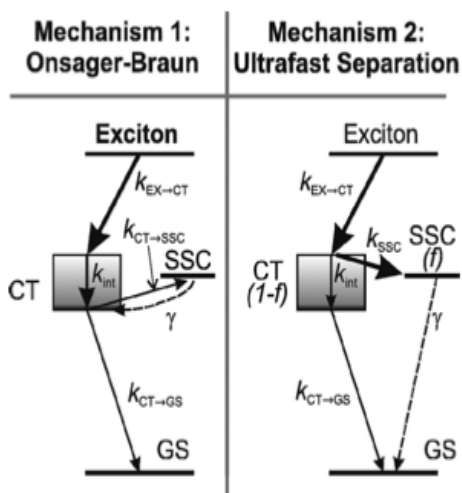


Figure 1.13 Two different models of charge generation and separation. CT= charge transfer state, SSC= spatially separated charges, GS=ground state (37).

In the general discussion about the nature of the driving force that determines the separation of charges, there are many and sometimes contrasting theories. The role of the excess excitation energy in efficient charge dissociation has been investigated by using different techniques. Lee et al., using photocurrent spectroscopy on polymer:fullerene blends, exciting the polymer with different pump-excitation energies and by directly exciting the CT states. They found that the free charges were generated directly from the relaxed  $CT_0$ -state without the necessity to go through any hot exciton or  $CT_n$  states. A schema of the model is presented in Figure 1.14 (47). The internal quantum yield of charge generation was found to be similar in both

experiments and independent of the excess excitation energy. Hence, they argue that the excess energy does not contribute significantly to the process of charge generation, whereas it is the intermediate CT states that, when directly excited, can increase the probability of having free charges, being the precursor of polarons. Also Vandewal et al., using electroluminescence and photo-thermal deflection spectroscopy, found similar results as Lee et al., in terms of the independence of the internal quantum yield on the excess excitation energy (48).

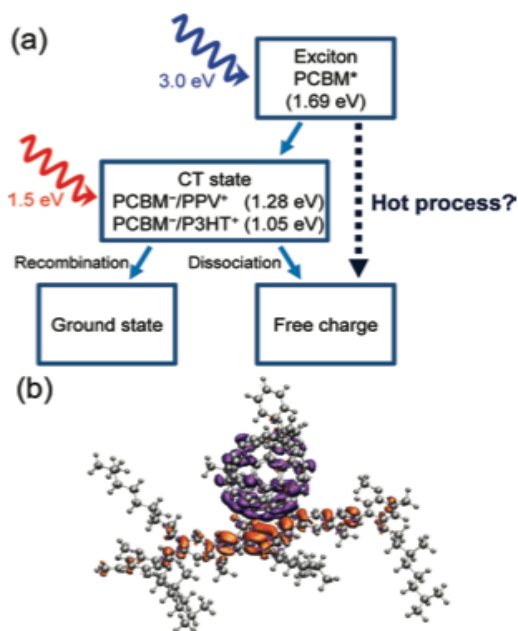


Figure 1.14 Conceptual scheme showing the two paths exploited in the experiment to have the charges dissociate: exciton dissociation after photoexcitation of the polymer with different energy or direct excitation of the CT states (47).

However the group of Lanzani et al. suggest a different result. In fact, using transient absorption spectroscopy with the probe in the IR regime (until 1500 nm) and pumping in the visible with different energy exceeding the energy gap of the polymer, they found an increase of the yield of charge dissociation when the pump energy was increased in a way that excites the higher-lying singlet states, as shown in Figure 1.15 (49). They suggest that the excess photon energy is exploited to achieve a higher degree of delocalization in hot  $CT_n$  states and this helps the probability of charge generation in the first 200 fs. They argue that the hot  $CT_n$  states are fundamental for charge dissociation.

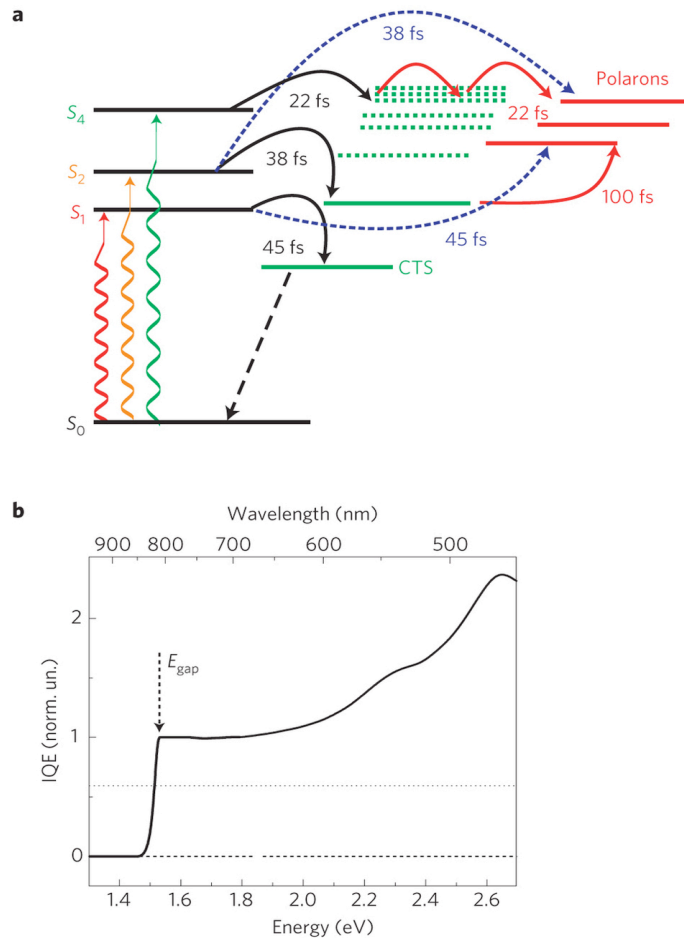


Figure 1.15 a) The effect of pump-excitation energy in the formation of polarons and CT states on the 200 fs time scale. b) shows the dependence of IQE (Internal Quantum Efficiency) on the pump-excitation energy b)(49).

Bakulin et al. have performed pump-push photocurrent experiments to study further the role of the CT states. They find that the driving force to overcome the Coulombic binding energy of the CT state comes from the delocalization of the hot charge-transfer states ( $CT_n$ ) populated within 100 fs. In their experiment, a second IR pump (called push) is exploited to bring the charges that are in the relaxed  $CT_0$  state back to the hot  $CT_n$ -excited states. In this situation, they found an increase of photocurrent. The mechanism is described in Figure 1.16 (50).

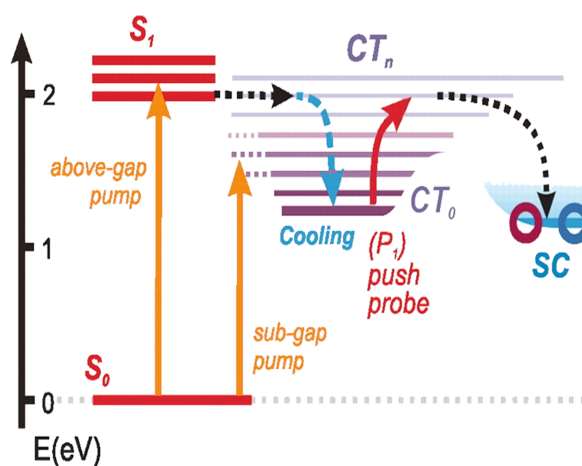


Figure 1.16 Scheme showing the pump-push-photocurrent experiments performed by the group of Friend at al.: Generation of free charges from delocalized CT<sub>n</sub> states (CT<sub>0</sub> is the lowest-lying level)(50).

These results are supported also by Dimitrov at al., who find that, when the photon energy above the energy gap is increased, even the double of the quantum yield of charges is obtained (51).

From the aforementioned results, the idea that emerges - about how to obtain the best efficiency of charge generation - is that the dissociation of the (possibly hot) intermediate interfacial CT states is an important step in the pathway of charge separation. Another important question is the time scale on which the charge separation occurs. There has been some research that strongly supports the idea that the free charges are generated on the ultrafast time scale, without well-defined intermediate CT state, directly from the excitons. Provencher et al., using femtosecond Raman spectroscopy, saw that the polarons can be generated on an ultrafast (< 50 fs) time scale, which confirms that the ultrafast dissociation of a non-equilibrium initial photo excited species is important in the process of charge generation. Moreover, Bittner and Silva elaborated a quantum calculation that describes how the exciton dissociates directly into free charges (52, 53). Laquai et al., using transient absorption spectroscopy, also conclude that the free charges are generated directly on the 100 fs time scale (54).

Another important aspect, which has still not been well developed and which is essential for developing a model of charge dissociation and for understanding the mechanism of free charge generation, is to find the

minimum distance of the electron-hole pair at which the binding energy between the hole and electron can overcome or become equal to thermal energy. Experimental results on this aspect were obtained by Gelinias at al.: they used transient absorption spectroscopy and observed the signature of the Stark effect in the spectra, due to the electric field produced by photo-generated electron-hole pairs at the donor-acceptor interphase and to their spatial separation with time. They find that the charges have to reach a distance of 4 nm within the first 100 fs in order to reduce the binding energy equal to thermal energy; if they do so in optimized blends, they can dissociate. Figure 1.17 shows the photophysics of charge generation at the interface, according to the situation described above (55).

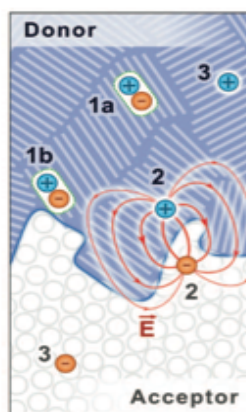


Figure 1.17 Photophysics of free charge generation: the excitation approaches the interface and starts to dissociate, creating an electric field detected in the experiment as a Stark effect (55).

Hodgkiss et al., confirming the previous result, also find that the electron-hole pair has to reach a distance of 4 nm before becoming free charges (43). In regard to the time in which this separation occurs, Friend et al. and Hodgekiss et al. suggest an ultrafast (100 fs) time scale. However, Gulbinas et al. find that the charges reach several nm in several ps, before they become free charges. They use a technique (electric-field induced second harmonic generation) that enables them to follow the electric-field dynamics and the drift of charge carriers. This technique is based on the same principle as the one used by Friends et al. (Stark effect), but the field that Gulbinas et al. use does not come directly from the charges at the interface, but is externally applied.

Another important question, which needs to be developed and well understood, is how the mechanism of free charge generation and

recombination depends on the sample's phase morphology (structural organization) and the specific microstructure of the donor and acceptor in the blends. The short-range packing, long-range ordering (crystalline or amorphous) and the arrangement of the acceptor and donor into different intermixed and neat phases, can be controlled during the sample processing, as has been already suggested (56). As discussed before, the microstructure of the BHJ is very complex. The amorphous or crystalline neat domains often coexist with a phase where the polymer and fullerene are intimately mixed. The different sample morphologies and the presence of crystallinity in the fullerene or polymer domains, change the way that free charges are generated and the time needed for this. It influences all the steps needed for the dissociation and transport of the charges.

One of the first works to highlight the importance of the microstructure for the efficiency of charge generation was performed by Muller et al. They studied the effect of the polymer: fullerene weight ratio and of the processing protocol on the exciton generation, its dissociation and the charge transport to the electrodes (57). Using thermal analysis, they found that the fullerenes have the ability to mix with the polymer (forming intimately mixed regions) and also to form large crystalline PCBM domains (at high fullerene content), which improves performance in terms of electron transport. The presence of the neat fullerene domains is also the key characteristic that improves the charge dissociation (58). They found that the electron affinity of the neat PCBM domains is high with respect to the fully intermixed phase, favouring the transport of the electrons out of the intermixed regions. This kind of morphology, with intermixed regions and neat fullerene domains, provides a strong driving force to enable the spatial charge separation while a fully intercalated microstructure leads to important geminate recombination (important population of the  $CT_0$  state) and impedes most charges from ever dissociating. Muller et al. also found that the control of intercalation, between the fullerene and polymer, is fundamental to the improvement of charge generation efficiency. They have used the pBTTT polymer, which is particularly suitable for enabling us to control the intercalation of fullerenes between polymer side chains. They found that the ratio that enables best performances is 1:4 by weight (because neat PCBM and intermixed regions co-exist), whereas in the 1:1 blend (only intermixed regions) they found that the charges recombine and never separate (57-59).

Finally, McGehee et al., using Monte Carlo simulations, have demonstrated that in order to improve the power conversion efficiency, the microstructure



should consist of three phases (polymer, fullerene and intermixed polymer/fullerene phase), with high local charge carrier mobility, and a long lifetime of the CT state. They find the optimal microstructure to have the least amount of recombination and highest yield of free charges. Specifically, they show that to have better performance in terms of charge generation, the concentration of PCBM has to be higher than the percolation threshold, hence enabling formation of neat PCBM regions and an efficient electron transport. Otherwise, the small fraction of PCBM completely intercalates with the polymer and acts as a trap, forcing charge recombination (60) (61-63).

### 1.7.3 Recombination Phenomena in BHJ Blends

The loss channel during free charge generation and charge extraction, which competes with the probability of obtaining free charges at the electrodes, is the recombination phenomenon. In order to function in solar cells, the charges have to reach the electrodes before recombination, within their lifetime. Recombination occurs when an electron and hole cannot separate because the driving force is not strong enough, or if they encounter during their transport to the electrodes. The equation that describes how the concentration of charge carriers changes due to their generation and recombination is as follows:

$$\frac{dn}{dt} = G_0 - k_r n - B_L np$$

Here,  $n$  and  $p$  are the concentrations of electrons and holes and  $G_0$  is the rate of charge carrier generation (64). In this equation, the term  $k_r$  represents the first order recombination, typically caused by geminate recombination, and the term  $B_L$  represents the second order recombination, typically caused by bimolecular recombination. These two recombinations are the main processes of charge recombination in the BHJ.

Geminate recombination occurs when the electron-hole pair formed by the dissociation of an exciton is recombining because it is strongly bound at the interface between the donor and acceptor in the heterojunction. This is the type of recombination expected in the CT state. We are sure to be in the presence of geminate recombination when, in the experiment, we observe that the dynamics are independent of excitation fluence (and there is a linear dependence of charge concentration on fluence). It has been suggested that

the time scale of geminate recombination is of the order of hundreds of ps to tens of ns (65, 66). It has been also demonstrated that geminate recombination depends on the initial charge mobility along the polymer chains and on the disorder at the interface. This dependency influences the probability of electron-hole pairs to escape geminate recombination in case of high local mobility. It has also been experimentally demonstrated that a specific microstructure of the BHJ favours geminate recombination: geminate recombination is typical for a microstructure with a very intimately intermixed donor-acceptor phase (50-52).

Bimolecular recombination refers to the recombination of two free charges from different initial excitons, if they encounter in the BHJ. The mathematical model describing this situation is the Langevin model (67). It takes into account the fact that the charges are produced statistically, independently of each other. The model shows that the bimolecular recombination depends upon the mobility of electrons and holes and on the initial charge density, both depending on the excitation flux. This means that, when we have very high fluence, the recombination probability increases and the dynamics of the bimolecular recombination evolves from the ns time scale (in real solar conditions) to the ps or even fs time scale (54, 68). In order to avoid artificial effects of bimolecular recombination on the dynamics measured by ultrafast spectroscopy experiments, we need to use very low fluences in our experiments (about  $10^{12}$  -  $10^{13}$  photons/cm<sup>2</sup>).

## 1.8 Investigated Polymers

In this thesis, I have studied different kinds of polymers: a donor-acceptor copolymer (PBDTTPD) and a homopolymer (pBTTT). The fact that the chemical characteristics of these polymers are different gives us the opportunity to understand how the charge generation dynamics depends on chemical structure.

In the last few years, the interest in donor-acceptor copolymers has increased, because the efficiency of organic solar cells based on them is much higher than for homopolymers (7-9%). The donor-acceptor copolymers are composed of an electron-donating moiety (D) and an electron poor moiety (A). The hybridization of their molecular orbitals introduces the peculiarity of causing a permanent dipole moment in the ground and/or excited states, thus

introducing intermolecular charge transfer character. The large spatial redistribution of electron density towards the acceptor moiety, when going from the ground to an excited state, implies a charge transfer transition. This characteristic contributes to the reduction of the band gap, thus enabling the red part of solar light to be harvested. Moreover, in comparison with classic homopolymers, the donor-acceptor co-polymers have additional characteristics: they have dipole moments in the excited states and undergo changes in intermolecular charge transfer character during excited-state relaxation. It has been shown that the internal charge transfer character in the excited state of a D-A co-polymer leads to short-lived delocalization and stimulates the formation of free charges (69, 70).

Specifically, I have studied the PBDTTPD donor-acceptor copolymer. Figure 1.18 shows the molecular structure and the steady-state spectra of neat PBDTTPD and the PBDTTPD:PCBM blend, synthesized for the first time in 2010 (71),(72). The PBDTTPD repeat unit consists of the benzodithiophene (BDT) electron-donating group and the thieno [3,4-c]pyrrole-4,6-dione (TPD) electron-withdrawing group. By optimizing the morphology, the power conversion efficiency in a 1 cm<sup>2</sup> solar-cell device of this blended polymer reaches a value of 8.5 % (73). The steady-state spectra of this polymer present some vibronic structure and there is a small Stokes shift. This is due to the fact that in the ground state and the excited state the polymer has a mostly planar backbone conformation (74, 75). This characteristic enables exciton delocalization over about 2 nm, thus favouring the exciton diffusion out of neat PBDTTPD domains; this has been also supported by some theoretical calculations (74).

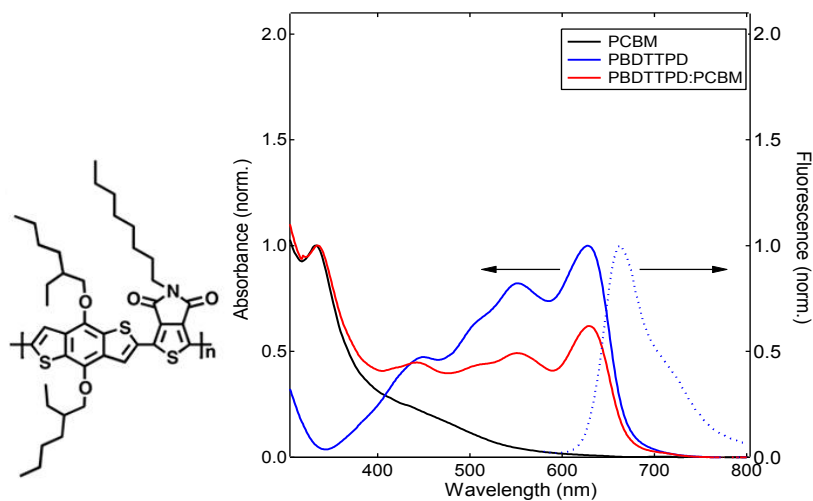


Figure 1.18 Molecular structure of PBDTTPD and the steady-state absorption spectra of the neat and blended polymer, as well as of PCBM (76).

It has been shown for PBDTTPD that it is less the internal charge transfer character that contributes to the good efficiency of charge generation, but rather the exciton delocalization over 2 nm that plays the main role in charge separation. This makes the polymer particularly appropriate for our studies of short-lived excited state delocalization.

The second polymer that I have studied was pBTTT. The pBTTT polymer is known for its excellent charge mobility in field-effect transistor devices (77-79). Even if they yield moderate power conversion efficiency in solar cells, pBTTT:fullerene blends are particularly suitable model systems for studying microstructural effects (80). Indeed, it has been shown that the fullerene molecules intercalate between the side-chains of ordered polymer domains, forming a well-defined co-crystalline phase, whereas excess fullerenes aggregate into relatively phase-pure clusters (58, 59, 80, 81). Thanks to this particular structure, the polymer has the capability to host the fullerenes inside “cavities”. In this way, it is possible to obtain a single intermixed phase by using a 1:1 weight ratio of polymer and fullerene, or to obtain two phases (intermixed and neat fullerene) by using a 1:4 weight ratio. The molecular structure of the pBTTT polymer and schematic representations of different pBTTT:PCBM microstructures are shown in Figure 1.19.

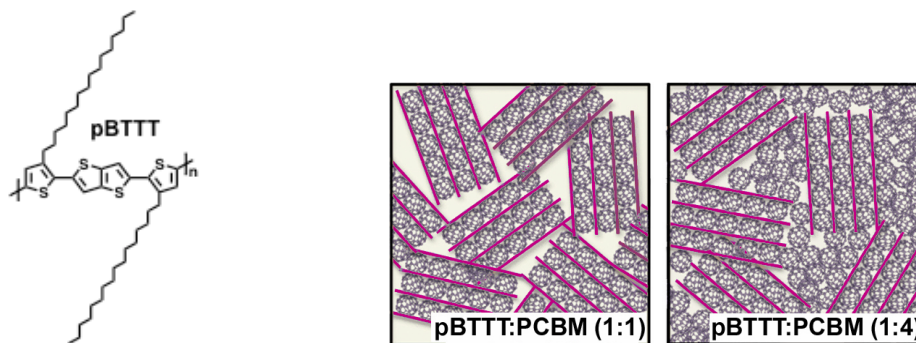


Figure 1.19 Molecular structure of pBTTT and schematic representation of the polymer:fullerene bulk-heterojunction microstructures in the 1:1 blend (middle) and 1:4 blend (right).

This peculiarity of pBTTT gives us the possibility to target different microstructures either by changing the ratio between the fullerene and the polymer, or by using some processing additives to prevent the intercalation of the fullerenes between the polymer side chains. We have recently shown that the co-crystal formation can be controlled (from a fully intermixed, to a partially intercalated, to a predominantly non-intercalated microstructure), by using fatty-acid methyl esters of different lengths as additives. The intercalation of the fullerenes inside the polymer chains increases the lamellar distance with respect to the neat polymer. This specific property of the polymer is highlighted in Figure 1.19, which shows the X-ray diffractograms of the neat polymer and the 1:1 blend (containing only co-crystalline phase). It is possible to see the peak shift due to the increased distance between the lamellae. An intermediate situation is shown for the green and blue curves where, thanks to the additive, the donor and the acceptor are respectively partially intercalated or predominantly phase-separated.

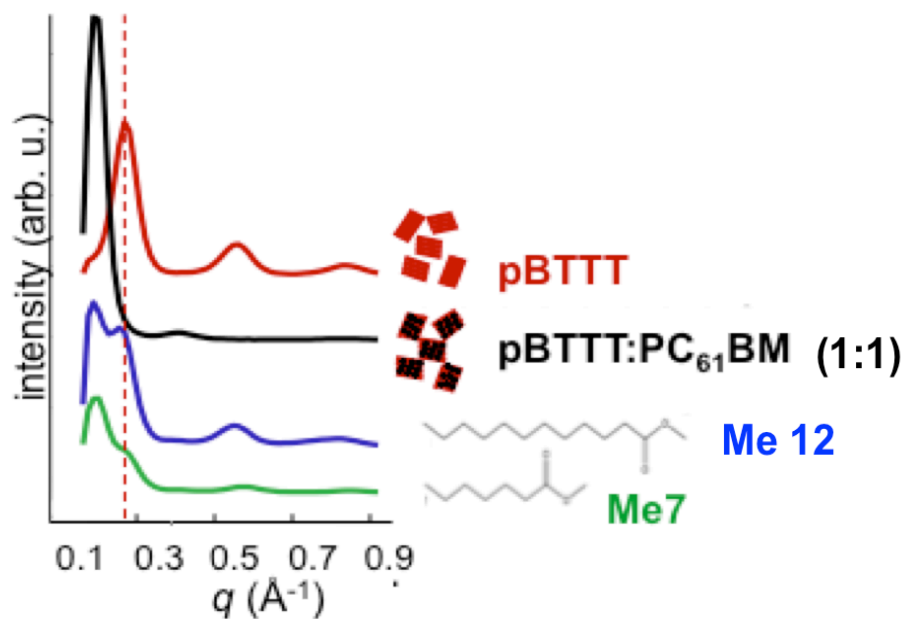


Figure 1.19 X-ray diffractograms of neat pBTTT and pBTTT:PCBM blends with different microstructures: the red curve is the neat sample, the black curve is the 1:1 blend (fully intercalated), and the blue and the green curves are the 1:1 blends obtained with the processing additives (Me 7 and Me 12, as shown in the Figure) of different alkyl chain lengths: Me7 yields a partially intercalated microstructure and Me12 leads to a predominantly phase-separated microstructure (82).

## 1.9 References

1. N. Armaroli, V. Balzani, "The future of energy supply: challenges and opportunities" *10.1002/anie.200602373* 1433-7851 (Wiley-VCH Verlag GmbH & Co. KGaA, 2007).
2. M. Gratzel, Photoelectrochemical cells. *Nature (London, U. K.)* **414**, 338 (2001).
3. N. Sakai, R. Bhosale, D. Emery, J. Mareda, S. Matile, Supramolecular n/p-heterojunction photosystems with antiparallel redox gradients in electron- and hole-transporting pathways. *J. Am. Chem. Soc.* **132**, 6923 (2010).
4. B. Walker *et al.*, Nanoscale Phase Separation and High Photovoltaic Efficiency in Solution-Processed, Small-Molecule Bulk Heterojunction Solar Cells. *Adv. Funct. Mater.* **19**, 3063 (2009).
5. J. E. Bullock, R. f. Kelley, M. R. Wasielewski, Self-assembled nanostructures for organic photovoltaics. *PMSE Prepr.* **96**, 805 (2007).
6. B. C. Thompson, J. M. J. Frechet, Polymer-fullerene composite solar cells. *Angew. Chem., Int. Ed.* **47**, 58 (2008).
7. C. J. Brabec, Organic photovoltaics: technology and market. *Sol. Energy Mater. Sol. Cells* **83**, 273 (2004).
8. G. Li *et al.*, High-efficiency solution processable polymer photovoltaic cells by self-organization of polymer blends. *Nat. Mater.* **4**, 864 (2005).
9. T. Surek, Crystal growth and materials research in photovoltaics: progress and challenges. *J. Cryst. Growth* **275**, 292 (2005).
10. C. J. Brabec, N. S. Sariciftci, J. C. Hummelen, Plastic solar cells. *Adv. Funct. Mater.* **11**, 15 (2001).
11. W. Barford, Electronic and Optical Properties of Conjugated Polymers. *Oxford University Press, New York*, (2005).
12. A. J. Heeger, S. Kivelson, J. R. Schrieffer, W. P. Su, Solitons in conducting polymers. *Rev. Mod. Phys.* **60**, 781 (1988).
13. O. C. K.P.C. Vollhardt, W. H. Freeman Company, NY, 1987.
14. G. Lanzani *et al.*, Photophysics of conjugated polymers: The contribution of ultrafast spectroscopy. *Phys. Status Solidi A* **201**, 1116 (2004).
15. J. L. Bredas, J. Cornil, A. J. Heeger, The exciton binding energy in luminescent conjugated polymers. *Adv. Mater. (Weinheim, Ger.)* **8**, 447 (1996).
16. G. Lanzani, "The Photophysics behind Photovoltaics and Photonics". *Wiley-VHC*, (2012).
17. H. Bassler *et al.*, Excitons in  $\alpha$ -conjugated polymers. *Synth. Met.* **135-136**, 377 (2003).
18. I. G. Scheblykin, A. Yartsev, T. Pullerits, V. Gulbinas, V. Sundstroem, Excited State and Charge Photogeneration Dynamics in Conjugated Polymers. *J. Phys. Chem. B* **111**, 6303 (2007).

19. N. Banerji, Sub-picosecond delocalization in the excited state of conjugated homopolymers and donor-acceptor copolymers. *Journal of Materials Chemistry C* **1**, 3052 (2013).
20. N. Banerji *et al.*, Breaking Down the Problem: Optical Transitions, Electronic Structure, and Photoconductivity in Conjugated Polymer PCDTBT and in Its Separate Building Blocks. *J. Phys. Chem. C* **116**, 11456 (2012).
21. I. Hwang, G. D. Scholes, Electronic Energy Transfer and Quantum-Coherence in  $\alpha$ -Conjugated Polymers. *Chem. Mater.* **23**, 610 (2011).
22. A. Ruseckas *et al.*, Ultrafast depolarization of the fluorescence in a conjugated polymer. *Phys. Rev. B: Condens. Matter Mater. Phys.* **72**, 115214/1 (2005).
23. X. Yang, T. E. Dykstra, G. D. Scholes, Photon-echo studies of collective absorption and dynamic localization of excitation in conjugated polymers and oligomers. *Phys. Rev. B: Condens. Matter Mater. Phys.* **71**, 045203/1 (2005).
24. P. B. Miranda, D. Moses, A. J. Heeger, Ultrafast photogeneration of charged polarons in conjugated polymers. *Phys. Rev. B: Condens. Matter Mater. Phys.* **64**, 081201/1 (2001).
25. C. Silva *et al.*, Efficient exciton dissociation via two-step photoexcitation in polymeric semiconductors. *Phys. Rev. B: Condens. Matter Mater. Phys.* **64**, 125211/1 (2001).
26. G. J. Denton, N. Tessler, M. A. Stevens, R. H. Friend, Optical response of conjugated polymers excited at high intensity. *Synth. Met.* **102**, 1008 (1999).
27. D. M. Basko, E. M. Conwell, Theory of hot exciton dissociation in conjugated polymers. *Synth. Met.* **139**, 819 (2003).
28. F. Paquin *et al.*, Charge separation in semicrystalline polymeric semiconductors by photoexcitation: is the mechanism intrinsic or extrinsic? *Phys. Rev. Lett.* **106**, 197401/1 (2011).
29. G. A. Chamberlain, Organic solar cells: a review. *Sol. Cells* **8**, 47 (1983).
30. C. W. Tang, Two-layer organic photovoltaic cell. *Appl. Phys. Lett.* **48**, 183 (1986).
31. S. H. Park *et al.*, Bulk heterojunction solar cells with internal quantum efficiency approaching 100%. *Nat. Photonics* **3**, 297 (2009).
32. K. Feron, W. J. Belcher, C. J. Fell, P. C. Dastoor, Organic solar cells: understanding the role of Forster resonance energy transfer. *Int J Mol Sci* **13**, 17019 (2012).
33. H. Nemeč, P. Kuzel, V. Sundstroem, Charge transport in nanostructured materials for solar energy conversion studied by time-resolved terahertz spectroscopy. *J. Photochem. Photobiol., A* **215**, 123 (2010).
34. P. E. Shaw, A. Ruseckas, I. D. W. Samuel, Exciton diffusion measurements in poly(3-hexylthiophene). *Adv. Mater. (Weinheim, Ger.)* **20**, 3516 (2008).



35. A. J. Lewis *et al.*, Singlet exciton diffusion in MEH-PPV films studied by exciton-exciton annihilation. *Org. Electron.* **7**, 452 (2006).
36. J. Piris *et al.*, Photogeneration and Ultrafast Dynamics of Excitons and Charges in P3HT/PCBM Blends. *J. Phys. Chem. C* **113**, 14500 (2009).
37. I. A. Howard, R. Mauer, M. Meister, F. Laquai, Effect of Morphology on Ultrafast Free Carrier Generation in Polythiophene:Fullerene Organic Solar Cells. *J. Am. Chem. Soc.* **132**, 14866 (2010).
38. R. A. Marsh, J. M. Hodgkiss, S. Albert-Seifried, R. H. Friend, Effect of Annealing on P3HT:PCBM Charge Transfer and Nanoscale Morphology Probed by Ultrafast Spectroscopy. *Nano Lett.* **10**, 923 (2010).
39. D. G. Cooke, F. C. Krebs, P. U. Jepsen, Direct observation of sub-100 fs mobile charge generation in a polymer-fullerene film. *Phys. Rev. Lett.* **108**, 056603/1 (2012).
40. N. Banerji, S. Cowan, M. Leclerc, E. Vauthey, A. J. Heeger, Exciton Formation, Relaxation, and Decay in PCDTBT. *J. Am. Chem. Soc.* **132**, 17459 (2010).
41. L. G. Kaake, D. Moses, A. J. Heeger, Coherence and Uncertainty in Nanostructured Organic Photovoltaics. *J. Phys. Chem. Lett.* **4**, 2264 (2013).
42. K. Chen, A. J. Barker, M. E. Reish, K. C. Gordon, J. M. Hodgkiss, Broadband Ultrafast Photoluminescence Spectroscopy Resolves Charge Photogeneration via Delocalized Hot Excitons in Polymer:Fullerene Photovoltaic Blends. *J. Am. Chem. Soc.* **135**, 18502 (2013).
43. S. Gelinas *et al.*, The Binding Energy of Charge-Transfer Excitons Localized at Polymeric Semiconductor Heterojunctions. *J. Phys. Chem. C* **115**, 7114 (2011).
44. F. C. Jamieson, T. Agostinelli, H. Azimi, J. Nelson, J. R. Durrant, Field-Independent Charge Photogeneration in PCPDTBT/PC70BM Solar Cells. *J. Phys. Chem. Lett.* **1**, 3306 (2010).
45. M. Wojcik, M. Tachiya, Accuracies of the empirical theories of the escape probability based on Eigen model and Braun model compared with the exact extension of Onsager theory. *J. Chem. Phys.* **130**, 104107/1 (2009).
46. A. A. Bakulin *et al.*, The Role of Driving Energy and Delocalized States for Charge Separation in Organic Semiconductors. *Science (Washington, DC, U. S.)* **335**, 1340 (2012).
47. J. Lee *et al.*, Charge Transfer State Versus Hot Exciton Dissociation in Polymer-Fullerene Blended Solar Cells. *J. Am. Chem. Soc.* **132**, 11878 (2010).
48. K. Vandewal *et al.*, Efficient charge generation by relaxed charge-transfer states at organic interfaces. *Nat. Mater.* **13**, 63 (2014).
49. G. Grancini *et al.*, Hot exciton dissociation in polymer solar cells. *Nat. Mater.* **12**, 594 (2013).

50. A. A. Bakulin *et al.*, The Role of Driving Energy and Delocalized States for Charge Separation in Organic Semiconductors. *Science (Washington, DC, U. S.)* **335**, 1340 (2012).
51. S. D. Dimitrov *et al.*, On the Energetic Dependence of Charge Separation in Low-Band-Gap Polymer/Fullerene Blends. *J. Am. Chem. Soc.* **134**, 18189 (2012).
52. F. Provencher *et al.*, Direct observation of ultrafast long-range charge separation at polymer: fullerene heterojunctions. *arXiv.org, e-Print Arch., Condens. Matter*, 1 (2013).
53. E. R. Bittner, C. Silva, Noise-induced quantum coherence drives photo-carrier generation dynamics at polymeric semiconductor heterojunctions. *Nat. Commun.* **5**, 4119/1 (2014).
54. F. Etzold *et al.*, Ultrafast Exciton Dissociation Followed by Nongeminate Charge Recombination in PCDTBT:PCBM Photovoltaic Blends. *J. Am. Chem. Soc.* **133**, 9469 (2011).
55. S. Gelinas *et al.*, Ultrafast Long-Range Charge Separation in Organic Semiconductor Photovoltaic Diodes. *Science (Washington, DC, U. S.)* **343**, 512 (2014).
56. A. M. Ballantyne *et al.*, Understanding the Influence of Morphology on Poly(3-hexylselenophene):PCBM Solar Cells. *Macromolecules (Washington, DC, U. S.)* **43**, 1169 (2010).
57. C. Muller *et al.*, Binary organic photovoltaic blends: a simple rationale for optimum compositions. *Adv. Mater. (Weinheim, Ger.)* **20**, 3510 (2008).
58. F. C. Jamieson *et al.*, Fullerene crystallisation as a key driver of charge separation in polymer/fullerene bulk heterojunction solar cells. *Chem. Sci.* **3**, 485 (2012).
59. N. C. Cates *et al.*, Tuning the Properties of Polymer Bulk Heterojunction Solar Cells by Adjusting Fullerene Size to Control Intercalation. *Nano Lett.* **9**, 4153 (2009).
60. J. A. Bartelt *et al.*, The importance of fullerene percolation in the mixed regions of polymer-fullerene bulk heterojunction solar cells. *Adv. Energy Mater.* **3**, 364 (2013).
61. Z. M. Beiley *et al.*, Morphology-dependent trap formation in high performance polymer bulk heterojunction solar cells. *Adv. Energy Mater.* **1**, 954 (2011).
62. N. C. Miller *et al.*, Factors governing intercalation of fullerenes and other small molecules between the side chains of semiconducting polymers used in solar cells. *Adv. Energy Mater.* **2**, 1208 (2012).
63. T. M. Burke, M. D. McGehee, How high local charge carrier mobility and an energy cascade in a three-phase bulk heterojunction enable >90% quantum efficiency. *Adv. Mater. (Weinheim, Ger.)* **26**, 1923 (2014).
64. A. J. Mozer *et al.*, Time-dependent mobility and recombination of the photoinduced charge carriers in conjugated polymer/fullerene bulk

- heterojunction solar cells. *Phys. Rev. B: Condens. Matter Mater. Phys.* **72**, 035217/1 (2005).
65. S. K. Pal *et al.*, Geminate Charge Recombination in Polymer/Fullerene Bulk Heterojunction Films and Implications for Solar Cell Function. *J Am Chem Soc* **132**, 12440 (Sep 8, 2010).
  66. W. L. Rance *et al.*, Photoinduced Carrier Generation and Decay Dynamics in Intercalated and Non-intercalated Polymer:Fullerene Bulk Heterojunctions. *ACS Nano* **5**, 5635 (2011).
  67. A. Pivrikas *et al.*, Langevin recombination and space-charge-perturbed current transients in regiorandom poly(3-hexylthiophene). *Phys. Rev. B: Condens. Matter Mater. Phys.* **71**, 125205/1 (2005).
  68. S. De *et al.*, Geminate Charge Recombination in Alternating Polyfluorene Copolymer/Fullerene Blends. *J. Am. Chem. Soc.* **129**, 8466 (2007).
  69. W. Zhang *et al.*, Mechanism of Primary Charge Photogeneration in Polyfluorene Copolymer/Fullerene Blends and Influence of the Donor/Acceptor Lowest Unoccupied Molecular Orbital Level Offset. *J. Phys. Chem. C* **117**, 735 (2013).
  70. B. S. Rolczynski *et al.*, Ultrafast intramolecular exciton splitting dynamics in isolated low-band-gap polymers and their implications in photovoltaic materials design. *J Am Chem Soc* **134**, 4142 (2012).
  71. Y. Zou *et al.*, A Thieno[3,4-c]pyrrole-4,6-dione-Based Copolymer for Efficient Solar Cells. *J. Am. Chem. Soc.* **132**, 5330 (2010).
  72. C. Piliago *et al.*, Synthetic Control of Structural Order in N-Alkylthieno[3,4-c]pyrrole-4,6-dione-Based Polymers for Efficient Solar Cells. *J. Am. Chem. Soc.* **132**, 7595 (2010).
  73. C. Cabanetos *et al.*, Linear Side Chains in Benzo[1,2-b:4,5-b']dithiophene-Thieno[3,4-c]pyrrole-4,6-dione Polymers Direct Self-Assembly and Solar Cell Performance. *J. Am. Chem. Soc.* **135**, 4656 (2013).
  74. C. Risko, M. D. McGehee, J.-L. Bredas, A quantum-chemical perspective into low optical-gap polymers for highly-efficient organic solar cells. *Chem. Sci.* **2**, 1200 (2011).
  75. I. Hwang, S. Beaupre, M. Leclerc, G. D. Scholes, Ultrafast relaxation of charge-transfer excitons in low-bandgap conjugated copolymers. *Chem. Sci.* **3**, 2270 (2012).
  76. S. Shi *et al.*, Efficient polymer solar cells based on a broad bandgap D-A copolymer of "zigzag" naphthodithiophene and thieno[3,4-c]pyrrole-4,6-dione. *J. Mater. Chem. A* **1**, 1540 (2013).
  77. M. Baklar *et al.*, Ink-jet printed p-type polymer electronics based on liquid-crystalline polymer semiconductors. *J Mater Chem* **20**, 1927 (2010).
  78. B. H. Hamadani, D. J. Gundlach, I. McCulloch, M. Heeney, Undoped polythiophene field-effect transistors with mobility of 1 cm<sup>2</sup> V<sup>(-1)</sup> s<sup>(-1)</sup>. *Appl Phys Lett* **91**, (Dec 10, 2007).

79. I. McCulloch *et al.*, Liquid-crystalline semiconducting polymers with high charge-carrier mobility. *Nat Mater* **5**, 328 (Apr, 2006).
80. A. C. Mayer *et al.*, Bimolecular Crystals of Fullerenes in Conjugated Polymers and the Implications of Molecular Mixing for Solar Cells. *Adv Funct Mater* **19**, 1173 (Apr 23, 2009).
81. E. Cho *et al.*, Three-Dimensional Packing Structure and Electronic Properties of Biaxially Oriented Poly(2,5-bis(3-alkylthiophene-2-yl)thieno[3,2-b]thiophene) Films. *J Am Chem Soc* **134**, 6177 (2012/04/11, 2012).
82. E. B. Domingo, Ferguson, A. J., Jamieson, F. C., McCarthy-Ward, T., Shoaee, S., Tumbleston, J., Kopidakis, N., Reid, O. G., Madec, M.-B., Pfannmöller, M., Schröder, R. R., Watkins, S., Portale, G., Hermerschmidt, F., Smith, P., Heeney, M., Ade, H., Rumbles, G., Durrant, J. R., and Stingelin, N, "Additive-assisted supramolecular manipulation of PBTTT:PCBM blend microstructures," Submitted to *Materials Horizons*.



# **CHAPTER TWO**

## **Experimental**

## 2.1 Spectroscopic Techniques: General Introduction

In this thesis, we performed experiments and compared data from two complementary time-resolved experiments: transient absorption spectroscopy (TAS) and THz-time domain spectroscopy. It is possible to obtain information on exciton generation, dissociation, as well as on the lifetime of the generated charge carriers and on the recombination processes using these techniques. The peculiarity of THz time domain spectroscopy is that it is more selective to detect the contribution of (free) charges with femtosecond time resolution, since the energy in the THz range (one THz corresponds to a photon energy of 4 meV) can be absorbed by charge carriers. However, this is not enough to promote electronic transitions in molecules, atoms and semiconductors. Excitons have only a weak absorption in the THz range (due to a microscopic change in the polarizability), which should be more important in the case of extended delocalization. Moreover, the technique allows us to have access to the spectrally resolved photoconductivity, from which it should be possible to distinguish the presence of bound charges (excitons, charge transfer states) and free charges (polarons). Information on charge mobility can also be obtained. On the other hand, the TAS technique is sensitive not only to the free polarons, but also to excitons and to the bound charge pairs (charge transfer state). The drawback of this experiment is that it presents very broad absorption bands, which make it difficult to distinguish clearly among different processes (exciton decay, charge separation, spectral dynamics due to excited state relaxation, dynamics of bound and free charges, and recombination).

Photo-induced THz time domain experiments and femtosecond transient absorption spectroscopy (TAS) are both pump-probe time-resolved techniques. The principle of these techniques is to excite the system by an optical pulse (pump) and to use another optical or THz pulse (probe) to measure the variation on the optical or THz absorption of the system caused by the pump pulse. By changing the time delay between pump and probe pulses, the changes happening in the sample - following photo-excitation - are monitored with a sub picosecond time resolution.

## 2.2 Transient Absorption Spectroscopy (TAS)

Transient absorption spectroscopy is among ultrafast spectroscopies, which can time resolve the evolution of phenomena happening in a sample, after its

pump excitation. This is possible thanks to the use of a femtosecond laser, which produces pulses with a short temporal width, such that it is possible to investigate phenomena in a time scale from the ps and to the few fs range. As in a usual pump-probe experiment, a pump beam is perturbing the system at the time  $\Delta t=0$  and a probe beam is monitoring the changes in absorption of the sample at a certain time delay with respect to the pump beam (1). After the pump excitation, the absorption of the sample is changed; this situation can be detected by the change in the number of transmitted photons from the probe beam with respect to the un-pumped situation. Pump and probe come from the same laser and have the same repetition rate. In our setup, the optical path length of the pump is delayed with respect to the probe. The time resolution of the experiments depends on the temporal width of the pump and probe but not on the delay between the pump and probe beam.

The probe beam is split into two beams: one is going through the sample and is detected in a situation in which the sample is pumped ( $I_p$ ) and un-pumped ( $I_{np}$ ), using a synchronized chopper at half the laser frequency in the pump. The other is bypassing the sample (reference)  $I_r$ . A scheme of a pump-probe experiment is shown in Figure 2.1.

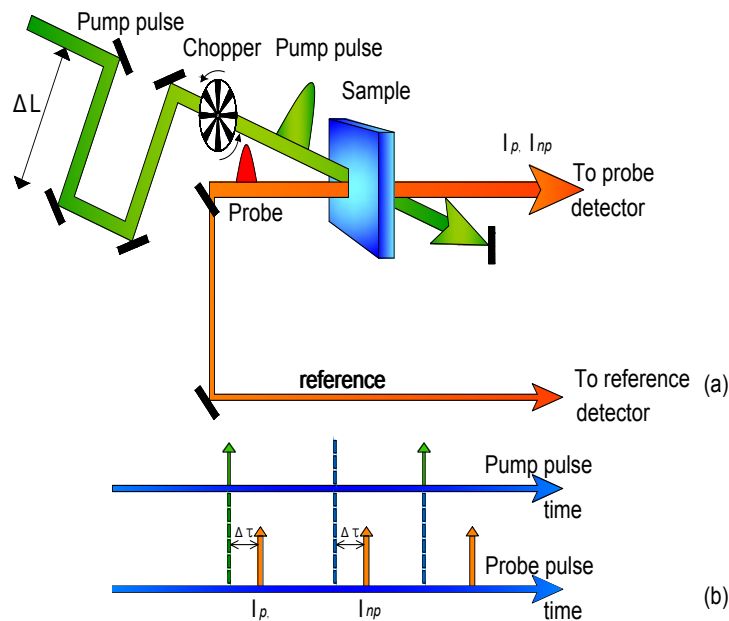


Figure 2.1 Scheme of a pump-probe experiment: a) the pump beam is delayed with respect to the probe beam using a delay line. The intensity of the probe beam after the sample is detected. The reference beam is bypassing the sample going directly to the reference detector.  $I_p$  and  $I_{np}$  are the pumped and un-pumped probe beams.  $\Delta L$  is the delay distance. b)  $\Delta t$  is the temporal delay between the pump and the probe.



Let us now look how the transient intensity is obtained from the detected pulses. In order to do this, let us define the different beams:

- $I_0$ : intensity of the probe beam before the sample
- $I_p$ : intensity of the probe beam after the sample (pumped mode)
- $I_{np}$ : intensity of the probe beam after the sample (un-pumped mode)
- $I_{ref}$ : reference intensity bypassing the sample

The shot by shot detection is allowing high sensitivity. For each shot, the transmitted intensities of signal and reference are detected. We must take into account the fact that between two different shots there might be some laser fluctuation such that the detected intensity is not the same, therefore we use the ratio between the consecutive reference pulses to correct for the fluctuation (we denote with a prime the pulse intensity of two different shots). This is expressed in the following equation:

$$\frac{I'_0}{I_0} = \frac{I'_r}{I_r} \quad 1)$$

We know that the absorbance without the pump is given by the following formula (from the Lambert-Beer law):

$$A_{np}(\lambda) = -\log \frac{I_{np}}{I_0} \quad 2)$$

If we write the same for the intensity detected in pumped mode, the transient absorption for a certain delay time between the pump and the probe is obtained from the difference:

$$\Delta A(\lambda) = A_p(\lambda) - A_{np}(\lambda) = \log \frac{I_{np}}{I_0} - \log \frac{I'_p}{I'_0} = \log \frac{I_{np} I'_0}{I'_p I_0} = \log \frac{I_{np} I'_r}{I'_p I_r} \quad 3)$$

If we detect the transient absorption signal for different time delays we get the time-resolved dynamics. The amplitude of the transient spectra is proportional to the population created from the pump, with a proportionality depending on the absorption coefficient, the sample thickness and the concentration of excited species. For each pump-probe delay time, this technique is also able to provide the transient spectra in the visible range (400 - 750 nm) and the nIR range (750 -1000 nm). In this way, we get spectra with positive and negative features, which give us information about the different photo-induced species present in the sample after that pump

excitation has caused different photo-physical processes. We will now describe the different contributions, as shown Figure 2.2.

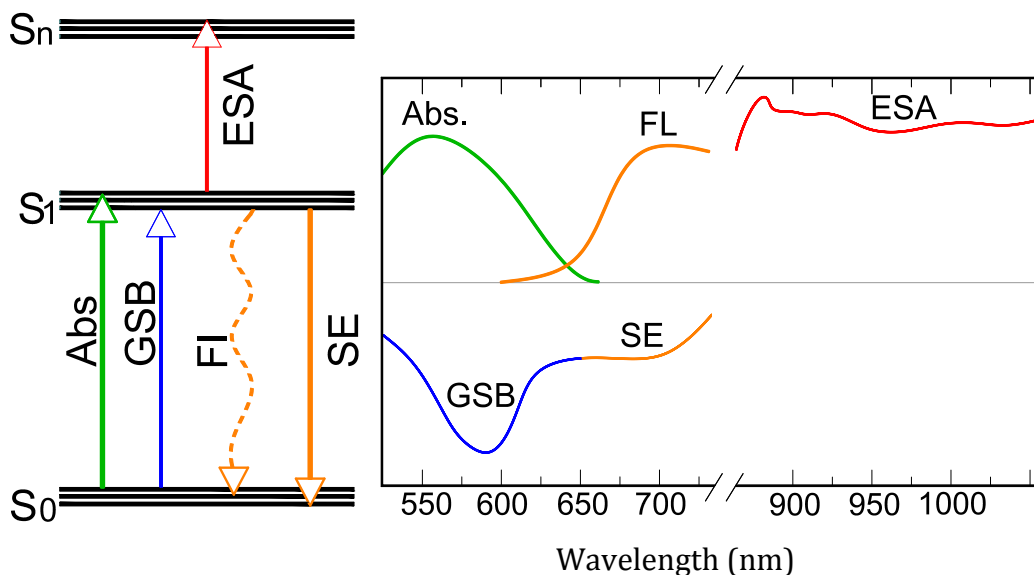


Figure 2.2 On the left, an energy diagram describing the different contributions to the transient absorption spectra. On the right, different features in a typical transient absorption spectrum.

- The negative  $\Delta A$  contribution is called ground state bleaching (GSB) and corresponds to a situation where there is a lack of molecules in the ground state: in this situation, the absorption of the excited state is lower than that in the ground state. The amplitude of the GSB is proportional to the population of species missing from the ground state. The dynamics of the GSB is indicating the way in which the excited state is recovering to the ground state.
- The other negative  $\Delta A$  contribution is called stimulated emission (SE): the stimulated emission band is coming from the fluorescence of the excited state induced by the probe beam. The emitted photons have the same frequency and direction of the incoming probe beam. The band has Stokes shifted with respect to the GSB. In general, when the stimulated emission band is decaying, it indicates a depopulation of the excited state. In a polymer: fullerene BHJ, the SE band is vanishing due to exciton quenching during charge transfer.
- The positive contribution to the spectra is called excited state absorption (ESA). If the photo-induced species absorb in the

wavelength region of the probe, this band describes a situation in which a molecule is already in the excited state ( $S_1$ ) and is excited further into a higher state ( $S_n$ ). In general, this band is showing the signature of the excited state. The absorption can however also come from the triplet state or photo-generated charges. Specifically, in polymer:fullerene blends, this band can show the signature of excitons, triplet excitons, charge pairs, charge transfer states, or polarons (free charges).

### 2.2.1 Experimental Apparatus for TAS

Let us now describe the details of the experimental TAS setup used in this thesis. The schematic representation of the setup is illustrated in Figure 2.3.

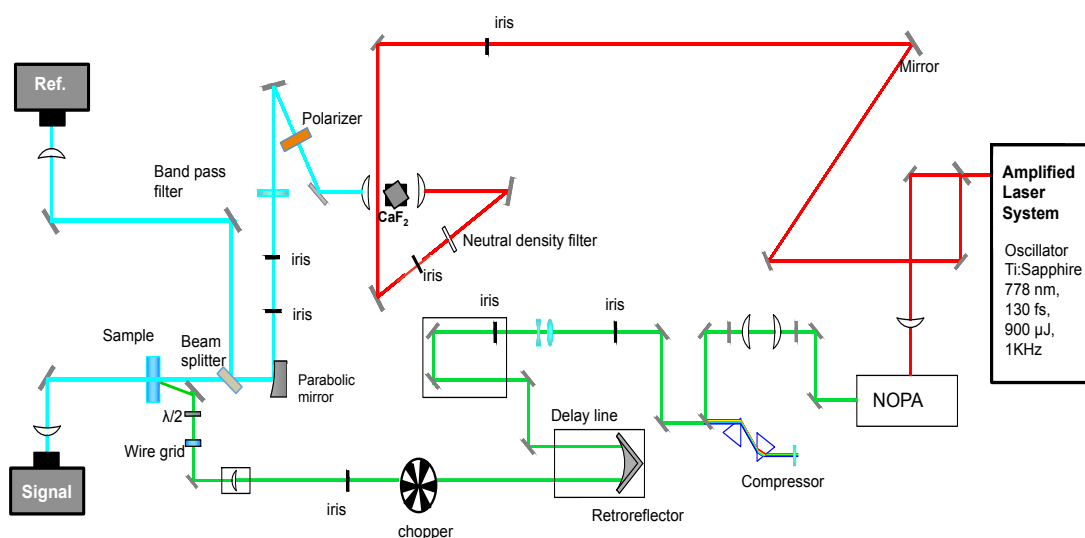


Figure 2.3 Schematic representation of the transient absorption setup.

I have used this setup in two configurations: one with the probe being visible white light (400-750 nm) and the other with the probe in the nIR range (750-1000 nm). The setup consists mainly of an amplified femtosecond laser with 900 μJ pulse energy centred at 775 nm, of a NOPA (non-linear optical parametric amplifier) providing wavelengths in the range 450 - 700 nm for generating the pump beam, of a medium for white light and nIR probe generation, and of a signal and reference spectrometer for the detection of the probe light. Let us now describe the detailed characteristics of each specific element.

probe light. Let us now describe the detailed characteristics of each specific element.

### ***2.2.1.1 The Femtosecond Laser***

The laser used is a CPA-2001 model from Clark-MXR. The center wavelength of the laser is at about 775 nm. The pulse duration is about 150 fs and the average power is about 950  $\mu$ J with a repetition rate at 1 kHz. The medium used to generate the pulses is a Ti:Sapphire regenerative amplifier pumped by the second harmonic of a Nd:YAG. The oscillator of the system consists of a Er-doped fiber laser. Before amplification, the pulse is stretched in time and frequency to decrease the power. After several amplifications in the Ti:Sapphire cavity, the pulse is compressed back with gratings to obtain an amplified short pulse (2).

### ***2.2.1.2 Generation of the Pump Pulses***

In a TAS experiment, usually we need to use different wavelengths as pump excitation. The two wavelengths I used in the experiment are mainly 390 nm and 540 nm. In order to generate 540 nm, I used the non-linear optical parametric amplifier (NOPA). The generation of the 390 nm wavelength is not possible with the NOPA, therefore we provided a different path to generate the second harmonic from the 775 nm laser output, which enters inside a BBO crystal.

### **The non-linear optical parametric amplifier (NOPA)**

The setup used to obtain pump wavelengths in the range 450 nm to 700 nm is the NOPA (Non-linear Optical Parametric Amplifier). A part of the output pulses of the laser (150  $\mu$ J) is seeded into the NOPA. In order to obtain white light (supercontinuum generation) it is possible to use either a sapphire plate ( $\text{Al}_2\text{O}_3$  aluminium oxide) or either a  $\text{CaF}_2$  crystal. The latter has been used to generate the probe white light and the former has been used to generate the white light inside the NOPA. In order to be able to obtain a high intensity output power, the NOPA consists of two stages. After the second stage the beam is amplified six times with respect to the first one.

In the first stage, a small part of the incoming 775 nm pulse is passing through a sapphire plate to generate white light. Sapphire exhibits wide

optical transmission in the visible, UV, and NIR and it is an anisotropic birefringent crystal, which means that it has two optical axes. Light beams entering the crystal parallel to an optical axis will pass straight through, but those entering with an angle will split in two traveling along the two optical axes at different speeds, emerging in slightly different places and vibrating in planes that are mutually perpendicular. Supercontinuum generation is a process where laser light is converted to white light with a very broad spectral bandwidth whereas the spatial coherence usually remains high. The process is caused by the nonlinear effects of high power ultra short (laser) light pulses passing through a centrosymmetric transparent medium. When the electric field of the light becomes comparable in strength to the material's atomic field, the higher order nonlinear terms of susceptibility to the polarization ( $\vec{P}$ ) expansion are not negligible anymore:

$$\vec{P} = \epsilon_0(\chi^{(1)}\vec{E} + \chi^{(2)}\vec{E}^2 + \chi^{(3)}\vec{E}^3 + \dots) \quad 4)$$

where  $\chi^{(n)}$  is the nth order susceptibility (3). As each non-linear term of this equation comes into play, many non-linear processes can occur in the crystal. In this case, we are only concerned with centrosymmetric materials, for which all of the even order terms drop out (4). Therefore we can ignore the second order non-linear term. The third order term in this equation leads to the processes of self-focusing and self-phase modulation (SPM)(5),(6), which are the basis of continuum generation (CG). Both self-focusing and SPM can be explained using the basic non-linear CG equation, which can be derived from equation 4):

$$n=n_0 + n_2 \cdot I(r,t) \quad 5)$$

Here,  $n_0$  is the linear refractive index and  $n_2$  is the second order non-linear refractive index. As we can see from the above equation, the non-linear index of refraction ( $n$ ) is dependent upon the intensity of the laser beam ( $I$ ), which in turn has both spatial ( $r$ ) and time ( $t$ ) dependence. SPM is based on the intensity dependence of the index of refraction with time. This time variation in intensity is what creates a variety of frequencies and colours from a nearly monochromatic light source.

In the NOPA, the remaining beam from the incoming 775 nm is seeded to a non-linear BBO (beta-barium borate) crystal for second harmonic generation (a second-order non-linear effect) to obtain a blue beam (390 nm). Then this

beam and the WL are focused on another non-linear BBO crystal. By tuning the angle of the BBO crystal, changing the angle between the white light seed and the pump, and the delay between the two, it is possible to obtain the phase-matching condition for selected colours of the white light, which will be amplified. After the first stage, the output beam can be still amplified six times by passing through the second stage. In this part of the NOPA, the beam coming out of the first stage is focused again together with a 390 nm beam onto another BBO crystal. Finally, the outgoing pulses have an energy between 6-12  $\mu\text{J}$  which can vary according to the selected wavelength. The spectrum of the NOPA output is monitored with a dual-channel spectrometer (S2000, Ocean Optics).

### **Pulse compression**

Since the outgoing optical pulses go through many optical elements in the NOPA (e.g. glasses or lenses) and non-linear crystals, they result in a frequency which is chirped, delayed, and marked by an increased duration (up to 500 fs). This situation is compensated by pulse compression.

The phenomenon known as pulse chirp is called GVD (**group velocity dispersion**). The most commonly known phenomenon of dispersion in optics is the separation of white light by refraction into its components creating a full visible colour spectrum. Indeed, as the refractive index of a particular medium depends upon the wavelength, the result is the angle at which light is deflected will also change with wavelength. Consequently the different colours mixed in a ray of light will split at an angle, generating a phenomenon known as angular dispersion. The empirical formulas, which are usually used to quantitatively describe the wavelength dependence of a refractive index of a given material, are the Cauchy or the Sellmeier equations (7, 8). The behaviour of most transparent materials (e.g. glasses), for visible spectral range, can be described in this way:

$$1 < n(\lambda_{\text{red}}) < n(\lambda_{\text{yellow}}) < n(\lambda_{\text{blue}}) \quad 6)$$

or :

$$dn(\lambda)/d\lambda < 0$$

That is, the refractive index  $n(\lambda)$  decreases with increasing wavelength  $\lambda$ , as well as its first derivative. In this situation, the medium is characterized by a normal dispersion. Alternatively, if the refractive index increases with an increasing wavelength, the medium will have an anomalous dispersion (9).

More specifically, the different spectral component of an optical pulse has a different group velocity, which itself is dependent on the wave's frequency. This will cause that the deviation for each frequency component differs due to the different group velocity of different wavelengths passing through the refracting medium. This will result in group velocity dispersion (GVD). As a consequence, there will be some frequencies which will travel faster than some others, resulting in a temporal broadening of a short optical pulse of light. GVD can be described by the group delay dispersion parameter shown in equation 7), which can be used strictly for uniform medium:

$$D = -\frac{\lambda \partial^2 n(\lambda)}{c \partial \lambda^2} \quad 7)$$

It is possible to define a positive or negative dispersion: if  $D$  assumes a value less than zero, the medium has a positive dispersion. However, if  $D$  is a number greater than zero, the medium has a negative dispersion. The pulse of light will be positively chirped - or up-chirped if the higher frequency components (blue part of the pulse) travels slower than the lower frequency components (red part of the pulse). Usually this happens when the ray of light propagates through a normally dispersive medium. In this case, the group velocity of the pulse decreases with increasing frequency. In the same way, when a pulse travels through an anomalously dispersive medium, high frequency components travel faster than the lower ones. This corresponds to a pulse which is negatively chirped - or down-chirped. This effect induces a spread in time of the pulse's arrival on the sample, which we need to correct for.

To correct for this chirp, two pairs of prisms are used as in the configuration shown in Figure 2.4.

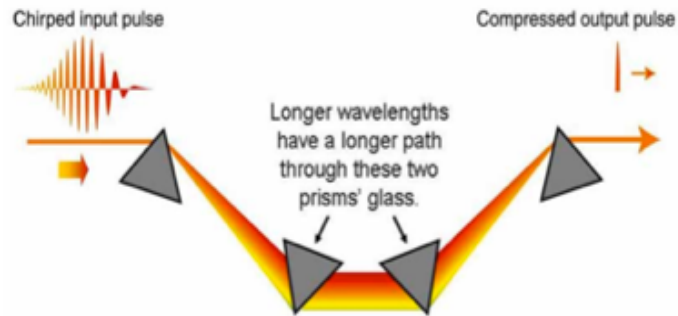


Figure 2.4 Pulse compression obtained by the use of two pairs of prisms (10).

In the first prism, the chirped input pulse undergoes retraction for each wavelength component with a different angle (it is dispersed). A second prism, located in reverse in relation to the first, has the role to collimate the dispersed incoming beam in a way that the red wavelengths undergo more material respect to the blue components such that its velocity will decrease (this compensates the chirp). But the outgoing pulse will still be spatially dispersed. To correct this, typically a second pair of prisms is used. However in our setup, we used a mirror, which reflects the beam in a way so that it passes again through the first two prisms. This path has the role to spatially collimate the beam. The incident beam has to hit the prism at the Brewster angle to avoid the loss due to reflection. The distance between the prisms is different according to the input wavelength. The outgoing pulse after the compression has a temporal width of 50 fs. In order to measure the temporal width of the outgoing pulse, we used the autocorrelation technique. The principle of this technique is based on splitting the beam into two paths with a beam splitter: one is delayed with respect to the other with a delay stage. Afterwards, they are spatially overlapped on a non-linear medium for the second harmonic generation process. Finally, the beam generated has a frequency, which is twice the input frequency. A scheme of the autocorrelator is shown in Figure 2.5.



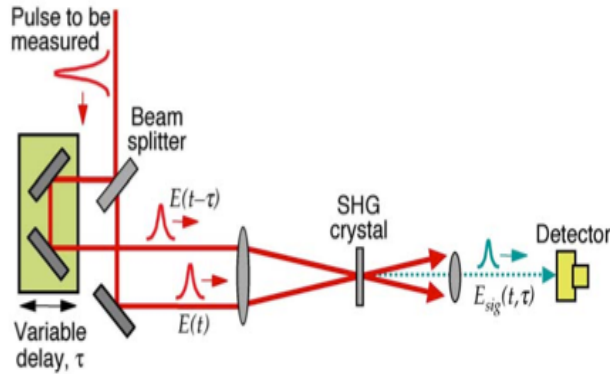


Figure 2.5 Experimental scheme for an autocorrelator using second-harmonic generation. The incoming beam is split into two parts: one is going through a variable delay stage and the second is overlapped on the second harmonic crystal generation in order to produce a pulse with a frequency which is the double of that one of the incoming beam. This pulse will be temporally measured versus time (11).

After the compression and the temporal pulse measurements, the pump beam is going through a fixed delay stage (which compensates for the distance between the prisms), then through a computer-controlled delay stage which sets the pump-probe delay, and finally it is focalized on the sample. The NOPA is not able to generate a wavelengths below 450 nm. Since we need an excitation wavelength of 390 nm to do some experiment, we used in the same setup another excitation path.

### **Generation of the 390 nm pump pulses**

In order to generate the blue excitation pump pulse at 390 nm, we used an alternative path: the 775 nm beam coming from the laser goes through a telescope, travels through a manual delay stage, and after few reflections is passing through a BBO crystal allowing SHG (second harmonic generation) to obtain 390 nm pulses. After the BBO crystal, a cut-off filter is needed to eliminate the remaining fundamental component. By changing the distance of the lenses in the telescope, it is possible to adjust the spot size of the 775 nm beam, which hits the crystal.

#### ***2.2.1.3 Generation and Detection of the Probe Pulses***

The probe beam used in the experiments is either in the visible range or in the nIR range. In order to generate the probe beam in the visible range, part

of the fundamental 775 nm beam is used from the main laser. In fact, part of the main laser beam energy (450  $\mu$ J) is used to pump the NOPA and some remaining part (20  $\mu$ J) is used to generate white light. The non-linear physical phenomenon for the generation of white light is self phase modulation, as seen in section 2.1.2.2. In our setup, we used a CaF<sub>2</sub> window for white light generation, which replaces the sapphire plate used in the previous setup. The advantage in using this medium is the extended frequency range in the UV and nIR ranges. After a few reflections, the 775 nm beam is focused on a 5 mm thick CaF<sub>2</sub> window, using a 5 cm lens as shown in Figure 2.6.

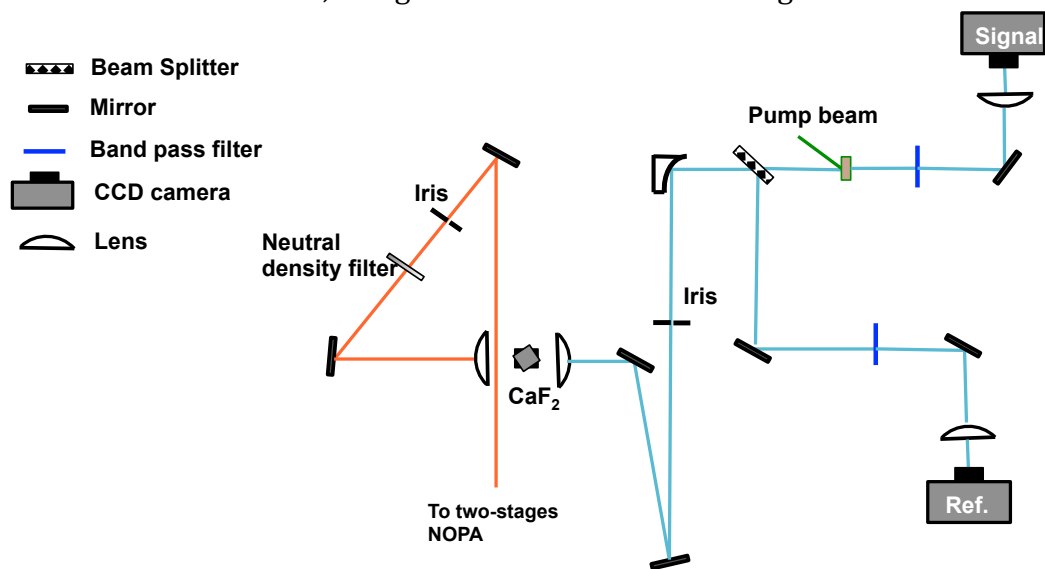


Figure 2.6 Scheme of a white continuum white light generation: the 800 nm enters the CaF<sub>2</sub> crystal and after collected on the sample with a parabolic mirror.

In order to avoid burning of the CaF<sub>2</sub> window, there is the possibility to move the window on a 2-axis translation stage and in the z direction using a vibration generator controlled by a motor (B2-2185.00, djb). In order to optimize the quality and the stability of the white light, it is possible to play with the iris and with a neutral density filter, placed in front of the CaF<sub>2</sub> window. The outgoing beam is collimated with a 5 cm lens (which was at one point replaced by a 10 cm spherical mirror), before passing through filters to remove any remaining fundamental light and through a wire-grid polarizer, which cleans the polarization. The beam is then collected by a parabolic mirror, which allows to avoid additional chirp dispersion of the beam. Using a reflective OD 0.5 filter, the generated white light is then divided in two: one part is going through the sample to the signal spectrograph, and the second is going to the reference detector. When generating the nIR probe

light in the range 750 - 1100 nm, we replaced the 350 - 750 nm band pass filter in the white light with a cut-off filters at 850 nm (high-pass), adjusted the polarizer for maximum transmission and changed the grating of the spectrographs.

### **Detection details**

After the splitting of the probe beam into two parts (signal and reference), the two beams are detected by two different spectrographs (Spectra Pro 2150). In each case, the input beam is focused by a 5 cm focal length achromatic lens, which can be moved along the three-axis directions to guide the focused beam through a 200 mm slit. The dispersive medium used in the spectrographs is a diffraction grating. The latter is an optical component used to spatially separate polychromatic light (white light) into its constituent optical frequencies. The simple grating consists of a glass substrate with a series of parallel, equi-spaced lines on the front surface of the glass. Notice that the optical beam enters the periodic pattern (spatial fringe pattern) with a particular angle of incidence.

After dispersion, all of the component wavelengths are projected onto a CCD (Hamamatsu S7030-0906) with 512\*58 pixels located on the focal plane. In order to detect the different frequency ranges, it is possible to change the grating via a computer controlled program (Mono). The first (500 nm blaze) allows the analysis of white light in the range 350-800 nm, and the second (800 nm blaze) allow the analysis of nIR-white light in the range 750-1100nm. In order to detect the visible white light, a band-pass filter is needed (350-750 nm) to remove the fundamental wavelength of the laser. On the other hand, when we want to detect the nIR light, a 750 nm and/or 850 nm long pass filter is used before the beam enters on the spectrographs. Usually a variable optical density filter is also used in front of the spectrographs to avoid the effect of saturation in the response of the detectors (the intensity should be between 1000 and 60000 counts per channel) and to be able to have the same signal intensity between the signal and the reference cameras. The calibration of the spectrographs has been achieved using a set of interferential filters (10 nm band-pass) and by moving the gratings accordingly. The detection is shot by shot, and to improve the signal to noise ratio, the signal was averaged over 3000-6000 shots.

## 2.2.2 Experimental Settings and TAS Data Treatment

Before we start measurements with the TAS pump- probe experiment, we need to set and to check various important parameters:

- pump and probe beam spatial and temporal overlap
- spot size and energy of the pump pulses (fluence)
- magic angle between the pump and the probe polarizations

After the pump wavelength has been generated by the NOPA, the beam passes through a telescope and different lenses. Finally it is reflected with a mirror to the sample. The pump pulse is focalized just after the sample, in order to avoid any non-linear effects on the sample. The probe beam, as well, is focalized with a parabolic mirror on the sample. The probe beam has a much lower power with respect to the pump, in order to limit sample heating and to make sure that only the pump excites the sample.

The two beams are overlapped on the sample **spatially** and **temporally**. The spatial coincidence is the spatial overlap of the two beams on the sample. A CCD camera (part of a Thorlabs beam profiler) that allows monitoring the position of the two spots on the sample facilitates the overlap process. On the other hand, the temporal coincidence occurs when the optical path difference of the two beams is equal to zero. The delay between the two pulses is controlled by a mechanical delay stage, inserted along the pump line, with a retro-reflector (49-668, Edmund Optics). A computerized program controls the movement of the mechanical stage. The slide's maximum path is 30 cm, and the minimum step is 1  $\mu\text{m}$ . In our setup, we also have a second manual delay stage, which is used to roughly set the temporal overlap and which is kept fixed while the first one is moving during the measurements. For setting the 390 nm pump, usually we must manually move the second delay stage in order to find a new time zero.

A chopper at a frequency of 500 Hz, which is half of the laser frequency (1 kHz), is placed on the pump path allowing the pumped and un-pumped transmitted probe signal to be detected. The polarization angle between the pump and the probe is set to the magic angle. Using a  $\lambda/2$  waveplate, it is possible to set the polarization of the pump beam to an angle of  $54.7^\circ$  with respect to the probe polarization. This yields an isotropic excitation of the sample and eliminates the anisotropic component in the pump-probe data.

Before the experiment begins, we need to measure the pump and the probe spot dimension at the sample position (to determine the excitation fluence).

In order to do this, a beam profiler (Thorlabs) captures, displays, and records the spatial intensity profile of the laser beam at a particular plane transverse to the beam propagation path. The beam profiler can measure the whole optical intensity profile of a laser beam, i.e. not only the beam radius but also the detailed shape. In our measurements, we obtained a diameter of around 300  $\mu\text{m}$  for the probe spot and of 800  $\mu\text{m}$  for the pump spot (adjustable by moving the focusing lens).

The last important step necessary for analyzing the TAS data, is to take the cross correlation by Kerr gating (12). This serves to correct for the chirp of the probe beam (caused by group velocity dispersion of the broad white light). Each wavelength of the broad white light reaches the time zero at a different time. Specifically, the red wavelengths are slower in relation to the blue ones, in a way that when the blue part of the spectrum has reached the time zero, the red wavelengths have reached the time zero a few picoseconds before. Since the sample is prepared on a microscope slide substrate, the interaction of the pump and probe light with the substrate is creating different phenomena such as the non-linear Kerr effect. This is a non-linear effect used to measure the instrumental response function of the experiment (time resolution and white light chirp). The Kerr effect occurs when a strong electric field (from the pump) hits the glass, thus changing the index of refraction and creating an anisotropy in the material in the same direction as the incoming polarization. In order to measure the Kerr effect, a Glen-Thompson polarizer has been used and rotated in a way to prohibit probe light from passing through. However, when the pump and probe are temporally overlapped (at time zero for each probe wavelength), the polarization of the probe is rotated by the Kerr effect in a way that the beam is able to go through the polarizer. The signal as a function of time has the shape of a Gaussian for each different wavelength of the probe light.

Then, a Matlab procedure, developed by Banerji et al. allows the correction of the TAS data for the group velocity dispersion (chirp) of the probe. In order to do this for each wavelength, a Gaussian function is used to fit the temporal profile obtained from the Kerr gating. The parameters obtained from the fitting (the maximum of the Gaussian represents time zero for the given wavelength, while the width is related to the time resolution) are then used in the program to perform the chirp correction. In order to analyze the TAS data, a global fitting procedure was typically applied to the dynamics plotted for different wavelengths every 5 nm throughout the TAS spectra. The analysis

function used could be a three or two exponential function like the one shown here:

$$\Delta A = A_1 e^{t/\tau_1} + A_2 e^{t/\tau_2} + A_3 e^{t/\tau_3} \quad 8)$$

In this way, it is possible to distinguish different photo physical processes, assuming the condition that they occur on sufficiently separated time scales.

## 2.3 THz Time Domain Spectroscopy

### 2.3.1 Introduction: Why use THz Spectroscopy?

The peculiarity of THz-time domain spectroscopy is its characteristic frequency range inbetween the electronically attainable lower frequencies and optically attainable higher frequencies. This range of THz frequencies has become feasible thanks to the introduction of femtosecond lasers. One THz corresponds to an energy of 4 meV, which is less than the thermal energy (25 meV). Hence, the THz radiation is particularly appropriate to detect specific properties in condensed state materials (semiconductors, superconductors) as well as in polymer materials. As the transport time of charge carriers in a semiconductor (which is on the fs to ps time scale) matches with the THz range in the electromagnetic spectrum, THz radiation interacts specifically with the electronic motion. The THz radiation is also very suitable to probe the charge generation in conjugated polymers, because the energy in the THz range is resonant with (free) charge carriers, but interacts much less with bound excitons.

On the other hand, the peculiarity of the THz time domain technique, with respect to other time-resolved techniques, is that it allows mapping of the THz electric field as a function of time. The THz time domain technique provides information not only on the amplitude but also on the phase of the electric field (E) without recurring to the Kramers-Kronig analysis (13, 14). This is possible after doing the Fourier transformation of the electric field. The information about the phase of the incoming electric field is lost in TAS due to the fact that the averaged intensity, which we are probing, is proportional to  $E^2$ .

### ***2.3.1.1 Experimental Layout***

#### **Laser and pump generation**

In the terahertz time domain setup, the main laser source is an amplified Ti:Sapphire femtosecond laser (LIBRA, Coherent), which provides pulses with a central wavelength of 800 nm, pulse energy of 4.5 mJ and a temporal width of about 45 fs. The pump pulse is usually in the visible range. It is generated by a tuneable optical parametric amplifier (OPERA SOLO), which can provide pulses in the UV-vis-nIR range (235 - 2700 nm). In the OPA, part of the the incoming 800 nm beam (1.4 mJ) is converted to white light using a sapphire plate and afterwards stretched by a dispersive plate. The white light is temporally spread, then overlapped in a BBO crystal with part of the remaining fundamental beam. At the end of this pre-amplification stage, the resulting wavelength (signal) is overlapped in a second BBO crystal with the rest of the fundamental beam waiting to be amplified. The wavelength is tuned by changing the angle of the BBO crystal and the delay between the main fundamental pump beam and the pre-amplified signal. The total range of frequencies is obtained from the combination of the idler and the signal by using supplementary mixer stages (second harmonic or sum frequency generation steps).

#### **Generation and detection of THz radiation**

The probe pulses of our experiments are in the THz range (300 GHz to several THz). The THz radiation is generated by a 1 mm thick zinc telluride (ZnTe) crystal, which employs the optical rectification effect to generate THz radiation. The latter is a non-linear (difference frequency signal) effect, through which an ultrafast high power pulse is hitting a non-linear crystal generating the THz radiation in a cone. Using two gold-coated off-axis parabolic mirrors, the THz beam is then focused on the sample as shown in Figure 2.7. The THz beam propagates in a box purged with dry nitrogen, which reduces the humidity to a value lower than 6%. In this way, the absorption of THz radiation by air humidity is avoided. In transmission mode, another pair of parabolic mirrors is used to collect the THz pulses transmitted through the sample and to focus them onto a second ZnTe crystal for the detection.

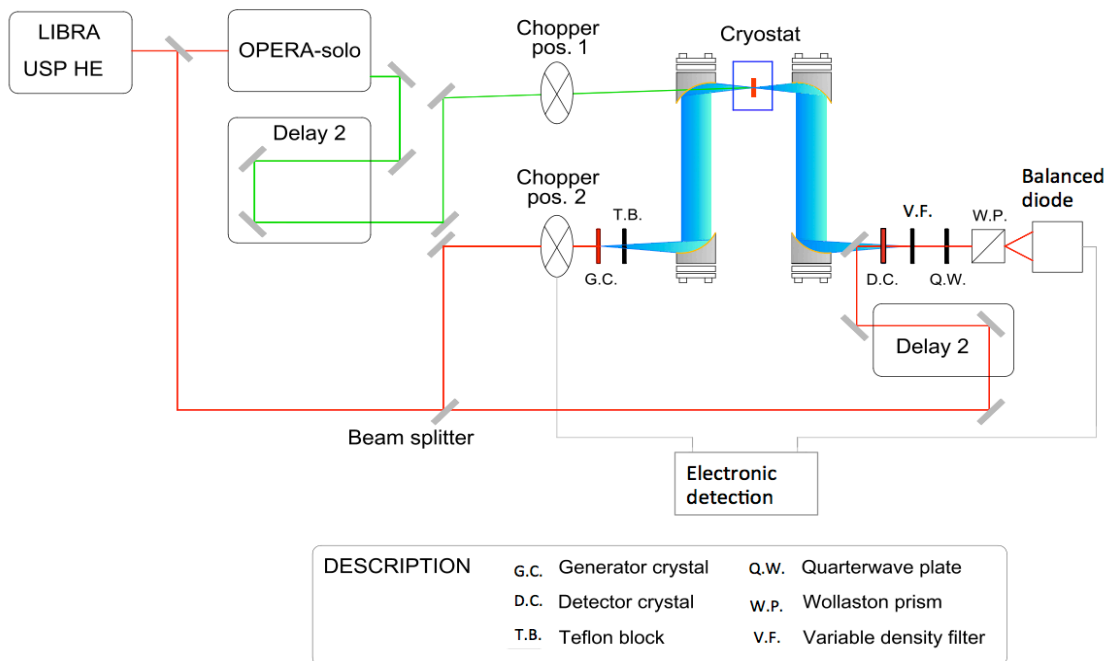


Figure 2.7 THz experimental setup

A gating beam at 800 nm is also going through this ZnTe detection crystal. The THz radiation induces a birefringence inside the crystal, which changes the polarization of the initially linearly polarized gating beam, when there is temporal coincidence. This effect is called electro-optic sampling. As the THz electric field varies on a much slower time scale than the duration of the 800 nm gating beam (several ps against 50 fs), the THz electric field is seen as a constant by the gate. A quarter wave plate is used to make the polarization of the outgoing gating beam circular (in the absence of a THz field) and elliptical (in the presence of it). Then a Wollaston prism separates the horizontal and the vertical components of the elliptical polarized light (15). Finally the intensity of the two components is detected by a pair of balanced photodiodes, which monitor the change in polarization induced by the THz radiation. By varying the time delay between the gating and the THz beams (using a computerized delay stage), the entire THz electric field can be mapped out.

For pump-probe experiments, a chopper running at half of the laser frequency (500 Hz) is placed in the pump beam. The final signal (which was previously recorded by a lock-in amplifier) is now recorded by a



simultaneous sampling data acquisition device NI-PCI-6143. This device reads the analogical signal at the output of the balanced photodiode and converts it to the digital format in the computer memory. The data sampling is synchronized to the laser frequency. Also, the state of the chopper (closed/opened) is recorded simultaneously with each laser shot. This scheme performs a shot by shot detection, in order to improve the signal-to-noise ratio.

### **Data collection and analysis**

The aim of our THz experiments is to obtain information about the response of a sample after photo-excitation, which creates new species such as charges, modifying the index of refraction of the material with respect to the situation where the sample is not pumped. The peculiarity of the THz technique is that not only the change in the amplitude of the electric field is detected, but that also the change in the phase can be detected. The former gives us information about the presence of free charges and the latter about the presence of bound charges. The complex conductivity ( $\sigma$ ) contains all the information on the absorption and on the phase shift of the THz electric field. The index of refraction ( $n$ ), the dielectric constant ( $\epsilon$ ) and conductivity ( $\sigma$ ) of a material are correlated according to equations 9, where  $\epsilon_0$  is the vacuum permittivity. In the experiment as well as in the data analysis we will treat the complex conductivity. After doing the Fourier transform of the complex conductivity, we obtain the real and the imaginary part of the conductivity as a function of the THz frequency (spectra).

$$\sigma_{sample} = -i\omega\epsilon_{sample}\epsilon_0 \quad 9)$$

$$n_{sample}^2 = \epsilon_{sample}$$

A typical pump-probe THz experiment consists in determining the dynamics in the sample after excitation, thus mapping the time-resolved change in THz absorption. Experimentally, this is done by taking the temporal profile of the THz electric field. In order to do this, the gate pulse is delayed with respect to the THz pulse using the delay line on the gate beam, obtaining a single cycle oscillation of the THz field of a period of 2 ps. The gate delay is then set to the maximum of the transmitted THz amplitude and the delay between the excitation (pump) pulse and the THz (probe) beam is varied, on the pump path. The final signal is the transient change in amplitude of the transmitted

electric field ( $\Delta E = E_{\text{pumped}} - E_{\text{un-pumped}}$ ). The amplitude of the signal is giving the average change in THz transmittance due to the photo-excitation. The change in peak amplitude ( $\Delta E/E_{\text{max}}$ , where  $E_{\text{max}}$  is the maximum in the un-pumped THz field) in the THz dynamics is related to the variation in conductivity if there is not a significant phase shift of the THz field.

More information about the nature of the species giving rise to the photo-induced THz signal (excitons, bound or free charges) can be found in the analysis of the THz spectrum obtained by Fourier transformation of the electric field. Usually, the measurements are performed by fixing the pump delay ( $\tau$ ) and mapping the transient THz field by changing the gate delay ( $\Delta E(\omega, \tau) = E_{\text{pumped}}(\omega) - E_{\text{un-pumped}}(\omega)$ ), while positioning the chopper along the pump path. In order to correctly record the spectra, we have to consider the fact that we are not in the steady-state condition because the excited population of a polymer sample changes quickly (200 fs) with time, especially for high fluence. In this condition, the choice to perform the measurement for a fixed pump-probe delay time, is not correct. In fact, each point of the THz field would see a different pump-probe delay. This is due to the fact that the first part of the THz field is detecting a different response with respect to the last part. In order to avoid this problem, it is possible to experimentally impose the steady state condition by scanning both delay stages simultaneously with the same speed. This has been done, in order to assure a constant time delay (13, 16). Finally, the THz electric field is recorded for the excited ( $E_{\text{pumped}}$ ) and not excited sample ( $E_{\text{un-pumped}}$ ), and for a reference substrate ( $E_{\text{ref}}$ ) (quartz substrate); these experimentally determined quantities define completely the conductivity. Typical THz fields are shown in Figure 2.8.

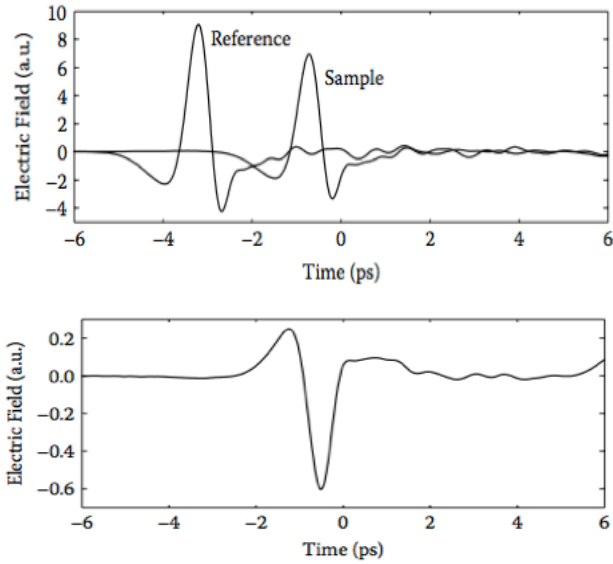


Figure 2.8 Upper panel: THz field with and without the sample: the presence of the sample attenuates the transmitted THz field in amplitude and shifts its phase (17). The lower panel is the transmitted field in presence of the pump.

As the steady state condition is then experimentally obtained, the conductivity can be calculated using the following formulation:

$$\sigma(\omega, \tau) = -\frac{\varepsilon_0 c (n_a + n_b) \Delta E(\omega, \tau)}{d E_{pumped}(\omega)}$$

where  $\varepsilon_0$  is the free space permittivity,  $c$  is the speed of light,  $n_a$  and  $n_b$  are the refractive indices before and after the sample, and  $d$  is the thickness of the sample (18).

The real part and the imaginary part of complex conductivity in the frequency domain can in the end be obtained, after performing the Fourier transform of the conductivity. Since the THz field absorption is in phase with the motion of free charges, the non-zero real part of the photoconductivity gives some information on the presence of free charges, while the imaginary part on presence of bound charges (16, 19).

## Interpretation of the complex conductivity

The physical interpretation of the real and imaginary part of the complex conductivity is correlated to the properties of the investigated material (semiconductor, polymer, or strongly correlated system). The conductivity spectra can give information about the presence of free charges, and bound or localized charges. There have been studies showing many models to describe the response of a material in the THz regime (19, 20).

Among these models, the **Drude model** was the first one to describe the charge transport in a metal or in a semiconductor. In this model, the material is described as a gas of free and independent electrons moving around a positively charged core. The real and imaginary part of the complex conductivity when an external THz electric field is applied are both positive. The real part has its maximal conductivity in proximity of zero frequency and is decreasing with increasing frequency, while the imaginary part has its maximum in proximity of the scattering frequency (21). Knowing the effective electron mass, it is possible to calculate the mobility in bulk semiconductors. Therefore, the Drude model is more appropriate to describe the movement of free or strongly delocalized charges for long-range transport in a semiconductor. However, Smith proposed a model (**Drude-Smith model**) in order to simulate the localization of charges due to the finite medium and hence delimited motion.

Taking into account the fraction ( $c_n$ ) of a carrier's initial velocity preserved after the  $n^{\text{th}}$  scattering event, the Drude-Smith model can take into account different situations: for  $c_n=0$ , the model predicts the classical Drude model, for a negative value of  $c_n$  ( $c_n < -0.5$ ) the model predicts a conductivity which is dominated by the backscattering of charges. In the latter situation, the imaginary part of the conductivity is negative for low frequencies, and for  $c = -1$  the real conductivity reaches its maximum value at a frequency equal to 1 (22).

Figure 2.9 shows the real and the imaginary part of the conductivity according to the Drude model and the Drude-Smith model: it is possible to see how the peak of the real and imaginary parts is shifted toward higher frequency when the charge is getting localized.

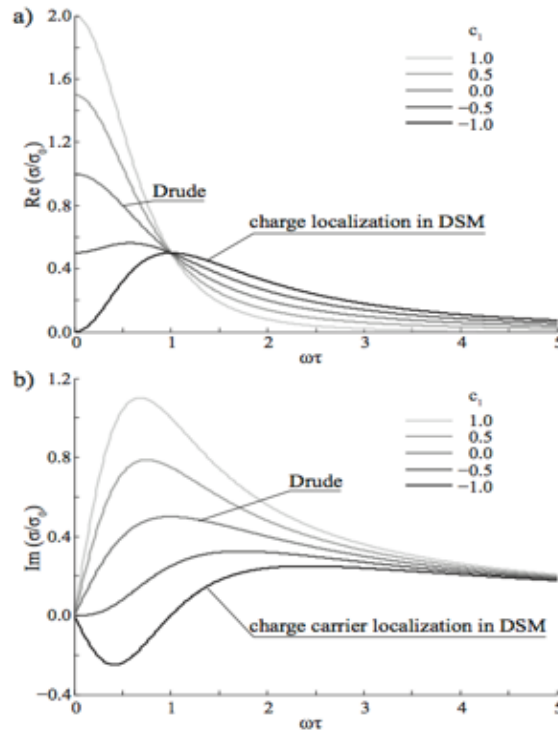


Figure 2.9 a) shows the real conductivity and b) shows the imaginary conductivity plotted using the Drude-Smith model for different persistence velocity coefficients  $C_n$  (23).

If the localization of charges comes from a force, which is driving the charges back to their equilibrium position, the model we need to describe this situation is different from the Drude and from the Drude-Smith model. The spectra obtained in this situation are different from both the previously described models. The behaviour of localized charges, this time, can be described using a simple model of a driven harmonic oscillator with a finite resonance frequency of bound charges. The real and the imaginary parts of the conductivity are completely different from the one described with the Drude model. In fact, the real part of the conductivity is increasing with a quadratic relation with respect to the frequency and reaches the maximum at the resonance frequency. The imaginary part is negative and reaches zero conductivity at the resonance frequency.

Figure 2.10 shows the real and imaginary part of the average mobility for a charge carrier (after having divided the conductivity by the charge density  $(en)$ , with  $n$  being the carrier density and  $e$  the charge) in case of an oscillator model with an oscillator frequency in the range of the probe frequency. The graph shows two possibilities: one for high frequency of the oscillator and the

other in case of an overdamped oscillator. This last model usually is used in order to describe a system where the charges are bound as excitons in organic semiconductors or in a situation where trap states are present, as in nanostructured materials (21).

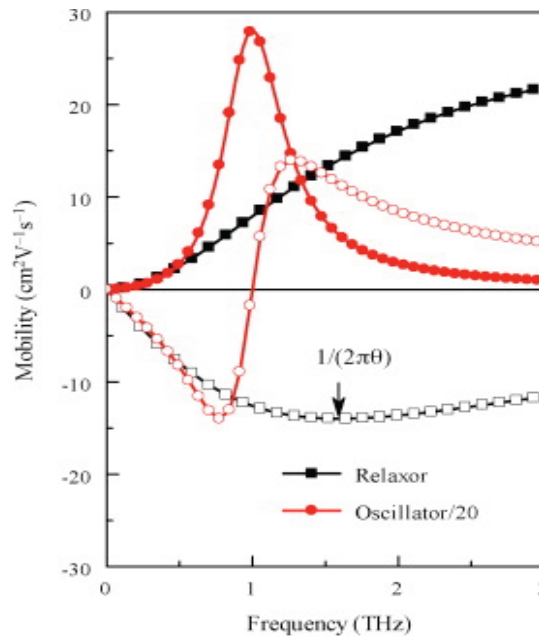


Figure 2.10 Oscillator model describing bound charges for the case of a high frequency oscillator (red) and a damping oscillator (black) (21).

Apart from recent studies, there have been other theoretical models describing the motion of charges in polymers just after the photo-excitation obtained with probing in the THz regime: for example hopping along polymer chains, Monte Carlo simulations, or inter-subband models (20).

## 2.4 References

1. B. Lang, How to Measure a Transient Absorption Spectrum. *Report 2001-2008*.
2. P. Maine, D. Strickland, P. Bado, M. Pessot, G. Mourou, Generation of ultrahigh peak power pulses by chirped pulse amplification. *IEEE J. Quantum Electron.* **QE-24**, 398 (1988).
3. D. F. Zernike and J. E. Midwinter, *Applied Nonlinear Optics*. Wiley, New York, (1937).
4. C. Modoran, *Interaction of Ultrashort Pulses with Transparent Materials*, The Ohio State University. **2005, (thesis)**.
5. R. L. Fork, C. V. Shank, C. Hirlimann, R. Yen, W. J. Tomlinson, Femtosecond white-light continuum pulses. *Opt. Lett.* **8**, 1 (1983).
6. Rullière, *Femtosecond laser pulses: principles and experiments*. **(Springer-Verlag, 1998)**.
7. G. Ghosh, M. Endo, T. Iwasaki, Temperature-dependent Sellmeier coefficients and chromatic dispersions for some optical fiber glasses. *J. Lightwave Technol.* **12**, 1338 (1994).
8. J. Singh, *Optical Properties of Condensed Matter and Applications*. John Wiley & Sons, Ltd, (2006).
9. S. Ramachandran *et al.*, Anomalous dispersion in a solid, silica-based fiber. *Opt. Lett.* **31**, 2532 (2006).
10. S. Akturk, X. Gu, M. Kimmel, R. Trebino, Extremely simple single-prism ultrashort- pulse compressor. *Opt Express* **14**, 10101 (2006).
11. <http://www.swampoptics.com>.
12. S. Yamaguchi, H.-O. Hamaguchi, Convenient method of measuring the chirp structure of femtosecond white-light continuum pulses. *Appl. Spectrosc.* **49**, 1513 (1995).
13. M. C. Beard, G. M. Turner, C. A. Schmuttenmaer, Terahertz Spectroscopy. *J. Phys. Chem. B* **106**, 7146 (2002).
14. P. C. M. Planken, H.-K. Nienhuys, H. J. Bakker, T. Wenckebach, Measurement and calculation of the orientation dependence of terahertz pulse detection in ZnTe. *J. Opt. Soc. Am. B* **18**, 313 (2001).
15. Y.-S. Lee, *Principles of Terahertz Science and Technology*. Springer, (2009).
16. J. T. Kindt, C. A. Schmuttenmaer, Theory for determination of the low-frequency time-dependent response function in liquids using time-resolved terahertz pulse spectroscopy. *J. Chem. Phys.* **110**, 8589 (1999).
17. S. L. Dexheimer, *Terahertz Spectroscopy: principles and applications*. (2007).
18. P. U. Jepsen, D. G. Cooke, M. Koch, Terahertz spectroscopy and imaging - modern techniques and applications. *Laser Photonics Rev.* **5**, 124 (2011).

19. R. Ulbricht, E. Hendry, J. Shan, T. F. Heinz, M. Bonn, Carrier dynamics in semiconductors studied with time-resolved terahertz spectroscopy. *Rev. Mod. Phys.* **83**, 543 (2011).
20. J. Lloyd-Hughes, T.-I. Jeon, A Review of the Terahertz Conductivity of Bulk and Nano-Materials. *J. Infrared, Millimeter, Terahertz Waves* **33**, 871 (2012).
21. H. Nemeč, P. Kuzel, V. Sundstroem, Charge transport in nanostructured materials for solar energy conversion studied by time-resolved terahertz spectroscopy. *J. Photochem. Photobiol., A* **215**, 123 (2010).
22. N. V. Smith, Classical generalization of the Drude formula for the optical conductivity. *Phys. Rev. B: Condens. Matter Mater. Phys.* **64**, 155106/1 (2001).
23. M. Weber, Terahertz Transmission Spectroscopy of Organic Polymer:PEDOT:PSS. *thesis*, (2009).





## **CHAPTER THREE**

# **A Detailed Study of Charge Generation in One- and Two-Phase Microstructures of pBTTT:PCBM**

This chapter has been adapted from the following papers: “**The Influence of Microstructure on Charge Separation Dynamics in Organic Bulk Heterojunction Materials for Solar Cell Applications**” published in Journal of Materials Chemistry A, and “**A Close Look at Charge Generation in Polymer: Fullerene Blends with Microstructure Control**” published in the the Journal of the American Chemical Society.

In this chapter we present the transient absorption results (dynamics and spectra) for one- and two-phase microstructures of pBTTT:PCBM blends. Some time-resolved fluorescence measurements are also shown and compared with the transient absorption results. The chapters 3 and 4 highlight the important role of the microstructure in the process of charges generation/recombination.

### 3.1. Introduction

Early on, it has become clear that the precise arrangement of the donor and acceptor in the bulk heterojunction (BHJ), which we will refer to as microstructure, has strong implications on solar cell efficiency (1). Moreover, the microstructure of the BHJ in most polymer:fullerene blends is much more complex than a simple two-phase scenario of neat polymer and fullerene domains. Amorphous and/or crystalline pure domains often coexist with a phase where the polymer and fullerene are intimately mixed(2-6). In the present chapter, we demonstrate that the mechanism and dynamics of charge generation in polymer:fullerene blends is largely determined by the microstructure.

Numerous empirical strategies to enhance device performance by influencing the microstructure of BHJ thin films during or after their solution-processing have been elaborated (e.g. casting solvent optimization, use of additives, thermal/solvent annealing)(3, 7-12). In an effort to comprehensively correlate the early charge generation events to BHJ structure, we have used femtosecond transient absorption spectroscopy to investigate charge separation (CS) in several systems of pBTTT (poly(2,5-bis(3-hexadecylthiophen-2-yl)thieno [3,2-b]thiophene) and PCBM ([6,6]-phenyl C60 butyric acid methyl ester), with well-characterized BHJ structure.

As discussed already in the Chapter 1, the pBTTT polymer is a particularly suitable model system to study microstructural effects in solar cells. In fact it is known that PCBM molecules intercalate between the side-chains of ordered

polymer domains, forming a co-crystalline phase and providing a structurally well-defined setting for our investigation (2, 5, 13). The first set of samples presented in this chapter consists of blends of pBTTT with various fractions of PCBM.

To change a sample's microstructure means to change its phase, as shown in the following phase-diagram (Figure 3.1):

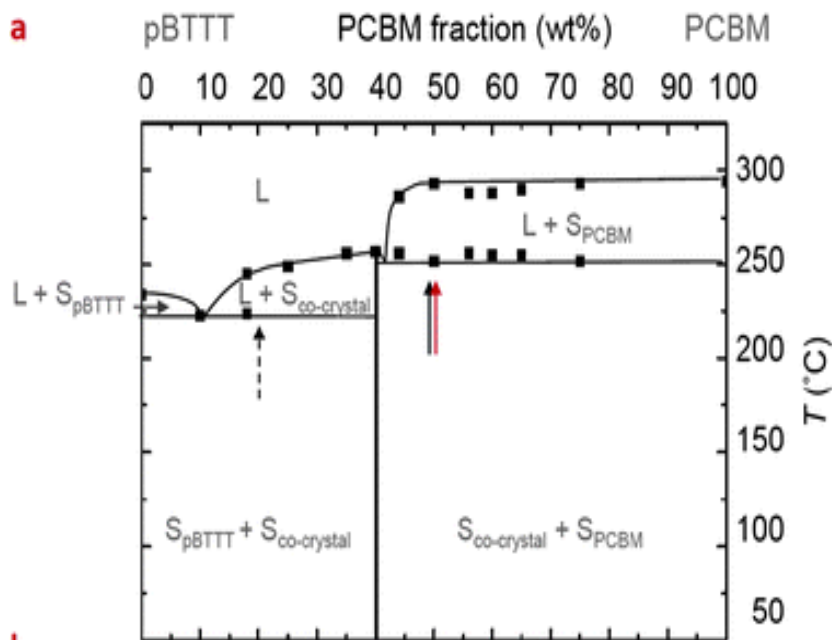


Figure 3.1 Phase diagram showing how the composition of a pBTTT:PCBM blend changes with the weight fraction of the polymer and the PCBM. The co-crystal formation is experimentally determined to occur at a value of 40 % of PCBM content (13).

In this chapter we show results for neat pBTTT films, the 1:1 and the 1:4 blends of pBTTT and PCBM. By selectively exciting either the polymer or fullerene, we have targeted either electron or hole transfer and evaluated the effect of having pure donor or acceptor domains and intermixed regions on both CS pathways. In this chapter, we also highlight how the electro-absorption signature in TA spectra can be used to monitor the charge separation dynamics by targeting the presence of holes in the co-crystalline phase.

## 3.2. Experimental Methods

### 3.2.1. Sample preparation details

The pBTTT polymer ( $M_n = 34$  kDa;  $M_w = 66$  kDa, molecular structure in Figure 3.2) was synthesised as previously reported in Ref. (14) while PCBM for the corresponding blends was purchased from Solenne and used without further purification.

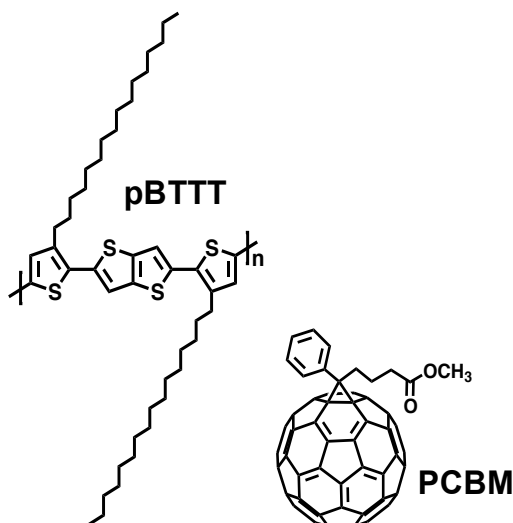


Figure 3.2 Molecular structure of the pBTTT polymer and PCBM

The first set of samples has been prepared from solutions of a pBTTT and PCBM mixture in 1:1 and 1:4 weight ratio in 1,2-ortho-dichlorobenzene (1,2-*o*DCB, Aldrich). The total concentration of the pBTTT:PCBM mixture was 20 mg/mL and 50 mg/mL, respectively. All solutions were left stirring for more than 4 hours at 100 °C to fully dissolve the active material. Films were then deposited on glass by wire-bar coating from hot solutions (~85-90 °C) at 35 °C to ensure the formation of the co-crystals. Prior to measurements, oxygen was removed by keeping the films for 24 hours in vacuum, then they were sealed in an inert measuring chamber.

### 3.2.2. TA spectroscopy: experimental conditions

The TA spectra and the dynamics were recorded using femtosecond pulsed laser pump-probe spectroscopy. The setup used in the experiment was already described in Chapter 2. Excitation at 540 nm was used to excite mainly the polymer in the pBTTT:PCBM blends. For this wavelength, the

pump beam was generated with a two-stage non-collinear optical parametric amplifier (NOPA-Clark, MXR). Alternatively, the samples were excited at 390 nm (where there is significant PCBM absorption), after frequency doubling the fundamental 778 nm beam in a BBO crystal (about 150 fs pulse duration). The broadband probe was in the visible and the n-IR range. The visible and n-IR parts of the spectrum were recorded separately. The probe intensity was always less than the pump intensity ( $< 10$  nJ) and the spot size was much smaller (about 0.2 mm). The pulse energy at the sample was adjusted within the tens of nano-Joule range and the beam diameter was around 1 mm (determined precisely with a BC106-Vis Thorlabs beam profiler,  $1/e^2$  cut-off). For each measurement, identical dynamics at slightly higher and lower power assured complete absence of any intensity-induced bimolecular effects. The fluence (in general  $< 10$   $\mu\text{J}/\text{cm}^2$ ) was adjusted to have a similar flux of absorbed photons for all measurements, taking into account the absorbance at the excitation wavelength and the photon energy. The TA spectra shown here were recorded with a flux of  $1.7 \times 10^{13}$  photons/ $\text{cm}^2$ , where bimolecular recombination effects are negligible. The TA dynamics used for the global analysis were recorded at  $1 \times 10^{13}$  photons/ $\text{cm}^2$ , after ensuring for each sample the complete absence of 1) intensity effects by comparison to the (identical) dynamics at slightly higher and lower power, and 2) degradation.

### 3.2.3. Fluorescence up-conversion spectroscopy

The time-evolution of the fluorescence from the pBTTT and pBTTT:PCBM films was measured on the femtosecond time scale using the fluorescence up-conversion technique. The setup, based on a modified FOG100 system (CDP Lasers & Scanning Systems), used a Mai Tai HP (Spectra-Physics) mode-locked Ti:sapphire laser system to have a tunable excitation wavelength. Its 800 nm or 1000 nm output (100 fs pulse duration, 80 MHz repetition rate) was frequency doubled for sample excitation at 400 nm or 500 nm, respectively. The pump intensity per pulse was about 4 mW, yielding a fluence of 3  $\mu\text{J}/\text{cm}^2$  (with a spot diameter of 50  $\mu\text{m}$ ). Any intensity effects were negligible. The measured sample fluorescence was enhanced by sum-frequency generation with a delayed gate pulse in a non-linear BBO crystal. Phase matching conditions were tuned in order to probe the fluorescence dynamics at different emission wavelengths. The up-converted signal was then dispersed in a monochromator and its intensity measured with a photomultiplier tube operating in the photon counting mode. The polarization of the pump beam was at magic angle relative to that of the gate

pulses. To minimize degradation, the encapsulated samples were continuously rotated during the up-conversion measurements. At least three scans of the dynamics in the -5 ps to 1000 ps range were averaged at each emission wavelength. No degradation of the samples was observed between scans. For each sample, the normalized fluorescence time profiles obtained at various emission wavelengths were analysed globally by adjusting a trial function to the measured data points using a nonlinear least-squares fitting procedure. The dynamics could in all cases be well reproduced by the convolution of a Gaussian-shaped instrument response function (IRF) with the sum of several exponential terms. The width of the IRF was found to be around 100 fs.

### **3.3. Steady-State Spectra of the 1:1 and 1:4 Blends**

The steady-state absorption spectrum of neat pBTTT shows a structureless band around 525 nm, while neat PCBM film absorbs little in the visible range, but mainly below 400 nm (Figure 3.3A). In the 1:1 pBTTT:PCBM blend (by weight) processed by wire bar coating at 35°C, there is quasi complete intercalation of fullerenes, yielding a single intimately mixed co-crystal phase, as schematically shown in Figure 3. 4B (5, 13, 15, 16). Both the PCBM signature and the polymer band are present in the corresponding absorption spectrum. The latter shows a clear vibronic structure and is more red-shifted (maximum at 558 nm) compared to neat pBTTT. This spectral difference can be explained by slightly modified packing and conformational changes of pBTTT in co-crystalline versus neat domains, affecting the intra-versus intermolecular electronic coupling and overall electronic structure (17-20). The excess PCBM present in the 1:4 pBTTT:PCBM blend (by weight) forms relatively pure clusters around the intermixed regions, yielding a two-phase scenario (5, 13, 15).

In the absorption spectrum, the PCBM band is strongly enhanced, while the structured shape of the pBTTT band confirms that the polymer is still present in the co-crystal phase (Figure 3.3 B).

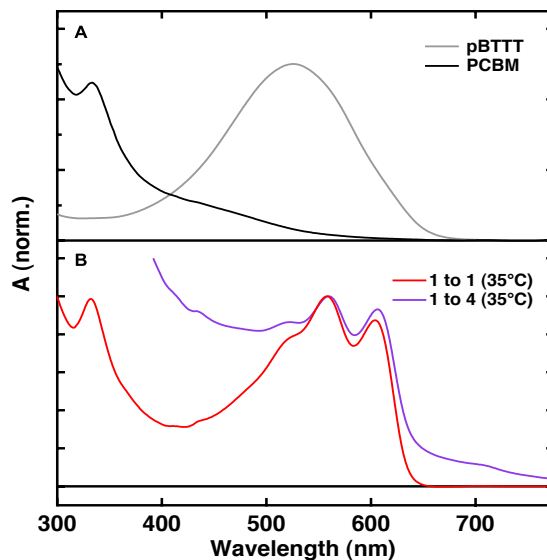


Figure 3.3 Steady-state absorption spectra of the investigated pBTTT, PCBM and pBTTT:PCBM systems. (A) Neat films of pBTTT and PCBM. (B) pBTTT:PCBM blends in 1:1 and 1:4 ratio (by weight), wire bar coated at 35°C.

A schematic representation of the molecular packing in neat pBTTT and the 1:1 pBTTT:PCBM blend is illustrated in Figure 3.4. We can see how the intercalation of PCBM is related to a lattice spacing expansion (about 9 Å) in the direction of the side chains.

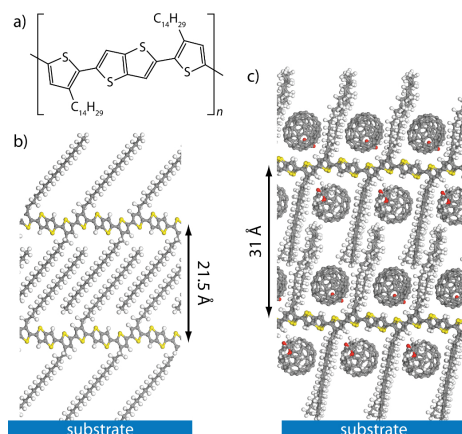


Figure 3.4 (a) The chemical structure of pBTTT, (b) the crystal structure of pBTTT, and (c) the crystal structure of intercalated pBTTT:PCBM co-crystal phase (21).



### 3.4. Transient Absorption Results of Neat pBTTT Films

For neat pBTTT films, the TA spectra show negative signals of ground state bleaching (GSB) and stimulated emission (SE) in the 500-700 nm region, as well as positive excited-state absorption (ESA) rising towards 1000 nm (Figure 3.5A).

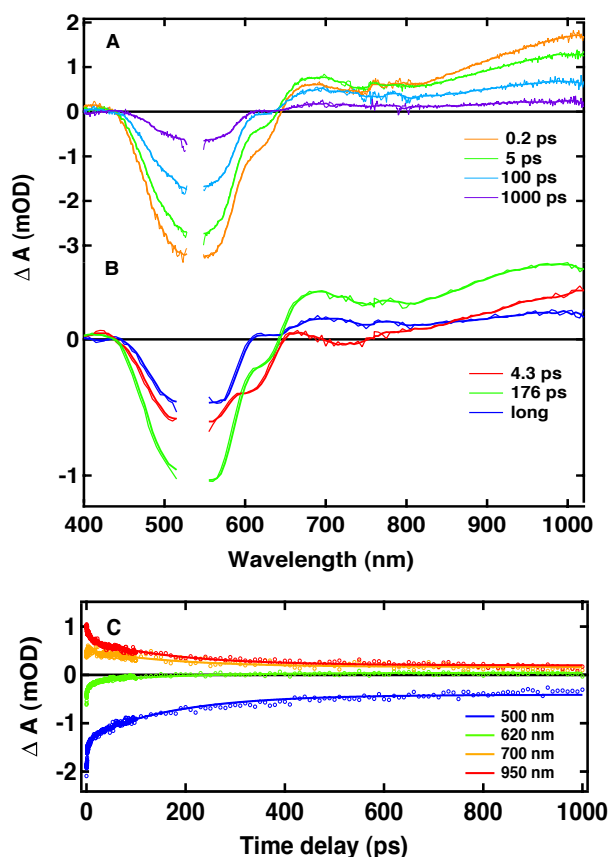


Figure 3.5 TA data for neat pBTTT films. (A) TA spectra recorded at selected time delays following 540 nm excitation. Thicker solid lines are smoothed and overlaid to the raw experimental data. (B) Amplitude spectra associated with the time constants obtained by multi-exponential global analysis of the data. (C) TA dynamics at selected probe wavelengths. The solid lines represent the best multi-exponential fit obtained by global analysis.

The decay of the TA features is essentially biphasic, with a fast component and a slower component in the TA dynamics, shown for selected wavelengths in Figure 3.5C. They were analysed globally (See Appendix 3.9) with time constants of 4.3 ps and 176 ps, yielding respectively the red and green amplitude spectra in Figure 3.5B. The shape of the 4.3 ps amplitude spectrum suggests decay of pBTTT excitons with blue-shifted SE signature. This early

relaxation is caused by ground-state recovery of high-energy polymer segments, as well as by excitation energy transfer to low-energy chromophores, and possibly by geometrical changes in the polymer backbone (22-25). On the other hand, the 176 ps component corresponds essentially to the lifetime of relaxed pBTTT excitons with more red-shifted SE. At long time delays, a plateau is observed in the TA dynamics, due to long-lived TA features with negligible SE contribution and flat absorption above 600 nm (mainly charges and/or the triplet state) (26, 27).

### **3.5. Charge Generation in pBTTT:PCBM Blends**

In this section, we show the photophysics of the 1:1 and 1:4 blends of pBTTT:PCBM. Selected TA spectra for two excitation wavelengths (390 nm and 540 nm) are shown in Figure 3.6 and in Figure 3.8. We discuss separately the differences in the spectra and in the dynamics of the 1:1 and 1:4 pBTTT:PCBM blends in sections 3.5.1 and 3.5.2, respectively.

#### **3.5.1. Charge generation in the 1:1 blend (540 nm and 390 nm)**

We start by considering the 1:1 sample excited with either of two excitation wavelengths: 540 nm or 390 nm. At 540 nm, predominantly the polymer is excited, while mainly PCBM absorbs at 390 nm with a weak Figure 3.6B). At first glance, there is no striking difference between the TA spectra and their evolution recorded at the two excitation wavelengths. The spectra are dominated by a structured negative band in the 480-620 nm region, which coincides with the steady-state absorption spectrum of pBTTT and is therefore assigned to the ground state bleaching (GSB) of the polymer. The presence of the GSB indicates that pBTTT is in a state other than the ground state (e.g. excited, charged, triplet...). There is also a broad positive band extending from 625-1000 nm. This band slightly rises towards the longer wavelengths, and has a pronounced peak around 630 nm (partially overlapping with the GSB; we will later see that this is an electro-absorption signal).

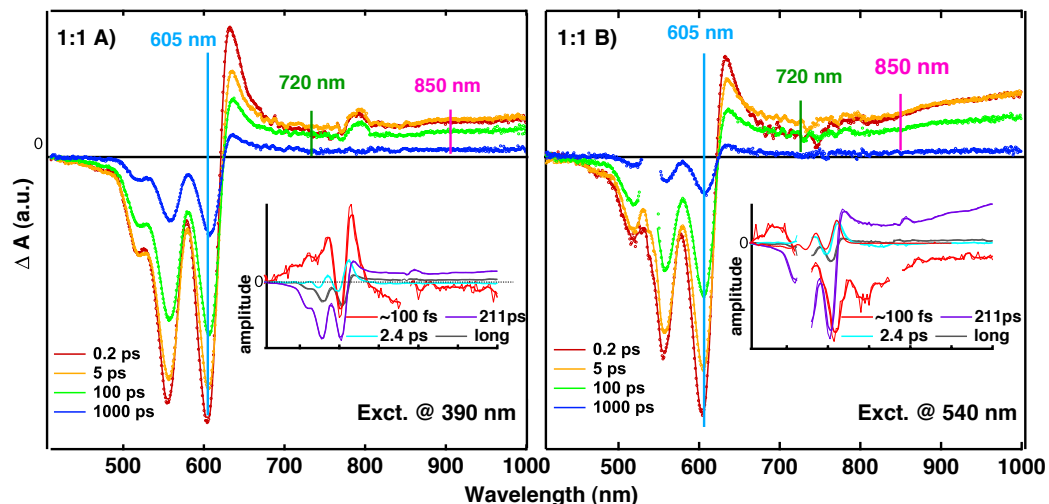


Figure 3.6 TA spectra recorded at selected time delays for pBTTT:PCBM (A) 1:1 blend following 390 nm excitation, (B) 1:1 blend following 540 nm excitation. Thick solid lines are smoothed and overlaid to the raw experimental data (round markers). Noise around 780 nm is caused by remaining fundamental laser light in the probe beam. The insets show the amplitude spectra associated with the time constants obtained by multi-exponential global analysis of the data.

We assign this broad band to absorption from positive charges (polarons) on pBTTT, in good agreement with reported photoinduced absorption (PIA) and charge modulation spectroscopy (CMS) measurements (28, 29). There is little change to the shape of the TA spectra when going from the earliest time delay to the longest (200 fs to 1 ns), and the 630 nm peak is immediately present. This indicates that the majority of charges are formed shortly after excitation at either wavelength.

The occurrence of ultrafast CS in the 1:1 blend is in agreement with the observed TA dynamics shown in Figure 3.7 for selected probe wavelengths in the GSB (605 nm) and charge absorption (720 nm, 840 nm).

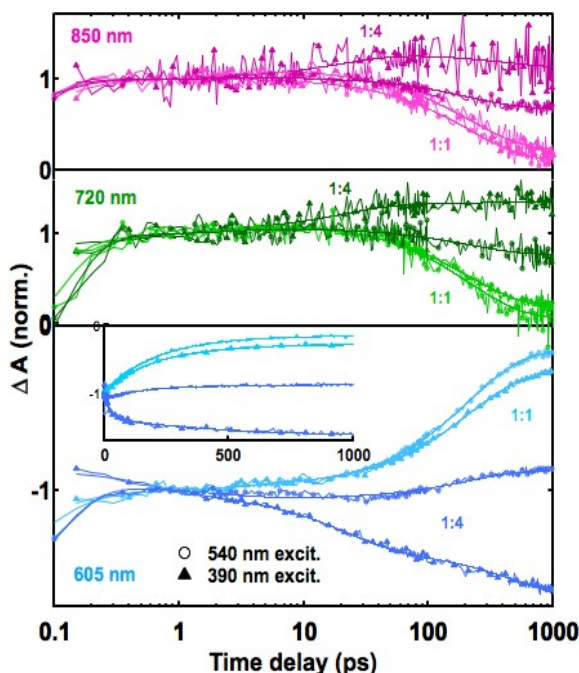


Figure 3.7 TA dynamics at selected probe wavelengths (605 nm, 720 nm and 850 nm) recorded for the 1:1 and 1:4 blends (lighter and darker, respectively) of pBTTT:PCBM following excitation at 390 nm (triangles) or 540 nm (circles). The time profiles were normalized at 1 ps to facilitate comparison. The solid lines represents the best multi-exponential fit obtained by global analysis. Dynamics are shown on a logarithmic time axis, except in the inset

With 540 nm excitation, where our time resolution was as short as 50-60 fs, an ultrafast (<300 fs) component pointing to a rise of charge absorption is visible. We are confident that it is real, since we carefully distinguished it from the signal rise within the laser pulse and verified that there is no interference by artefacts around time delay zero. The **global analysis** confirms that the ultrafast process is observed throughout the TA spectrum and is associated with a time constant of  $\sim 100$  fs. The corresponding amplitude spectrum is shown in the inset of Figure 3.6B in red and further supports the assignment to ultrafast ET from excited pBTTT. Indeed, ET should lead to a disappearance of TA signatures related to the pBTTT exciton (SE and ESA), with concomitant rise of charge absorption. In the amplitude spectrum, the structured negative band to the red side of the GSB, which almost mirrors the latter, is highly indicative of decay of the polymer's SE. In the corresponding 200 fs TA spectrum, the indent in the 670-800 nm region is possibly the remaining tail of this SE. In the amplitude spectrum, the pre-exponential factor related to the  $\sim 100$  fs process is negative all the way up to

1000 ps, suggesting a rise of the charge absorption band, which partly overlaps with the SE. Moreover, the amplitude is positive in the 420-500 nm region, pointing to growth of a negative band, which we assign to the GSB of PCBM based on the coincidence with the steady-state absorption spectrum. ET is expected to lead to a rise of this GSB of PCBM, since the latter is not directly excited, but removed from the ground state via the CS process.

We turn to study what happens with **390 nm** excitation in the 1:1 blend. Although it is mainly the PCBM, which absorbs at this wavelength, the early 250 fs TA spectrum, shown in Figure 3.6A is dominated by the GSB of the polymer and by charge absorption. This suggests that ultrafast CS has already occurred, this time mainly by HT from photoexcited fullerene, involving the HOMO levels of the donor and acceptor. It has been previously established that HT in polymer:fullerene blends can be as fast as 30 fs (30). Given the lower time resolution that we have at 390 nm (150 fs), it is difficult to resolve the process. Still we could identify the tail of the ultrafast dynamics at the earliest time delays and analyse them roughly using a  $\sim 100$  fs time constant. The predominantly positive sign in the 430-650 nm region of the corresponding amplitude spectrum points to an increase of the polymer's GSB, as expected during HT (inset of Figure 3.6A). The negative amplitude at higher wavelengths is representative of rise of the charge absorption and may include some decay of the SE of pBTTT during ET, since the polymer is also slightly excited at 390 nm. The oscillatory part in the amplitude spectrum is related to the evolution of the electro-absorption signal, as discussed later.

We relate the ultrafast ( $\sim 100$  fs) charge formation by ET and HT in the 1:1 pBTTT:PCBM blend at both excitation wavelengths to a static quenching process (no exciton diffusion), given the close proximity of the donor and acceptor in the intimately mixed co-crystal phase. This is in excellent agreement with reported steady-state and time-resolved emission quenching studies (13, 31). There has been a lot of recent discussion that ultrafast CS in polymer:fullerene blends might compete with relaxation and occur from hot, highly delocalized states (23, 32-34). Our results are not in contradiction with such a mechanism.

The evolution of the charges in the 1:1 blend at longer times can be followed by considering the dynamics in Figure 3.7. There is decay on the hundreds of picosecond time scale of both the charge absorption (720 nm, 850 nm) and the polymer GSB (605 nm), pointing to recombination. The observed

recombination is geminate (gCR), since it is independent of pump intensity. This gCR results from electron-hole pairs that have dissociated within the co-crystalline phase (where the fullerene and polymer are molecularly mixed and hence, in close proximity), but cannot overcome the Coulomb force still binding them together in a charge transfer (CT) state. Only a small fraction of the charges survive beyond the 1 ns time window, as shown by the weak long-lived plateau in the dynamics. The dynamics with 390 nm and 540 nm excitation are quite similar (they were normalized at 1 ps for better visualization), showing that the fate of charges generated by ET and HT is comparable. By global analysis, we estimate in both cases an average time scale of 211 ps for the gCR, with the associated amplitude spectrum essentially showing the decay of the GSB and charge signatures (purple curves, insets of Figure 3.6). The much weaker grey amplitude spectrum of similar shape represents the plateau due to the population of long-lived charges. Ultrafast formation of free charge carriers via hot CT states, as opposed to dissociation of the relaxed CT state, has been intensively discussed in literature (35-38). Although we cannot distinguish between the two mechanisms, it is clear that neither is efficient in the fully intercalated polymer:fullerene microstructure, where gCR is favoured, leading to a low yield of free charges.

Finally, we note the apparent higher remaining polymer GSB signature with 390 nm excitation at 1 ns, leading to the small differences in the dynamics recorded at the two pump wavelengths (Figure 3.6, Figure 3.7). Two reasons could account for this observation. First, it has been shown that the yield of free charges, and thus the fraction of bound charges undergoing gCR, can depend on the generation pathway by ET or HT if the driving force for the two processes is very different (39). A larger driving force for HT in pBTTT:PCBM might therefore lead to a slightly weaker contribution of gCR. Nevertheless, many other studies disprove a wavelength dependence of free charge generation (see Chapter 1). More probably, the occurrence of some delayed HT components at 390 nm causes a rise of the GSB and charge signals that partly counterbalances the decay of those features due to gCR. The decay of the signatures related to the fullerene exciton is not expected to be useful to identify delayed HT, since their amplitude is very weak and most probably drowned by the intense polymer bands (40).

**Careful inspection** of the TA spectra of the 1:1 blend in Figure 3.6 reveals a slight (about 4 nm) red shift of the peaks related to the polymer GSB. This

shift leads to dynamics that we could reproduce globally with a 2.4 ps time constant. The corresponding amplitude spectrum (cyan in the insets of Figure 3.6) is present at both excitation wavelengths and has an oscillatory shape. As will be discussed in section 3.6, it is related to decay of the electro-absorption signal peaking at 630 nm. We note that the red shift of the polymer's GSB into the overlapping positive 630 nm band also occurs during the ultrafast CS processes. This causes for example the oscillatory shape around 615 nm in the amplitude spectrum of the  $\sim 100$  fs time constant with 390 nm excitation (inset of Figure 3.6A).

### 3.5.2. Charge generation in the 1:4 blend (540 nm and 390 nm)

The TA spectra of the 1:4 pBTTT:PCBM blend upon 540 nm excitation of predominantly the polymer are shown in Figure 3.8B.

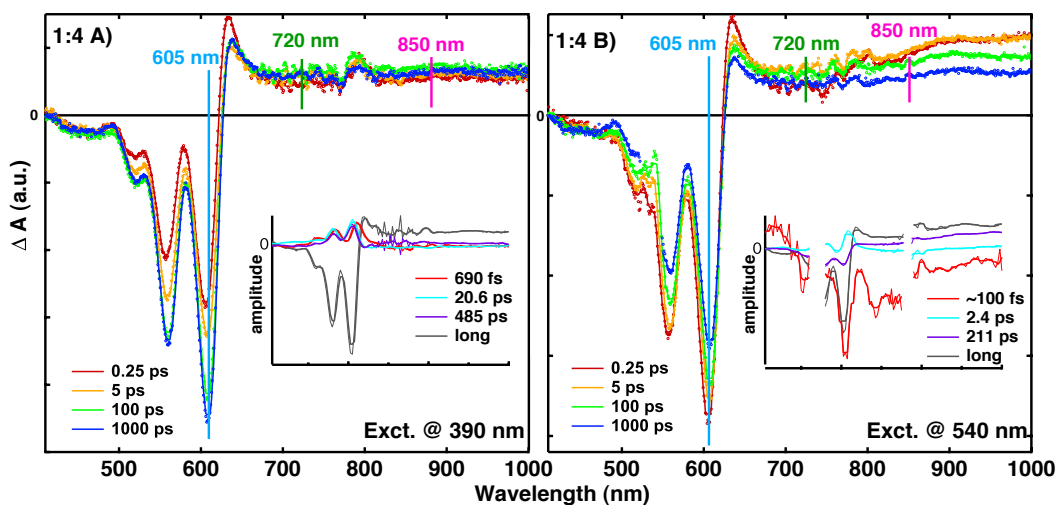


Figure 3.8 TA spectra recorded at selected time delays for pBTTT:PCBM (A) 1:4 blend following 390 nm excitation, (B) 1:4 blend following 540 nm excitation. The insets show the amplitude spectra associated with the time constants obtained by multi-exponential global analysis of the data.

The shape is very similar to the one recorded in the 1:1 blend (except for a more pronounced fullerene GSB around 450 nm due to high PCBM loading). The early appearance of the charge signatures points again to ultrafast ET. Indeed a short (hundreds of femtoseconds) component is visible in the dynamics of the 1:4 blend (Figure 3.8) and could again be globally reproduced with a  $\sim 100$  fs time constant. The amplitude spectrum is very similar to the corresponding one in the 1:1 sample, characteristic of ET (inset of Figure

3.8B) The slower 2.4 ps process (related to decay of the electro-absorption, see section 3.6), leading to a red shift of the polymer GSB and an oscillatory amplitude spectrum, is again present in the 1:4 sample. Overall, the results show that ET is very efficient and fast in both the 1:1 and 1:4 blends, because the pBTTT chains are in both cases in close proximity to the intercalated PCBM molecules.

Differences only appear at longer time scales. From the TA spectra and the dynamics (Figure 3.7, Figure 3.8), it is immediately clear that the loss of charges due to gCR is significantly reduced in the 1:4 blend. This is further confirmed by the decreased weight of the amplitude spectrum associated with the 211 ps gCR component (in purple, inset of Figure 3.8B), and the enhanced weight of the long-lived charges (in grey). The presence of the pure fullerene clusters thus increases the yield of long-lived free charge carriers. This is in excellent agreement with higher solar cell efficiency in the 1:4 blend, (5) and with previous TA, PIA and microwave conductivity results, mostly recorded at much longer times than the femtosecond results presented here (13, 28, 31, 41). The high electron mobility in the pure fullerene domains and increased electron affinity compared to intercalated PCBM provide a driving force for the spatial separation of charges formed by exciton dissociation in the co-crystals (13, 31).

We will now consider what happens in the **1:4 blend with 390 nm** excitation (Figure 3.8A). Given the high PCBM content of the sample, mainly fullerenes (both in the co-crystal phase and in relatively pure clusters) are excited. The early 250 fs TA spectrum shows the polymer's GSB and the charge absorption, indicating that some ultrafast HT has already occurred within the time resolution, most probably from the intercalated PCBM molecules (as in the 1:1 blend). The subsequent evolution of the spectra is however very different than what is observed in the other three measurements. In particular, there is a progressive increase of the pBTTT GSB, as the polymer's charged state is indirectly populated by delayed HT. The process is slow, because it concerns excitons that are generated in the pure PCBM clusters and need to diffuse towards pBTTT in the co-crystal regions. There is also a weak rise of the charge absorption band above 700 nm. This rise might be partially obscured by the overlapping flat absorption of the decaying PCBM exciton (40). Unlike the dynamics of the 1:1 blend, which are quite similar for both excitation wavelengths, the differences in the 1:4 blends are much more pronounced (Figure 3.8). With 390 nm excitation, there is a multiphasic



increase of the GSB at 605 nm, which continues beyond the 1 ns time window. An increase is also seen in the charge absorption (720 nm, 850 nm), but it competes at long time delays with a weak decay due to gCR, as was observed upon 540 nm excitation.

For the global analysis, three largely different time constants (690 fs, 20.6 ps and 485 ps) were necessary to reproduce the dynamics due to delayed HT in the 1:4 blend with 390 nm excitation. This is most likely a crystallisation of a much broader distribution of time constants related to the process (42). The corresponding amplitude spectra are characterized by a structured positive band mirroring the GSB signal (inset of Figure 3.8A). The shift of the fastest (690 fs) component suggests entanglement with the red shift of the GSB clearly seen in the TA spectra (Stark effect). The strongly multiphasic dynamics of the delayed HT originates from a variety of distances of the excitons generated in the PCBM clusters from the co-crystal regions. It is likely that not all excitons reach a pBTTT quencher during their lifetime (as previously suggested by incomplete quenching of the fullerene emission), especially if the PCBM domains are larger than the 5 nm exciton diffusion length (13, 43). Although we have discussed HT as splitting of a PCBM exciton in the presence of pBTTT, we cannot exclude the alternative scenario of hole injection into the polymer following spontaneous charge dissociation within the PCBM clusters and charge migration (this would lead to similar evolution of the TA spectra). The process has been demonstrated, (44, 45) but is probably slower than what we observe here and therefore has a minor influence on our results (46).

## **3.6. Stark effect in the TA data of the 1:1 and 1:4 Blends**

### **3.6.1. Theoretical background about the Stark effect**

Close inspection of the TA spectra presented above has revealed the presence of an oscillatory signal resembling the first derivative of the steady-state absorption spectrum superposed to the red side of the GSB and displaying a characteristic positive peak at 630 nm. We will explain now that this is related to an electro-absorption signature caused by the presence of charges in the co-crystal phase of the 1:1 and 1:4 blends. We start by introducing a theoretical background about the Stark effect.

In general, an electric field (E) perturbs the absorption spectrum of a molecule by shifting the energy levels of the ground and/or excited state (Stark effect), by breaking the symmetry allowing otherwise forbidden transitions, or by ionizing the excited state (47). We focus here on the Stark effect, which occurs if there is a change of permanent dipole moment ( $\Delta p$ ) and/or of polarizability ( $\Delta\alpha$ ) between the ground and excited states, leading to an energy shift of the transition. The electro-absorption (EA) is defined as the difference of the absorption spectrum in the presence ( $A^E(\nu)$ ) and absence ( $A(\nu)$ ) of the electric field. It can be expressed as a series of first, second and higher order derivatives of  $A(\nu)$  (47):

$$EA = A^E(\nu) - A(\nu) = -\frac{\partial A(\nu)}{\partial \nu} \Delta p E - \frac{1}{2} \frac{\partial A(\nu)}{\partial \nu} \Delta\alpha E^2 + \frac{1}{2} \frac{\partial^2 A(\nu)}{\partial \nu^2} (\Delta p E)^2 + \dots$$

The first term (linear in E) cancels in isotropic media, the second term (quadratic in E) shows that changes in polarizability are related to the first derivative of the absorption spectrum, and the third term associates changes in the permanent dipole moment to the second derivative of  $A(\nu)$ .

In TA spectroscopy, the absorption difference ( $\Delta A$ ) of the sample with and without excitation by the pump is measured, thus in the presence and absence of photo-generated charges in the case of the pBTTT:PCBM blends. If a Stark effect is caused by those charges, an EA contribution is seen in the TA data. In contrast to the case where a uniform electric field is externally applied across the bulk of the film using electrodes (48-50), the Stark effect in the TA data depends on the local radial electric fields around free charges and the local electric dipoles around electron-hole pairs. The EA signature in the TA data can be exploited to determine in which phase of the blend the charges are generated and how they spatially separate.

### 3.6.2. Assignment of the electro-absorption signal (1:1 blend)

We have demonstrated that ET from photoexcited pBTTT to intercalated PCBM molecules is prompt for the 1:1 blend excited at 540 nm. Therefore, only the signature of charges (not of excitons) is present in the TA spectra of Figure 3.6B. In addition to the expected GSB below 620 nm and the flat absorption of positively charged pBTTT above 620 nm, an oscillatory signal superposes to the red side of the GSB and displays a characteristic positive peak around 630 nm. We have also noticed a red shift of the GSB occurring during the ultrafast CS as well as with a 2.4 ps time constant. A red shift of the polymer GSB in a fullerene blend has been previously reported and explained

by migration of charges to lower energy sites within an inhomogeneous density of states (38). This process is however too slow to account for what we are observing here. Therefore, we ascribe the shift of the GSB to the evolution of the oscillatory signal peaking at 630 nm. We assign the oscillatory signal to an electro-absorption (EA) signature, caused by changes in the pBTTT absorption spectrum that occur because of the electric field generated by the presence of charges (**Stark effect**) (29, 51). Indeed, during the global analysis we found a particular oscillatory shape of the 2.4 ps component present in the amplitude spectra with 390 nm and 540 nm excitation of the 1:1 blend (insets of Figure 3.6). The strong similarity of the 2.4 ps amplitude spectrum (cyan in Figure 3.9) with the first derivative of the steady-state absorption spectrum of the 1:1 blend (black) further supports the involvement of the Stark effect.

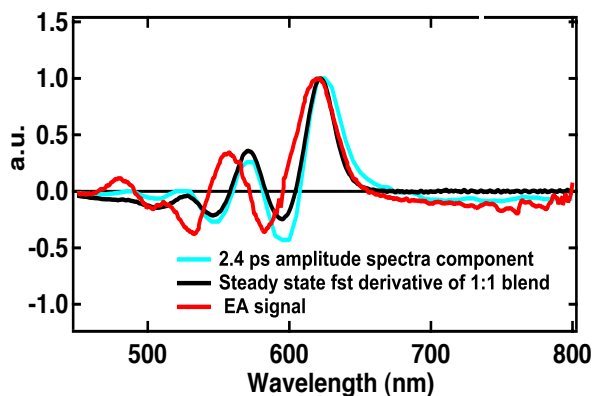


Figure 3.9 First derivative of the steady-state absorption spectrum (black) of the 1:1 blend, the electro-absorption spectrum measured in a solar cell with an applied bias of 6 V (red), and the amplitude spectrum associated with the 2.4 ps time constant obtained by global analysis of the TA data (cyan).

We have confirmed this assignment by directly measuring the EA spectrum obtained by sandwiching the 1:1 and 1:4 films between electrodes in solar cell devices, with an externally applied uniform electric field of  $6 \cdot 10^5$  V/cm (red curve in Figure 3.9). The EA spectrum is very similar to the oscillatory signature peaking at 630 nm in the TA spectra (Figure 3.6) and to the 2.4 ps amplitude spectrum (Figure 3.9). After changing the external electric field between  $2 \cdot 10^5$  V/cm and  $6 \cdot 10^5$  V/cm, we realized that the EA amplitude measured in the device at 620 nm varies quadratically with the externally applied bias, as shown in Figure 3.10.

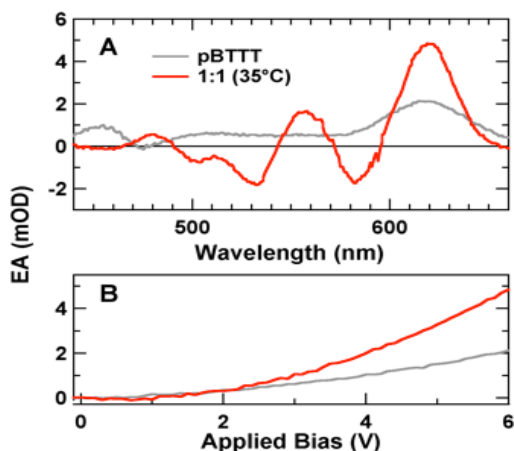


Figure 3.10 A) Electro-absorption spectra measured on solar cell devices of neat pBTTT and the intercalated 1:1 (35°C) pBTTT:PCBM blend, with 6V applied bias. (B) Quadratic dependence of the EA amplitude at 620 nm as a function of externally applied voltage bias. There is indication that the EA spectrum of neat pBTTT is weaker and less sharp than for the 1:1 blend.

We are thus observing a quadratic Stark effect (the transition shifts with  $E^2$ ). Since the EA spectrum of the 1:1 blend shows similarity to the first derivative of the absorption, the main origin of the Stark effect is a change in polarizability between the ground and excited state of pBTTT.

As discussed above, the 630 nm feature in the TA spectra of the 1:1 blend is assigned to a typical electro-absorption (EA) signature caused by the Stark effect, when the electric field generated by charges in the blend shifts the absorption of neighbouring polymer chains (47, 52). It is noteworthy that the EA signature observed in the TA data of the 1:1 blend is instantaneously present at the shortest time delays (Figures 6 A),B)) although the charges generated by prompt CS in this highly intermixed, fully intercalated system must be in close proximity and are presumably significantly bound.

We can explain our observations in the 1:1 blend using simple electrostatic considerations applied to the particular geometry of the pBTTT:PCBM co-crystal phase (20) (see section 3.9.1). Since the local field generated by a charge decays with distance ( $a$ ) according to  $1/a^2$  (and  $E^2$  decays even faster with  $1/a^4$ ), only the pBTTT chromophores located in closest proximity to a charge will experience a significant Stark effect. In the co-crystal phase, the initially generated dipole related to the electron-hole pair is perpendicular to the pBTTT backbones (by inspection of the crystal structure in Figure 3.4B). The polymer segments closest to a charge (which will dominate the EA

response), are the ones located on both sides of the hole on the same chain, and the ones on the chains  $\pi$ -stacked above and below the hole. The field generated by the hole across the lamella spacing of  $\sim 3$  nm is much weaker (20). Similarly, the effect of the field around the electron is small on the pBTTT chromophores, as it will mainly affect the close-by fullerene molecules. Electrostatic simulations (section 3.9.1) show that the field felt by the relevant polymer segments next to the hole vanishes if the electron-hole distance approaches zero. However, if we assume an initial charge separation distance of 1 nm (which is reasonable based on the size and arrangement of the pBTTT and PCBM molecules) (52), the field at the relevant positions is already significant and explains the presence of the EA signature in the TA spectra of the 1:1 blend at early time delays. In fact, the polymer segments located at a distance of about 0.2-0.5 nm away from the hole in the co-crystal geometry experience an electric field very close to the one created around a free hole.

### 3.6.3. Evolution of the EA signature in the 1:1 blend (540 nm)

Coming back to the 2.4 ps amplitude spectrum for the 1:1 blend excited at 540 nm, we can deduce that there is a decay of the EA with the 630 nm peak in the corresponding TA spectra. Indeed in the TA spectra, the time evolution of the 630 nm peak is clearly evident (Figure 3.6B). It decays slightly on the 2.4 ps time scale, but does not completely vanish, since it is still clearly visible at the longest (1 ns) time delay. From the global analysis we can also say that the generated charges undergo gCR on the 211 ps time scale. We tentatively ascribe the 630 nm peak decay to some relaxation of the charges (for example a change in the extent of delocalization of the hole), or to migration of some charges (which do not geminately recombine) within the co-crystal region.

The physical mechanism behind the decay of the EA with the 2.4 ps time constant might be explained by relaxation from an excited level of the electron-hole pair (excited level of the charge transfer (CT) state) to the lowest level of the CT state. Hence the excited CT states create a dipole generating an electrostatic field able to trigger a Stark effect in the surrounding polymer chains. Indeed, the photo-generated charges in polymer:fullerene blends create important electric fields in their vicinity, which can have strong effects on the optical transitions of neighbouring chromophores.(52) The typical shape of the EA feature with the 630 nm peak is representative of crystalline microstructures, as has been recently found with TA experiments in other crystalline materials.(53) Comparing the

dynamics at 625 nm (EA peak) and 605 nm (GSB) in 1:1 blends shown in Figure 3.11, we can further support that the nature of the decay taking place in the EA is different from the one at 605 nm. In fact the GSB decay is describing a recombination of electron-hole pairs to the ground state in 211 ps due to gCR, while the EA peak decay is describing a decay from an excited CT state to the lowest CT level.

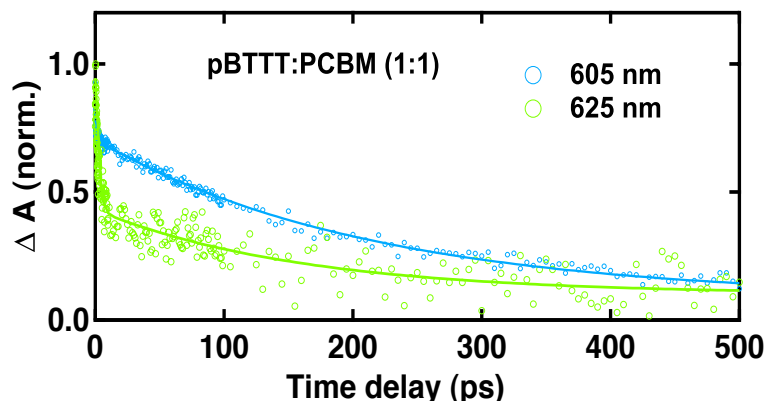


Figure 3.11 Comparison between the dynamics at the GSB (605 nm) and the EA feature (625 nm).

#### 3.6.4. EA in the 1:1 blend for 390 nm and 540 nm excitation

As seen in Figure 3.6, the EA signature (with the 630 nm peak) is present in the TA spectra of the 1:1 blend with 540 nm and 390 nm excitation. The presence of oscillations in the 100 fs amplitude spectrum indicates that there is some evolution of the EA on the ultrafast time scale (during the CS process by ET or HT). Within a first look at the spectra, it is clear that the 100 fs component is different according to the excitation wavelength: the 100 fs component for 390 nm excitation has a different shape from the one for 540 nm excitation. For 390 nm excitation, there seems to be a strong enhancement of the typical oscillations due to the EA signature. Differently from the 2.4 ps amplitude spectrum, the 100 ps component has a larger amplitude of the oscillations as shown in Figure 3.12A. This seems to suggest that the process of HT in the polymer is different from the ET. It is possible that in the process of HT, the generated electron-hole pair at the interface is more delocalized. Thus the generated electric field and the amplitude of the EA is initially higher (during about 100 fs). This is confirming the concept that the hole has a higher mobility with respect to the electron in the co-crystal

phase, as has been recently found by McGehee et al. (52). At longer time delays, the evolution of the EA signal with 390 nm and 540 nm excitation is very similar (with the typical 2.4 ps decay, Figure 3.12).

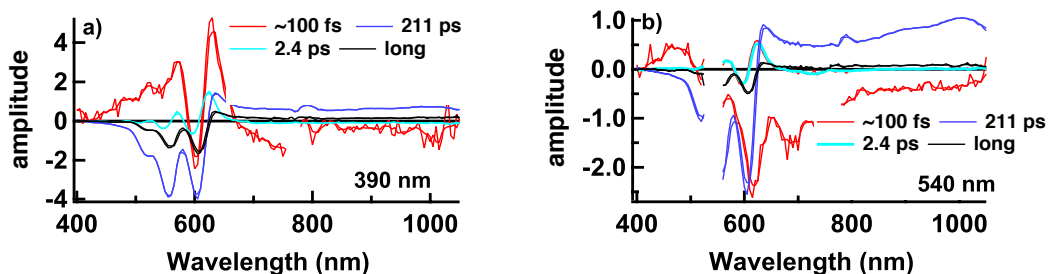


Figure 3.12 Amplitude spectra obtained by global analysis of 1:1 blends for excitation wavelengths of a) 390 nm and b) 540 nm. In both measurements, the 2.4 ps component (having a shape resembling to the first derivative of the 1:1 blend steady state absorption) is evident.

### 3.6.5. Evolution of the EA signature in the 1:4 blend

The characteristic 630 nm feature is present also in the 1:4 samples excited at 540 nm or 390 nm (Figure 3.8). The 630 nm feature can be recognized, also for the 1:4 blend, as a typical EA signal. The evolution of the EA signal is similar to the one found for the intercalated 1:1 blend without neat fullerene regions. It appears in both cases instantaneously, then slightly decays within 2.4 ps,(15) and remains significantly present for free charges at long time delays (see 1 ns spectra). This is surprising, since we have seen that the presence of neat PCBM clusters in the 1:4 blend provides a driving force for spatial charge separation and significantly prevents gCR within the time window of our experiment. We can again explain this observation by considering the molecular geometry around the photo-generated charges (electrostatic considerations in section 3.9.1). For the initial electron-hole pair in the co-crystal phase, the pBTTT segments most affected by the Stark effect experience an electric field comparable to the one around a free hole (i.e. the influence of the electron is negligible at their position, see discussion for the 1:1 blend). There is therefore not a large difference in the EA amplitude when the charges effectively separate thanks to the PCBM clusters. The observed 630 nm EA signature for pBTTT is thus independent of whether the electrons stay in the co-crystals or not, but it is related by the presence of (bound or free) holes on polymer chains in the co-crystal regions.

We tentatively suggest that the origin of the 630 nm signal is also partly due to the presence of hot electron-hole pairs at the interface between fullerene/intermixed phase. In the first 200 fs, the binding energy is overcome, thanks to the large fullerene domain. During this period of time, the electron-hole pair behaves as a strong dipole which generates a field. This field is at the origin of the Stark effect in the neighbouring polymer chains. After the first 200 fs, the decrease of the 630 nm peak amplitude (less oscillator strength) is probably indicating the generation of polarons.

### 3.7. Fluorescence Spectroscopy Results

The main TA results previously shown for the 1:1 and 1:4 blends are confirmed by time-resolved emission spectroscopy, as we discuss in the next paragraph.

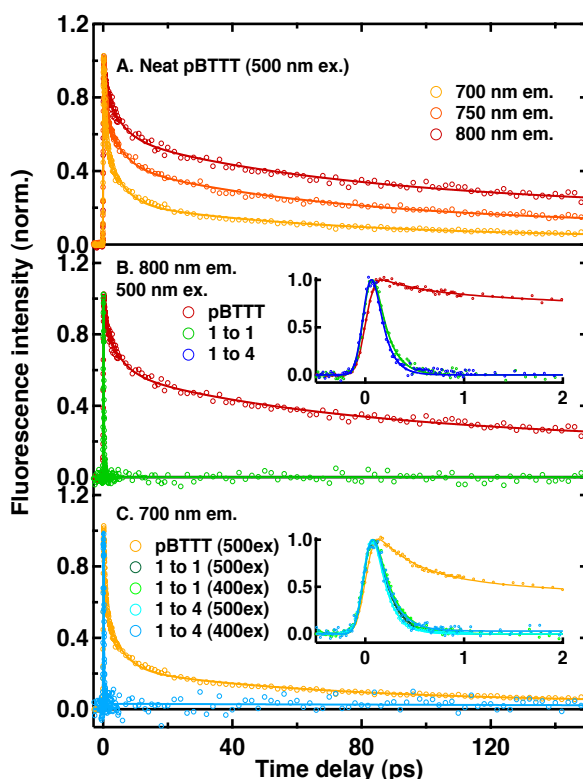


Figure 3.13 Femtosecond fluorescence dynamics obtained by the up-conversion technique. (A) Neat pBTTT film at various emission wavelengths following excitation at 500 nm. (B) Emission at 800 nm for neat and blend films (1:1 and 1:4, processed at 35 °C), following excitation at 500 nm. (C) Emission at 700 nm for the neat and blend films, following excitation at 400 nm or 500 nm. Solid lines are the best multi-exponential fit from global analysis.



For neat pBTTT films, the complex excited state behaviour seen in the TA data (section 3.4) is confirmed by strongly multiphasic fluorescence dynamics, measured by femtosecond up-conversion spectroscopy upon 500 nm excitation (Figure 3.13A).

Time constants of 0.4 ps, 4.9 ps, 62 ps and 600 ps were necessary to globally reproduce the dynamics at emission wavelengths between 700 nm and 800 nm. The enhancement of the fast components at shorter emission wavelengths is typical for a red shift of the fluorescence spectrum, caused in this case by the fast exciton decay for the high-energy chromophores.

A major result found for the pBTTT:PCBM blends is that the pBTTT excitons in the 1:1 and 1:4 samples dissociate into charges on the ultrafast  $\sim 100$  fs time scale, given the proximity of the polymer and fullerene in the co-crystal phase (no exciton diffusion is necessary, see section 3.5). This important result also perfectly agrees with the emission spectroscopy.

The time-resolved emission dynamics with 500 nm excitation (Figure 3.13B) confirm this prompt quenching of the 800 nm polymer fluorescence within 130 fs and 110 fs for the 1:1 and 1:4 blend, respectively (a convolution with the 100 fs instrument response function was used and it is likely that even faster quenching components are missed). The higher-energy emission at 700 nm (Figure 3.13C) also decays with 150/180 fs (1:1 blend) and 130/150 fs (1:4 blend), following excitation at 500/400 nm. With 400 nm excitation, there is a weak contribution of PCBM emission,<sup>(54)</sup> which is quenched by HT to pBTTT. The TA study has revealed this process to be prompt in the 1:1 blend ( $\sim 100$  fs), but to have a distribution of ultrafast to slow components (ranging from sub-ps to  $\sim 500$  ps) in the 1:4 blend due to diffusion of PCBM excitons to a quenching site through the fullerene clusters. This causes the weak offset at long time delays in the emission dynamics of the 1:4 blend excited at 400 nm.

### **3.8. Conclusion**

We have demonstrated a precise correlation between the early charge generation mechanism and the phase morphology of polymer:fullerene bulk heterojunction blends. The rate of electron and hole transfer was determined by femtosecond absorption and emission spectroscopy. The investigated pBTTT:PCBM samples could be classified into distinct categories according to

their microstructure and charge separation mechanism. We have discussed in this chapter the first two categories:

**One-phase, fully intercalated blend** (1:1 pBTTT:PCBM blend processed at 35 °C): Both electron and hole transfer occur on the < 100 fs time scale, since no exciton diffusion is necessary within the single co-crystal phase. However, a majority of the electron-hole pairs recombines geminately within 200 ps.

**Two-phase microstructure** comprised of co-crystalline regions and PCBM clusters (1:4 pBTTT:PCBM blend processed at 35 °C): Electron transfer is prompt, while hole transfer can be prompt or delayed depending on whether excitons are generated in the intercalated or neat PCBM regions. Geminate charge recombination in the co-crystal phase is significantly reduced due to efficient migration of electrons towards fullerene clusters, favouring spatial separation of electron-hole pairs.

## 3.9. Appendix - Theoretical Methods

### 3.9.1. Electrostatic Simulations

In order to better understand the evolution of the EA signature observed in our TA data, we use simple electrostatic considerations applied to the particular geometry of a pBTTT:PCBM co-crystal phase. The EA signature most visible in the TA spectra (600-650 nm region) stems from transitions in pBTTT, while the weaker contribution of PCBM is masked by the GSB of the polymer. We will therefore limit the discussion to the EA induced in the polymer chains by photo-generated charges. We neglect the effect of the field generated by the negative charge (electron) on the pBTTT chromophores, as this will mainly affect the close-by fullerene molecules. We treat the charges as point charges and do not take into account their delocalization in the PCBM clusters or polymer chromophores.

In its proximity, the positive charge will dominate the field experienced by neighboring chromophores. When the hole can be considered as a free charge (i.e. when the electron is sufficiently far), the electric field around the hole will radiate outwards uniformly in all directions ( $a$  is the distance from the charge,  $q$  is the unit charge ( $1.6 \cdot 10^{-19}$  C) and  $\epsilon_0$  is the permittivity of free space ( $8.85 \cdot 10^{-12}$  As/Vm, we did not correct for polymer medium)):

$$|\vec{E}_{free}^+| = \frac{q}{4\pi\epsilon_0} \left( \frac{1}{a^2} \right) \quad 1)$$

When the electron approaches the hole, it will perturb the field around the positive charge depending on how close it is (the distance between charges is denoted as  $d$ ). By using vector addition, we will calculate the magnitude of the electric field as a function of  $d$  in the vicinity of the positive charge (the EA scales with the square of this field, thus its direction does not matter). We consider positions A and B (aligned with the dipole formed by the two charges, looking either between the charges or on the other side of the hole), as well as position C (in the plane perpendicular to the dipole). Finally, position D is also perpendicular to the dipole, but in the plane taken in the middle of the two charges. They are shown in Figure 3.14:

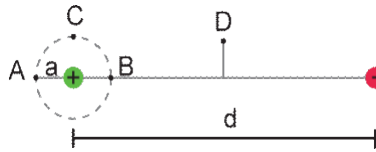


Figure 3.14 Schematic representation of the electron and hole at a distance  $d$ , and of the different possible position where the generated field affect the polymer surrounding the hole.

We discuss in this chapter only the positions C and D because as shown above, the polymer segments closest to the hole, which will dominate the EA response, are the ones located on both sides of the positive charge on the same chain, and the ones on the chains  $\pi$ -stacked above and below the hole. They are thus all in position C with respect to the electron-hole dipole (in the plane perpendicular to it). There are no polymer segments between the two charges (position B), and the ones in position A are separated by the lamella spacing distance, and thus too far away to significantly contribute to the EA. There might be some contribution from position D, if the polymer chains are not perfectly straight.

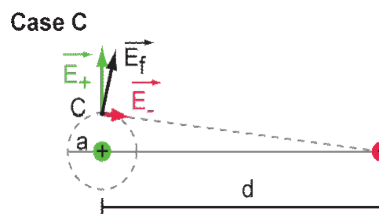


Figure 3.15 Resultant field generated by an electron-hole pair at distance  $d$  in the position C.

In position C, the fields due to the positive and negative charge are almost perpendicular. The effect of the negative charge is to weakly tilt the field in its direction and to slightly reduce its magnitude. Close to the hole (when  $a$  is small), the perturbation caused by the negative charge is much less pronounced than in positions A and B. It becomes more pronounced with increasing  $a$ . The field at position C vanishes when the distance  $d$  between the charges tends to zero, and increases with  $d$  towards the value of the free hole. The resultant field is described in formula 2 and the simulations are shown in Figure 3.16.

$$|\vec{E}_{tot}^C| = \frac{q}{4\pi\epsilon_0} \sqrt{\left(\frac{1}{a^2} - \frac{a}{(a^2 + d^2)^{3/2}}\right)^2 + \left(\frac{d}{(a^2 + d^2)^{3/2}}\right)^2} \quad 2)$$

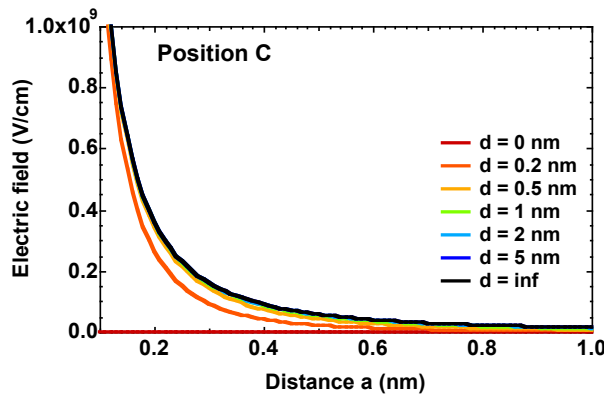


Figure 3.16 Electrostatic simulation of the field generated by an electron-hole pair for the position C, in a range of one nm for different distances  $d$ .

Assuming an initial charge separation distance ( $d$ ) of 1 nm (which is reasonable based on the size and arrangement of the pBTTT and PCBM molecules), the field at position C is significant and explains the presence of the EA signature in the TA spectra of fully intercalated samples at early time delays. In fact, the neighbouring polymer segments at position C, located at a distance ( $a$ ) of about 0.2-0.5 nm away from the hole, experience an electric field very close to the one that would be created around a free hole (i.e. the influence of the electron is small). In the absence of any other delocalization or relaxation effects, the early EA signature from charges promptly generated in the co-crystal phase should therefore have comparable amplitude due to separate charges.

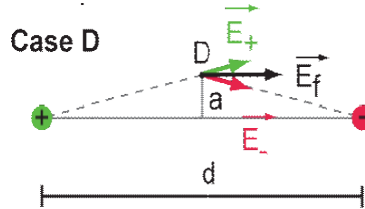


Figure 3.17. Resultant field generated by an electron-hole pair at distance  $d$  in the position  $D$ .

For position  $D$ , we are looking at the plane in the middle of the charges (so that  $a$  is no longer the distance from the positive charge, but the distance from the centre of the dipole, Figure 3.17). The fields due to the positive and negative charge cancel in the direction perpendicular to the dipole, but add up in the direction aligned with it. There is overall an increase of the total field magnitude, which is very important when the distance  $d$  between the charges is small, but drops rapidly to the value of the free charges as  $d$  is increased. The field in position  $D$  due to free charges is small, because  $D$  is far away from either charge. For a small electron-hole separation, there is a quite shallow distance dependence on  $a$ , which means that even chromophores a little further away can be affected by the field. The resultant field is described in formula 3) and the simulations are shown in Figure 3.18.

$$|\vec{E}_{tot}^D| = \frac{q}{4\pi\epsilon_0} \frac{d}{\left(\frac{d^2}{4} + a^2\right)^{3/2}} \quad 3)$$

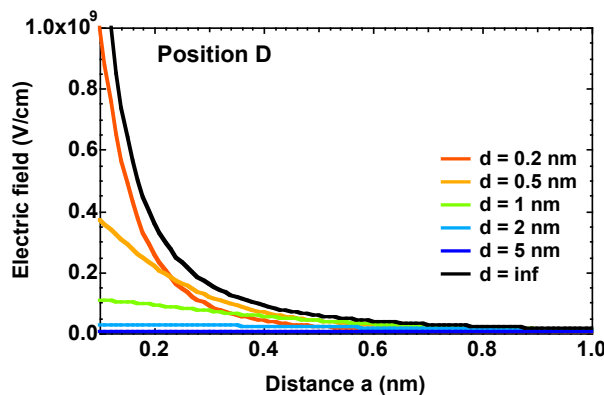


Figure 3.18 Electrostatic simulation of the field generated by an electron-hole pair for the position  $D$ , in a range of one nm, for different distances  $d$ .

In addition to the arguments concerning delocalization and polaron formation discussed above to explain the fast (100 fs and 2.4 ps) decay of the EA signal

in the TA data, the effect of spatial charge separation on chromophores in position D might also contribute. Polymer segments in position D can feel a field even if they are quite far away from the dipole, and this field decreases most steeply as the charges separate, possibly contributing to the fast decay of the EA signature.

### **3.9.2. Analysis of the TA Dynamics: Global Fit Procedure**

In this chapter, we show spectra and TA dynamics for different pBTTT blends. Dynamics corresponding to different probe wavelengths were obtained by taking cross sections through the chirp-corrected TA spectra recorded at about 350 different time delays in the -1 ps to 1 ns range. The interpretation of such dynamics is not trivial, given the complexity of polymer:fullerene blends for different reasons: in fact, multiple processes can influence the evolution of the TA signals (for example the pure charge generation dynamics might be entangled with spectral shifts due to relaxation of the neutral and charged species, and CS can be strongly multiphasic due to different distances and orientations between the donor and the acceptor). For all the above reasons, the analysis of a single-wavelength TA dynamics is typically not very meaningful. Instead, we have opted for global analysis, *i.e.* for simultaneous analysis of the TA dynamics taken every 5 nm throughout the spectrum (55). An analysis using the sum of exponential functions is meaningful when there are several independent exponential processes occurring on well-separated time scales. The multiexponential analysis perfectly suits the purpose for the level of discussion required here. It allows evaluating whether a process is multiphasic and estimating the time scale on which it occurs. Moreover, the sign of the pre-exponential factor indicates whether the process associated with the time constant leads to a rise or a decay of the TA signal at a given probe wavelength. By plotting the pre-exponential factors as a function of probe wavelength (yielding amplitude spectra), we can identify at one glimpse concerted changes in different parts of the transient spectrum. The shape of the amplitude spectra also allows disentangling different processes if they occur on a similar time scale and appears mixed into the same exponential time constant.

### 3.10. References

1. C. J. Brabec, N. S. Sariciftci, J. C. Hummelen, Plastic solar cells. *Adv Funct Mater* **11**, 15 (2001).
2. N. C. Miller *et al.*, Factors governing intercalation of fullerenes and other small molecules between the side chains of semiconducting polymers used in solar cells. *Adv. Energy Mater.* **2**, 1208 (2012).
3. P. M. Beaujuge, J. M. J. Fréchet, Molecular design and ordering effects in pi-functional materials for transistor and solar cell applications. *Journal of the American Chemical Society* **133**, 20009 (2011).
4. B. A. Collins, J. R. Tumbleston, H. Ade, Miscibility, Crystallinity, and Phase Development in P3HT/PCBM Solar Cells: Toward an Enlightened Understanding of Device Morphology and Stability. *Journal of Physical Chemistry Letters* **2**, 3135 (2011/12/15, 2011).
5. A. C. Mayer *et al.*, Bimolecular Crystals of Fullerenes in Conjugated Polymers and the Implications of Molecular Mixing for Solar Cells. *Adv Funct Mater* **19**, 1173 (Apr 23, 2009).
6. N. C. Cates *et al.*, Tuning the Properties of Polymer Bulk Heterojunction Solar Cells by Adjusting Fullerene Size to Control Intercalation. *Nano Letters* **9**, 4153 (2009).
7. J. K. Lee *et al.*, Processing Additives for Improved Efficiency from Bulk Heterojunction Solar Cells. *Journal of the American Chemical Society* **130**, 3619 (2008/03/01, 2008).
8. Y. Zhao, Z. Xie, Y. Qu, Y. Geng, L. Wang, Solvent-vapor treatment induced performance enhancement of poly(3-hexylthiophene):methanofullerene bulk-heterojunction photovoltaic cells. *Applied Physics Letters* **90**, 043504 (2007).
9. J. Peet *et al.*, Efficiency enhancement in low-bandgap polymer solar cells by processing with alkane dithiols. *Nat Mater* **6**, 497 (Jul, 2007).
10. H. Hoppe, N. S. Sariciftci, Morphology of polymer/fullerene bulk heterojunction solar cells. *Journal of Materials Chemistry* **16**, 45 (2006).
11. W. Ma, C. Yang, X. Gong, K. Lee, A. J. Heeger, Thermally Stable, Efficient Polymer Solar Cells with Nanoscale Control of the Interpenetrating Network Morphology. *Adv Funct Mater* **15**, 1617 (2005).
12. S. E. Shaheen *et al.*, 2.5% efficient organic plastic solar cells. *Applied Physics Letters* **78**, 841 (2001).
13. F. C. Jamieson *et al.*, Fullerene crystallisation as a key driver of charge separation in polymer/fullerene bulk heterojunction solar cells. *Chemical Science* **3**, 485 (2012).
14. I. Mcculloch *et al.*, Liquid-crystalline semiconducting polymers with high charge-carrier mobility. *Nat Mater* **5**, 328 (Apr, 2006).

15. M. Scarongella *et al.*, The influence of microstructure on charge separation dynamics in organic bulk heterojunction materials for solar cell applications. *J. Mater. Chem. A* **2**, 6218 (2014).
16. E. Buchaca-Domingo *et al.*, Additive-assisted supramolecular manipulation of polymer:fullerene blend phase morphologies and its influence on photophysical processes. *Materials Horizons* **1**, 270 (2014).
17. F. C. Spano, C. Silva, H- and J-Aggregate Behavior in Polymeric Semiconductors. *Annual Review of Physical Chemistry* **65**, 477 (2014).
18. L.-H. Li, O. Y. Kontsevoi, S. H. Rhim, A. J. Freeman, Structural, electronic, and linear optical properties of organic photovoltaic PBTTT-C14 crystal. *The Journal of Chemical Physics* **138**, (2013).
19. E. Cho *et al.*, Three-Dimensional Packing Structure and Electronic Properties of Biaxially Oriented Poly(2,5-bis(3-alkylthiophene-2-yl)thieno[3,2-b]thiophene) Films. *Journal of the American Chemical Society* **134**, 6177 (2012/04/11, 2012).
20. N. C. Miller *et al.*, Use of X-Ray Diffraction, Molecular Simulations, and Spectroscopy to Determine the Molecular Packing in a Polymer-Fullerene Bimolecular Crystal. *Adv. Mater.* **24**, 6071 (2012).
21. N. C. Roman Gysel, Alex Mayer, Michael Toney, and Michael McGehee, Molecular self-ordering in organic solar cell materials. *SPIE paper*, (2009).
22. N. Banerji, S. Cowan, E. Vauthey, A. J. Heeger, Ultrafast Relaxation of the Poly(3-hexylthiophene) Emission Spectrum. *Journal of Physical Chemistry C* **115**, 9726 (2011).
23. N. Banerji, S. Cowan, M. Leclerc, E. Vauthey, A. J. Heeger, Exciton formation, relaxation and decay in PCDTBT. *Journal of the American Chemical Society* **132**, 17459 (2010).
24. N. P. Wells, B. W. Boudouris, M. A. Hillmyer, D. A. Blank, Intramolecular exciton relaxation and migration dynamics in poly(3-hexylthiophene). *Journal of Physical Chemistry C* **111**, 15404 (Oct 25, 2007).
25. S. C. J. Meskers, J. Hubner, M. Oestreich, H. Bassler, Dispersive relaxation dynamics of photoexcitations in a polyfluorene film involving energy transfer: Experiment and Monte Carlo simulations. *J Phys Chem B* **105**, 9139 (Sep 27, 2001).
26. O. G. Reid, G. Rumbles, Quantitative Transient Absorption Measurements of Polaron Yield and Absorption Coefficient in Neat Conjugated Polymers. *The Journal of Physical Chemistry Letters* **4**, 2348 (2013/07/18, 2013).
27. J. Guo, H. Ohkita, H. Benten, S. Ito, Near-IR Femtosecond Transient Absorption Spectroscopy of Ultrafast Polaron and Triplet Exciton Formation in Polythiophene Films with Different Regioregularities. *Journal of the American Chemical Society* **131**, 16869 (2009/11/25, 2009).



28. F. Dou *et al.*, in *SPIE: Physical Chemistry of Interfaces and Nanomaterials XII*. (San Diego, 2013), vol. 8811, pp. 8811J-1.
29. M. J. Lee, Z. Y. Chen, R. di Pietro, M. Heeney, H. Sirringhaus, Electrooptical Spectroscopy of Uniaxially Aligned Polythiophene Films in Field-Effect Transistors. *Chem Mater* **25**, 2075 (May 28, 2013).
30. A. A. Bakulin, J. C. Hummelen, M. S. Pshenichnikov, P. H. M. van Loosdrecht, Ultrafast Hole-Transfer Dynamics in Polymer/PCBM Bulk Heterojunctions. *Adv Funct Mater* **20**, 1653 (May 25, 2010).
31. W. L. Rance *et al.*, Photoinduced Carrier Generation and Decay Dynamics in Intercalated and Non-intercalated Polymer:Fullerene Bulk Heterojunctions. *ACS Nano* **5**, 5635 (2011).
32. N. Banerji, Sub-Picosecond Delocalization in the Excited State of Conjugated Homopolymers and Donor-Acceptor Copolymers. *Journal of Materials Chemistry C* **1**, 3052 (2013).
33. L. G. Kaake *et al.*, Photoinduced Charge Generation in a Molecular Bulk Heterojunction Material. *Journal of the American Chemical Society* **134**, 19828 (2012/12/05, 2012).
34. G. Grancini *et al.*, Hot exciton dissociation in polymer solar cells. *Nat Mater* **12**, 29 (2013).
35. K. Vandewal *et al.*, Efficient charge generation by relaxed charge-transfer states at organic interfaces. *Nat Mater* **advance online publication**, (2013).
36. S. D. Dimitrov *et al.*, On the Energetic Dependence of Charge Separation in Low-Band-Gap Polymer/Fullerene Blends. *Journal of the American Chemical Society* **134**, 18189 (2012/11/07, 2012).
37. A. A. Bakulin *et al.*, The Role of Driving Energy and Delocalized States for Charge Separation in Organic Semiconductors. *Science* **335**, 1340 (Mar 16, 2012).
38. F. Etzold *et al.*, Ultrafast Exciton Dissociation Followed by Nongeminate Charge Recombination in PCDTBT:PCBM Photovoltaic Blends. *Journal of the American Chemical Society* **133**, 9469 (2011).
39. A. A. Bakulin *et al.*, Charge-Transfer State Dynamics Following Hole and Electron Transfer in Organic Photovoltaic Devices. *The Journal of Physical Chemistry Letters* **4**, 209 (2013/01/03, 2012).
40. N. Banerji *et al.*, Sensitization of fullerenes by covalent attachment of a diketopyrrolopyrrole chromophore. *Journal of Materials Chemistry* **22**, 13286 (2012).
41. I.-W. Hwang *et al.*, Bulk Heterojunction Materials Composed of Poly(2,5-bis(3-tetradecylthiophen-2-yl)thieno[3,2-b]thiophene): Ultrafast Electron Transfer and Carrier Recombination. *Journal of Physical Chemistry C* **112**, 7853 (2008).
42. A. Siemiarzuk, B. D. Wagner, W. R. Ware, Comparison of the Maximum-Entropy and Exponential Series Methods for the Recovery of Distributions of Lifetimes from Fluorescence Lifetime Data. *J Phys Chem-Us* **94**, 1661 (Feb 22, 1990).

43. D. R. Kozub *et al.*, Direct measurements of exciton diffusion length limitations on organic solar cell performance. *Chemical Communications (Cambridge, United Kingdom)* **48**, 5859 (2012).
44. G. F. Burkhard, E. T. Hoke, Z. M. Beiley, M. D. McGehee, Free Carrier Generation in Fullerene Acceptors and Its Effect on Polymer Photovoltaics. *Journal of Physical Chemistry C* **116**, 26674 (2012/12/20, 2012).
45. S. Cook *et al.*, A photophysical study of PCBM thin films. *Chemical Physics Letters* **445**, 276 (2007).
46. L. W. Barbour, M. Hegadorn, J. B. Asbury, Watching Electrons Move in Real Time: Ultrafast Infrared Spectroscopy of a Polymer Blend Photovoltaic Material. *Journal of the American Chemical Society* **129**, 15884 (2007/12/01, 2007).
47. G. Lanzani, *The Photophysics behind Photovoltaics and Photonics*. (Wiley-VCH Verlag& Co, Weinheim, 2012).
48. D. A. Vithanage *et al.*, Visualizing charge separation in bulk heterojunction organic solar cells. *Nat Commun* **4**, 2334 (2013).
49. J. Cabanillas-Gonzalez *et al.*, Photoinduced Transient Stark Spectroscopy in Organic Semiconductors: A Method for Charge Mobility Determination in the Picosecond Regime. *Physical Review Letters* **96**, 106601 (2006).
50. A. Devižis, D. Hertel, K. Meerholz, V. Gulbinas, J. E. Moser, Time-independent, high electron mobility in thin PC61BM films: Relevance to organic photovoltaics. *Organic Electronics* **15**, 3729 (2014).
51. V. Gulbinas, Y. Zaushitsyn, H. Bassler, A. Yartsev, V. Sundstrom, Dynamics of charge pair generation in ladder-type poly(paraphenylene) at different excitation photon energies. *Phys Rev B* **70**, 035215/1 (Jul, 2004).
52. S. Gélinas *et al.*, Ultrafast Long-Range Charge Separation in Organic Semiconductor Photovoltaic Diodes. *Science* **343**, 512 (January 31, 2014, 2014).
53. Y. Tamai, K. Tsuda, H. Ohkita, H. Benten, S. Ito, Charge-carrier generation in organic solar cells using crystalline donor polymers. *Phys. Chem. Chem. Phys.* **16**, 20338 (2014).
54. A. A. Y. Guilbert *et al.*, Spectroscopic Evaluation of Mixing and Crystallinity of Fullerenes in Bulk Heterojunctions. *Adv Funct Mater*, 6972 (2014).
55. I. H. M. van Stokkum, D. S. Larsen, R. van Grondelle, Global and target analysis of time-resolved spectra. *Bba-Bioenergetics* **1657**, 82 (Jul 9, 2004).



## **CHAPTER FOUR**

# **Charge Generation in Two- and Three-Phase Microstructures of pBTTT:PCBM with Partial or Predominant Phase-Separation**

This chapter has been adapted from the following paper: “**A Close Look at Charge Generation in Polymer: Fullerene Blends with Microstructure Control**” published in the “Journal of the American Chemical Society”. In this chapter we present the transient absorption (TA) results (dynamics and spectra) for different two- and three-phase microstructures of pBTTT:PCBM obtained by using fatty acid methyl ester processing additives.

## 4.1. Introduction

In Chapter 3, we described mainly a one-phase microstructure comprised of the fully intercalated co-crystal phase (1:1 blend of pBTTT:PCBM) and a two-phase microstructure comprised of the co-crystal phase and neat PCBM regions (1:4 blend of pBTTT:PCBM). In the current chapter, we describe samples manipulated during film processing with the addition of fatty acid methyl ester additives of different lengths (Me7, M12, M14). A more reliable strategy than using the film casting temperature is to control the PCBM intercalation using those asymmetrical processing additives, which direct the supramolecular assembly in the blend (1). The structures of heptanoic acid methyl ester (Me7) and dodecanoic acid methyl ester (Me12) are shown in Figure 4.1.

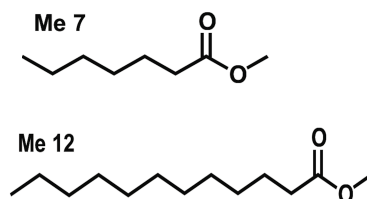


Figure 4.1 Additives of different lengths: Me7 and Me12.

It has been recently shown that the co-crystal formation can be controlled (from a fully intermixed, to a partially intercalated, to a predominantly phase-separated microstructure), by using fatty acid methyl esters as additives, which have the role to prevent intercalation between polymer chains and PCBM (1). We used these additives of different lengths and in different quantities in order to obtain controlled morphologies, different from the ones obtained changing simply the ratio of polymer to fullerene.

The first section of this chapter concerns samples having a three-phase microstructure with partial fullerene intercalation. This phase morphology is

comprised of co-crystalline regions, PCBM clusters and neat pBTTT domains, as schematically depicted in Figure 4.2. It is obtained for 1:1 pBTTT:PCBM blends processed at RT (instead of 35°C), with different amounts of Me7, or with one molar equivalent of Me 12.

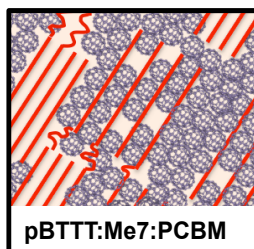


Figure 4.2 Schematic representation of a typical three-phase microstructure

The second section introduces samples having a predominantly phase-separated two-phase microstructure, comprised of neat polymer regions and neat PCBM domains. These samples are 1:1 blends of pBTTT:PCBM that have been processed using 10 molar equivalent of Me14, or Me12. The schematic representation of this microstructure is shown in Figure 4.3.

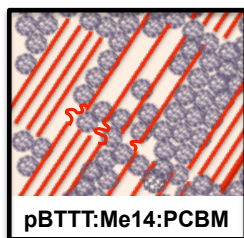


Figure 4.3 Schematic representation of a two-phase microstructure obtained using 10 molar equivalent of Me14 or Me12 additive.

We focus here on two main questions. First, we investigate how CS by both electron and hole transfer (ET and HT) depends on microstructure, and show how its rate can be limited by exciton diffusion through neat domains (2-4). Second, the role played by BHJ structure in the generation of free (as opposed to bound) charges is discussed, using the early evolution of an electro-absorption (EA) signature in the transient absorption data.

## 4.2. Experimental Methods

### 4.2.1. Sample preparation details

In order to prepare the second set of samples, we used the heptanoic acid methyl ester (Me7), dodecanoic acid methyl ester (Me12) and tetradecanoic acid methyl ester (Me14) processing additives purchased from Aldrich and Fluka. Solutions were prepared weighing a 1:1 (by mass) mixture of pBTTT and PCBM, and then adding 1, 10 or 50 molar equivalents of the respective additive per monomer unit of the polymer. Solutions of pBTTT:additive:PCBM blends were prepared in 1,2-ortho-dichlorobenzene (1,2-oDCB, Aldrich). All solutions were left stirring for more than 4 hours at 100 °C to fully dissolve the active material. Films were then deposited on glass by wire-bar coating from hot solutions (~85-90°C) onto substrates kept at RT. The 1:1 (RT) sample was prepared weighing a 1:1 (by mass) mixture of pBTTT and PCBM without any additive and the substrate was kept at RT during film casting. Prior to all measurements, oxygen was removed by keeping the samples for 24 hours in vacuum. They were then sealed in an inert measuring chamber (containing Argon) for transient absorption measurements. The film thickness was approximately 100-110 nm with a maximum absorption (optical density) in the visible range of about 0.5, as measured with a PerkinElmer Lambda 950 spectrophotometer.

### 4.2.2. TA spectroscopy: experimental conditions

See Chapter 3.2.2

## 4.3. Steady-State Absorption Spectra of the Studied Samples

All the samples presented in this chapter are summarized in Table 1:

Microstructure	Samples	Name
Partially intercalated, comprised of co-crystalline regions, PCBM clusters and neat pBTTT domains (three phases)	1:1 (RT) pBTTT:PCBM 1:50:1 pBTTT:Me7:PCBM 1:10:1 pBTTT:Me7:PCBM 1:1:1 pBTTT:Me7:PCBM 1:1:1 pBTTT:Me12:PCBM	1:1 (RT) Me7(1:50:1) Me7 Me7 (1:1:1) Me12 (1:1:1)
Predominantly phase-separated: PCBM clusters and neat pBTTT domains (two phases)	1:10:1 pBTTT:Me12:PCBM 1:10:1 pBTTT:Me14:PCBM	Me12 Me14

Table 1 Summary of the investigated microstructures for pBTTT:PCBM. The different processing conditions yielding each microstructure are also given, together with the abbreviated sample names used in the main text.

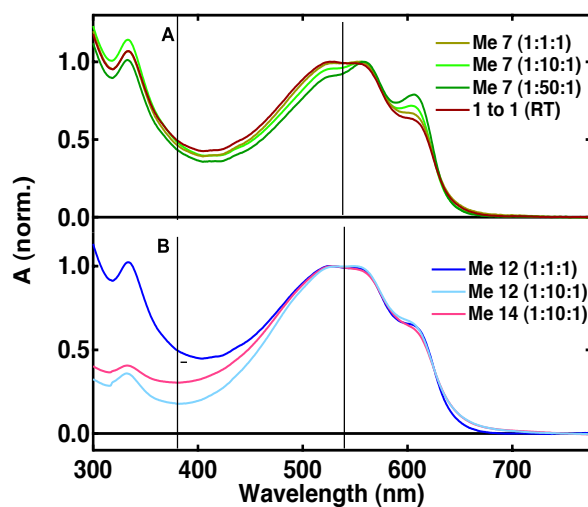


Figure 4.4 Steady-state absorption spectra of the investigated samples. (A) 1:1 blends of pBTTT:PCBM with different amounts of processing additive Me7, and without additive processed at RT. (B) 1:1 blends of pBTTT:PCBM with different amounts of Me 12 or Me 14. Vertical lines are the excitation wavelengths for TA spectroscopy.

The steady-state absorption spectrum of the 1:1 blend processed at room temperature (RT) is shown in Figure 4.4A. It shows significant differences compared to the fully intercalated 1:1 sample processed at 35°C (see Chapter 3). The polymer now exhibits a broad band around 540 nm and a shoulder at 605 nm, indicating incomplete fullerene intercalation (co-existence of neat pBTTT and co-crystal regions). The broad signature at 540 nm is due to neat pBTTT regions (by comparison to the absorption spectrum of neat pBTTT films), while the shoulder is representative for the more structured spectrum of the intercalated phase. The absorption spectra of the 1:1 pBTTT:PCBM blends (by weight) processed with 1, 10 and 50 molar equivalents of Me 7 per pBTTT monomer unit are depicted in Figure 4.4A. For the three samples, the superposed absorption of the broad and structured pBTTT bands points also to partial fullerene intercalation. From the relative weight of the broad 540 nm signature versus the 605 nm shoulder, it appears that the PCBM intercalation is slightly more pronounced for the highest Me 7 concentration. In a previous study, a variety of tools (grazing-angle incidence wide-angle X-ray scattering, scanning transmission X-ray microscopy, optical microscopy, resonant soft X-ray scattering) confirmed the three-phase microstructure in the 1:10:1 pBTTT:Me7:PCBM blend (1).



The previous structural investigation also revealed that using additives with longer alkyl chains, such as Me 12 or Me 14, leads to enhanced expulsion of PCBM from the co-crystal regions, and thus to formation of a predominantly phase-separated microstructure.<sup>(1)</sup> The absorption spectra of the 1:1 pBTTT:PCBM blends processed with Me 12 and Me 14 show a pronounced structureless signature in the 540 nm region and only a weak shoulder at 605 nm, confirming the predominant presence of neat polymer domains (Figure 4.4B). Moreover, there is a surprising decrease of the PCBM band below 400 nm for the samples containing 10 molar equivalents of Me 12 or Me 14, although the amount of fullerene has not been reduced (and the PCBM band re-appeared when the samples were re-dissolved). A similar effect has been noted for annealed poly(3-hexylthiophene) (P3HT) blends with PCBM.<sup>(5)</sup> We are still investigating the precise origin of the effect, but it is likely to be related to the formation of long-range PCBM crystallites (as opposed to short-range aggregates) (6). With less Me 12 (1:1:1 blend in Figure 4.4B), the shape of the pBTTT band is hardly affected, but interestingly the amplitude of the PCBM signature is not reduced, suggesting limited PCBM crystallization as with Me 7.

## **4.4. Charge Generation Studied by TA Spectroscopy**

### **4.4.1. Partially intercalated blends**

A three-phase microstructure can be obtained not only by using additives, but also by processing the 1:1 blends at room temperature (RT). For the 1:1 blend processed at RT, which we will refer to as 1:1 (RT), the TA spectra with 540 nm excitation (Figure 4.5B) are clearly different from the fully intercalated 1:1 sample (Figure 4.5A, Chapter 3). In particular, the shape of the GSB reflects the changes in the steady state absorption spectra, while the amplitude of the long-lived TA features is significantly enhanced in the RT sample, pointing to a microstructure that favours generation of free charges (although still more charges recombine than in the 1:4 blend).

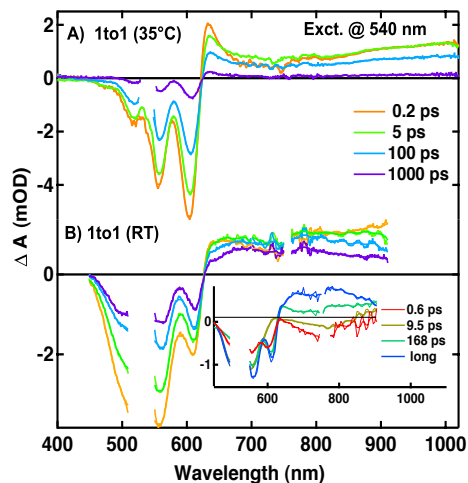


Figure 4.5 TA data for 1:1 pBTTT:PCBM films (by weight) following excitation at 540 nm (A) TA spectra at selected time delays for the fully intercalated 1:1 blend processed at 35 °C. (B) TA spectra of the partially intercalated 1:1 blend processed at room temperature (RT). The inset shows the amplitude spectra associated with the time constants obtained by multi-exponential global analysis of the data.

In agreement with the similarity of the steady-state absorption, the TA behaviour of the 1:1 (RT) sample (Figure 4.5B) is comparable to the one of the 1:1 blend processed with Me 7, which also results in partial fullerene intercalation (shown for 10 molar equivalents and 540 nm excitation in Figure 4.6A). For convenience, we will simply call the latter the Me 7 sample. As with the 1:1 (RT) sample, processing of the 1:1 blend with Me 7 reduces the extent of geminate charge recombination (gCR, see charge dynamics at 850 nm in Figure 4.7C). The partial phase separation of the polymer and fullerene due to the addition of Me 7 has also previously been correlated to enhanced free charge yield (by nanosecond TA spectroscopy and time-resolved microwave conductivity) and to improved solar cell efficiency compared to fully intercalated systems (1).

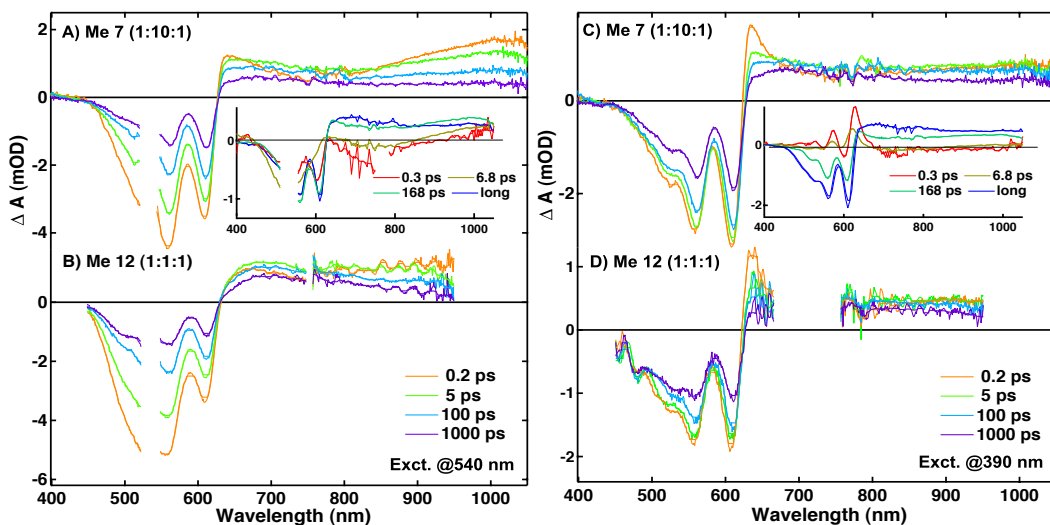


Figure 4.6 TA spectra at selected time delays for 1:1 pBTTT:PCBM films processed with ten molar equivalents of Me 7, or with one molar equivalent of Me 12, following excitation at 540 nm (A-B), or at 390 nm (C-D). The insets represent the amplitude spectra associated with the time constants obtained by multi-exponential global analysis of the data. Thicker solid lines are smoothed and overlaid to the raw experimental and amplitude spectra.

For both partially intercalated samples (RT and Me 7), the GSB contains an unstructured contribution in the 530 nm region, which we attribute to the presence of neat pBTTT domains (Figure 4.5B and Figure 4.6A). Since neat pBTTT domains and co-crystalline regions are excited at 540 nm, we expect prompt CS in the highly intermixed regions as well as multiphasic delayed CS for excitons diffusing (by various distances) through the neat regions towards PCBM (2, 3, 7). Indeed, the characteristic ESA signature at 1000 nm in the early TA spectra (in addition to the flat absorption of promptly generated charges), confirms the delayed presence of pBTTT excitons in the neat domains. Their quenching leads to fast components in the TA dynamics, for example in the ESA at 1000 nm (Figure 4.7E). In contrast, only slow decay of overlapping charge absorption is seen for the intercalated 1:1 blend processed at 35°C.

By global analysis, we found a sub-picosecond time constant (0.6/0.3 ps for RT/Me 7) and a slower (9.5/6.8 ps) time constant for the delayed exciton quenching. This assignment is based on the decay of the negative SE around 730 nm and positive ESA above 870 nm in the corresponding amplitude spectra (insets of Figure 4.5B and Figure 4.6A). We cannot exclude some slower exciton quenching masked by the evolution of the charge absorption. The amplitude spectra assigned to exciton quenching also indicate decrease

of the GSB. Reduction of the GSB during CS has been reported in other polymer:fullerene blends (3).

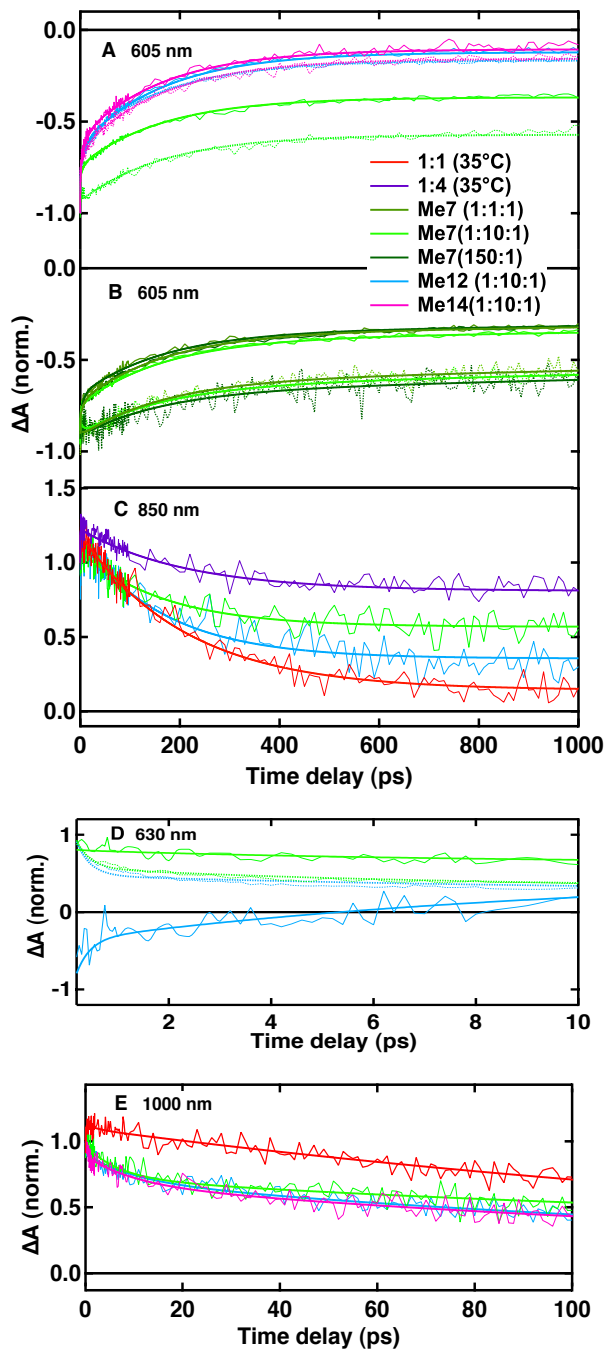


Figure 4.7 TA dynamics recorded for various blends shown in the legend at probe wavelengths of 605 nm (A, B), 850 nm (C), 630 nm (D), and 1000 nm (E). Solid lines represent 540 nm excitation, while dotted lines represent 390 nm excitation. The thicker lines are the best multi-exponential fits from global analysis.

However, given the  $\sim 4$  ps exciton decay in neat pBTTT films (see Chapter 3, Figure 4.5), it is possible that excitons in the neat regions are not only dissociated by delayed CS, but are also partly lost to the ground state. Finally, we observe a slower decrease of the TA features with a 168 ps time constant for the 1:1 (RT) and Me7 samples, which we attribute to gCR in the co-crystalline regions, given the similarity of the amplitude spectrum with the one obtained for gCR in the 1:1 and 1:4 blends (see Chapter 3) (8).

Let us now turn to the TA data with 390 nm excitation, where both the polymer and the PCBM are excited. TA spectra for the partially intercalated Me 7 sample are shown in Figure 4.6C. In those blends, the PCBM is present both in the intercalated, co-crystalline phase, as well as in the relatively phase-pure fullerene clusters. A complex overlap of prompt and delayed electron and hole transfer processes with recombination is therefore expected. There are significant differences compared to the data obtained with 540 nm excitation. Most notably, there is an apparently reduced decay of the TA features for the 390 nm data. This is also obvious in the TA dynamics probed at 605 nm for the Me 7 sample (Figure 4.7A, green solid lines for 540 nm and dotted lines for 390 nm excitation). Since free charge yield in OPV blends is generally not increased with excess excitation energy, it is unlikely that gCR is reduced at 390 nm. A more likely interpretation is that delayed HT from PCBM clusters (as observed in the 1:4 blend) leads to a rise of the polymer GSB and charge absorption, which partly counterbalances the decrease of the TA features due to gCR.

Finally, the 1:1 blend processed with a small quantity of Me 12 (1:1:1 Me 12 blend) has a three-phase microstructure with significant PCBM absorption at 390 nm, similar to the Me 7 blends. The evolution of the TA spectra resembles the one of the 1:1 (RT) and Me 7 samples (Figure 4.6B, D).

#### **4.4.2. Predominantly phase-separated samples**

More phase separated systems can be obtained when the 1:1 pBTTT:PCBM blends are processed with 10 molar equivalents of Me 12 and Me 14, leading to relatively phase-pure domains of the polymer and fullerene as shown in Figure 4.3(1). The TA spectra of those samples (abbreviated as Me 12 and Me 14 in the following) are shown in Figure 4.8A, B, for 540 nm excitation and Figure 4.8C, D for 390 nm excitation.

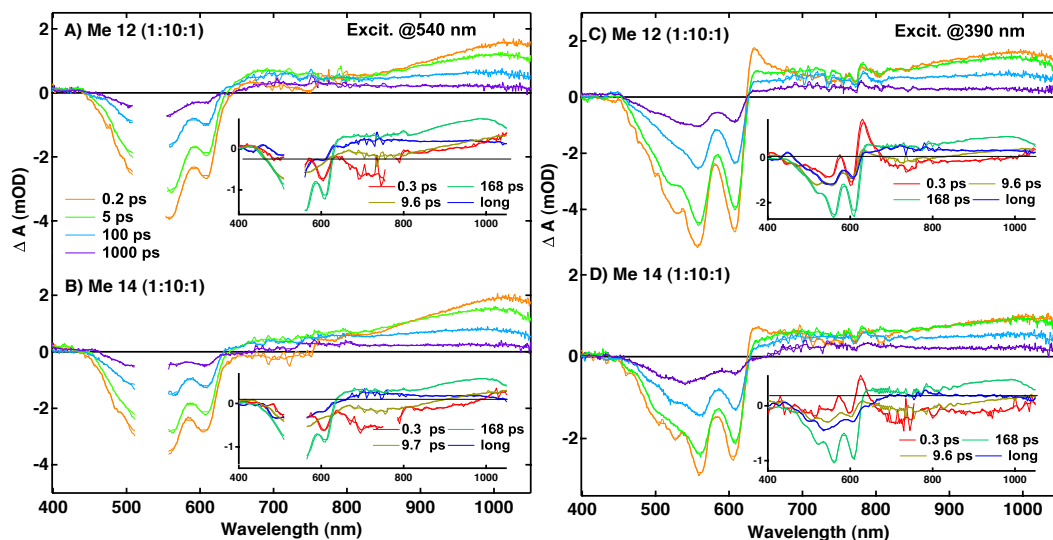


Figure 4.8 TA spectra at selected time delays for 1:1 pBTTT:PCBM films processed with 10 molar equivalent of Me 12 or Me14, following excitation at 540 nm (A-B), or at 390 nm (C-D). The insets represent the amplitude spectra associated with the time constants obtained by multi-exponential global analysis of the data. Thicker solid lines are smoothed and overlaid to the raw experimental and amplitude spectra.

The free charge yield and solar cell efficiency for the Me 12 and Me 14 blends is less than for the three-phase microstructure of the Me 7 sample, but higher than in the fully intercalated 1:1 blend (1). This trend is clearly reflected by the TA dynamics probed at 850 nm (mainly charge absorption, Figure 4.7C). The most long-lived signal is observed for the most efficient 1:4 blend, followed by samples processed with Me7, then Me12, and finally the fully intercalated 1:1 (35°C) blend. Thus, it is clear that recombination processes on the sub-nanosecond time scale determine the performance of pBTTT:PCBM devices.

There is no significant difference in the TA data between the blends processed with Me 12 and Me 14 (blue and pink curves in Figure 4.7A). With 540 nm excitation of pBTTT, the early 0.2 ps TA spectrum is dominated by signatures of pBTTT excitons (negative SE at 730 nm and positive ESA at 1000 nm, Figure 4.8A,B), without significant contribution of charge absorption. This strong reduction of prompt CS, as well as the more unstructured shape of the GSB, confirm the predominance of neat pBTTT domains rather than highly intermixed, co-crystalline regions. According to the fluorescence dynamics for 700 nm and 800 nm emission, the excitons in Me 14 blends are quenched more rapidly than in neat pBTTT films (see Chapter 3, Figure 4.13). Still, the quenching is quite slow and strongly

multiphasic, with time constants of 290 fs, 3.4 ps, 25 ps and 165 ps, confirming that exciton diffusion limits the CS rate.

In the TA spectra, the exciton quenching contributes to the 0.3 ps and 9.7 ps amplitude spectra (insets of Figure 4.8 A, B; their shape is similar to the one obtained for the Me 7 sample). There is also a dominant contribution of exciton decay to the 168 ps component (see similarity with the 176 ps amplitude spectrum of neat pBTTT film, see Chapter 3, Figure 4.5B). For the fully intercalated (1:1 and 1:4) and partially intercalated (RT, Me 7) blends, the TA decay on this time scale is mainly caused by gCR of charge pairs in the co-crystal phase. For the more phase-separated Me 12 and Me 14 samples, the loss mechanism is different and results mainly from the decay of excitons in neat pBTTT domains to the ground state, which cannot reach a PCBM acceptor during their lifetime.

For the Me 12 and Me 14 samples, it is still mainly the pBTTT which absorbs with excitation at 390 nm, since there is very little absorption of PCBM in this region (fullerene light harvesting is lost due to long-range ordering of PCBM, Figure 4.4B). This explains the negligible difference in the dynamics with 540 nm and 390 nm excitation (solid and dotted lines in Figure 4.7A). The TA spectra with 390 nm excitation also exhibit a strong contribution of polymer excitons, undergoing slow multiphasic quenching and decay (Figure 4.8C, D).

#### **4.5. Evolution of the Electro-Absorption at 630 nm**

As described in the previous paragraphs, for the partially intercalated 1:1 (RT) and Me 7 blends excited at 540 nm, gCR is reduced compared to the fully intercalated 1:1 blend, which we attribute to the presence of phase-pure domains in the former blends, similar to the 1:4 system. However, neat pBTTT regions are now present in addition to the PCBM clusters (1). The TA spectra recorded at long time delays (1 ns) predominately represent the signature of long-lived free charges (Figure 4.5B and Figure 4.6 A). The GSB and flat absorption of positively charged pBTTT are obvious, but there is a striking absence of the EA signal peaking at 630 nm. The 630 nm signature is weakly present in the 0.2 ps spectra of the RT and Me 7 blends excited at 540 nm. It is enhanced with 390 nm excitation (Figure 4.6C). For both excitation wavelength, the EA nevertheless almost completely disappears within a few picoseconds. In the predominantly phase-separated samples processed with

Me12 or Me14, the EA absorption signature can only be seen for short time delays and with 390 nm excitation (Figure 4.6D and Figure 4.7C, D).

Since we have seen for the 1:4 blend that the 630 nm peak amplitude is quite insensitive to the migration of electrons to PCBM clusters, we deduce that the fast decay of the 630 nm peak in the partially intercalated samples is related to the hole migration from the co-crystal phase to the neat pBTTT domains. Following a similar reasoning based on electrostatic simulations as for the 1:4 blend, we show that the increasing electron-hole separation by itself should not have a strong effect on the field experienced by the close neighbours of the hole (see section 3.9.1). The strong reduction of the EA in the partially intercalated samples is therefore rather related to the **nature** of the polymer segments surrounding the hole.

Indeed, the electronic properties of pBTTT are very different when it is in the neat domains or co-crystal phase, as testified by the change in the absorption spectrum (Chapter3, Figure3). The less steep absorption edge in the broad spectrum of neat pBTTT leads to a smaller value of the first derivative and thus to weaker EA. Experimentally, the EA spectrum recorded for a device containing neat pBTTT (with externally applied field) confirms that it is less sharp and reduced compared to the intercalated 1:1 blend (Chapter3, Figure 4.10A). Thus, the electric field generated by a hole in neat pBTTT domains will induce a weak EA in neighbouring polymer segments, not visible in the TA spectra.

Further evidence that the prominent EA signature is specifically related to holes in co-crystalline regions is shown in Figure 4.9A-C (540 nm excitation). Here, the concentration of Me 7 was varied during processing of the 1:1 blend, allowing slight tuning of the extent of PCBM intercalation. The early oscillatory EA signature due to prompt CS is more pronounced in the 1:50:1 blend containing more co-crystal fraction, than in the less intercalated 1:1:1 blend (in addition to weak changes in the GSB shape according to the steady-state absorption). Apart from this initial difference, the TA dynamics and overall evolution of the TA spectra is similar for the three samples (Figure 4.7B).



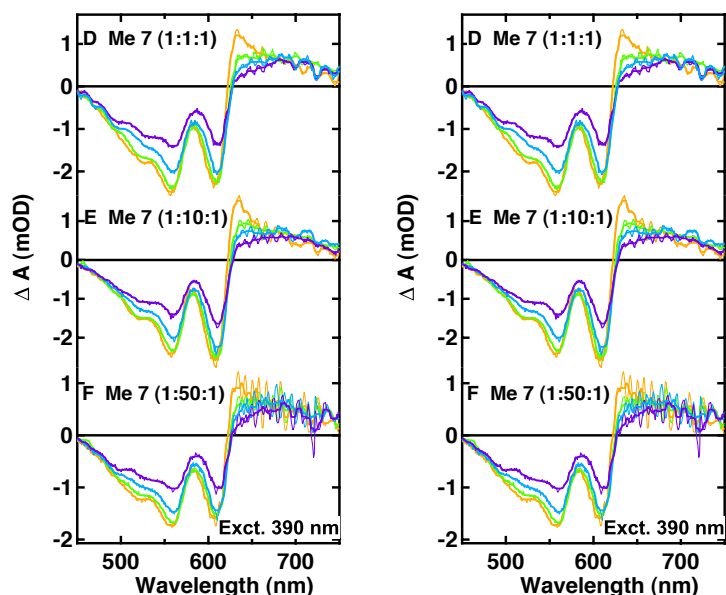


Figure 4.9 TA spectra at selected time delays for 1:1 pBTTT:PCBM films processed with different amounts of Me 7 additive, following excitation at 540 nm (A-C), or at 390 nm (D-F). Thicker solid lines are smoothed and overlaid to the raw experimental data and raw amplitude spectra.

With the phase-dependent 630 nm signature in pBTTT, we have a unique tool in hand to directly monitor the generation site of charges and the migration of holes from co-crystalline to neat polymer regions. Important conclusions can be drawn for the partially intercalated and more phase-separated pBTTT:PCBM blends:

1) The presence of the 630 nm EA peak at ultrafast times designates co-crystal regions as the prompt charge generation site in the blends containing a significant intermixed fraction (1:1 blends processed at RT and with 10 or 50 molar equivalents of Me 7, excited at 540 nm).

2) Prompt CS can also occur for excitons formed at the domain boundaries of neat phases (no diffusion is necessary and the hole is immediately present in the neat domain), leading to an initial charge signature without a visible EA signal (less intercalated Me 7 (1:1:1) and Me 12 (1:1:1) samples, excited at 540 nm). Since there is in general no obvious rise of the EA during delayed CS in the partially intercalated samples as well as in the more phase-separated Me 12 and Me 14 samples, this process also seems to occur at the interfaces between phase-pure domains.

3) Upon 390 nm excitation of all the partially intercalated samples (1:1 RT, Me 7) as well as the more phase separated Me 12 and Me 14 systems, there is a strong enhancement of the oscillatory 630 nm signature in the early 0.2 ps spectra. This suggests a selective excitation of PCBM and possibly pBTTT in the co-crystal phase at 390 nm. The effect is independent of the Me 7 concentration used during processing, confirming that promptly generated holes are in all cases pre-dominantly found in the highly intermixed, intercalated regions (Figure 4.9D-F).

4) Whenever charges are promptly generated in the co-crystal phase for the partially intercalated systems (with 540 and 390 nm excitation) and for the predominantly phase-separated blends (with 390 nm excitation), the holes migrate to neat pBTTT regions on the  $\sim 1$  ps time scale, as evidenced by the fast decay of the EA signature. For 390 nm excitation, this is clearly seen in the dynamics of Figure 4.7D. The EA decay is also reproduced by the oscillatory shape of the 0.3 ps amplitude spectra (insets of Figure 4.8C, D). The EA decay is less obvious in the amplitude spectra with 540 nm excitation, because of less selective excitation of the co-crystal phase and mixing with the ET dynamics.

5) The results confirm that neat polymer domains in partially intercalated samples favour spatial separation of charge pairs generated in the intermixed co-crystal phase, contributing to reduced gCR, in the same way as PCBM clusters in the 1:4 blend. They can however lead to loss of short-lived pBTTT excitons.

6) From the  $\sim 1$  ps decay of the EA, we conclude that the holes can move immediately after their generation and do so very quickly. In agreement with recent Monte Carlo simulations,<sup>(9)</sup> we suggest that this fast transport is sustained by high local mobility and by an energy cascade driving the holes to the neat regions. An energy cascade of 100-200 meV has been reported for the electron transport to the fullerene clusters (1), and can also be expected between the intermixed and neat pBTTT regions. Within the co-crystal phase, a hole can in principle migrate along the polymer backbones or along the  $\pi$ -stacking direction, but the former seems to be favoured (10). We therefore hypothesise that the ultrafast hole migration occurs predominantly along the same polymer chains, which extend from the co-crystalline to neat pBTTT domains (so-called 'tie'molecules')(11).

7) For the Me 7 and 1:1 (RT) samples (three phase microstructure), the presence of the 630 nm EA signature in the 168 ps amplitude spectrum assigned to gCR suggests that this recombination is dominant for holes remaining in the intermixed co-crystal regions (insets of Figure 4.5B and Figure 4.6A, C). The charges are likely to be trapped in the intermixed phase due to poor (through-chain) connectivity to neat pBTTT regions and missing percolated paths to PCBM clusters (11, 12).

## 4.6. Conclusion

In this chapter we have analysed two more phase-morphologies obtained for the pBTTT:PCBM blends: partially intercalated and predominantly phase-separated microstructures. Control of the charge separation was achieved by targeting well-defined microstructures through the use of fatty acid methyl esters processing additives. The electro-absorption (Stark effect) signature allowed to directly visualize ultrafast transport of holes from intercalated to neat region:

**Three-phase microstructure** with co-crystalline regions, PCBM clusters and neat pBTTT domains (1:1 pBTTT:PCBM blend processed at room temperature, with different amounts of Me 7, or with 1 molar equivalent of Me 12): prompt charge separation occurs in the co-crystal phase and for excitons formed at the edge of neat domains, while exciton diffusion through PCBM or pBTTT regions limits the rate of charge separation (and leads to some loss of short-lived polymer excitons). Nevertheless, both neat PCBM and polymer domains contribute to the spatial separation of electron-hole pairs, reducing geminate recombination in intercalated regions. The holes promptly generated in the co-crystal phase migrate to neat pBTTT regions on the  $< 1$  ps time scale, showing that they are free to move immediately after their formation. This ultrafast hole transport is sustained by high local mobility (possibly along polymer chains extending from co-crystal to neat regions) and by an energy cascade driving the holes to the neat domains.

**Predominantly two-phase system** comprised of relatively phase-separated regions of neat PCBM and pBTTT (1:1 pBTTT:PCBM blend processed with 10 molar equivalents of Me12 or Me14): charge separation becomes slow and multiphasic due to exciton diffusion, and there is significant loss to the ground state of excitons that cannot reach a charge separation site during their lifetime. Moreover, long-range fullerene ordering limits light harvesting

by PCBM at 390 nm, but remaining co-crystals can be selectively excited at this wavelength, followed by ultrafast transport of promptly generated holes to neat pBTTT regions.

Overall, the pBTTT:PCBM system has proven to be particularly suitable to answer many long-standing questions related to charge generation in polymer:fullerene blends. Not only because its microstructure can be precisely characterized and carefully manipulated, but also because the optoelectronic differences of the polymer found in neat or intercalated regions allow to differentiate the electro-absorption according to the bulk heterojunction phase, giving us a unique tool to determine the location of the charges.

## 4.7. References

1. E. Buchaca-Domingo *et al.*, Additive-assisted supramolecular manipulation of polymer:fullerene blend phase morphologies and its influence on photophysical processes. *Materials Horizons* **1**, 270 (2014).
2. A. A. Paraecattil, N. Banerji, Charge Separation Pathways in a Highly Efficient Polymer: Fullerene Solar Cell Material. *Journal of the American Chemical Society* **136**, 1472 (2014/01/29, 2014).
3. I. A. Howard, R. Mauer, M. Meister, F. Laquai, Effect of Morphology on Ultrafast Free Carrier Generation in Polythiophene:Fullerene Organic Solar Cells. *Journal of the American Chemical Society* **132**, 14866 (Oct 27, 2010).
4. S. De *et al.*, Exciton dynamics in alternating polyfluorene/fullerene blends. *Chem Phys Lett* **350**, 14 (2008).
5. M. A. Faist *et al.*, Effect of multiple adduct fullerenes on charge generation and transport in photovoltaic blends with poly(3-hexylthiophene-2,5-diyl). *Journal of Polymer Science, Part B: Polymer Physics* **49**, 45 (2011).
6. A. A. Y. Guilbert *et al.*, Spectroscopic Evaluation of Mixing and Crystallinity of Fullerenes in Bulk Heterojunctions. *Advanced Functional Materials*, n/a (2014).
7. S. De *et al.*, Exciton dynamics in alternating polyfluorene/fullerene blends. *Chem Phys Lett* **350**, 14 (2008).
8. M. Scarongella *et al.*, The influence of microstructure on charge separation dynamics in organic bulk heterojunction materials for solar cell applications. *Journal of Materials Chemistry A* **2**, 6218 (2014).
9. T. M. Burke, M. D. McGehee, How High Local Charge Carrier Mobility and an Energy Cascade in a Three-Phase Bulk Heterojunction Enable >90% Quantum Efficiency. *Advanced Materials* **26**, 1923 (2014).
10. M. J. Lee *et al.*, Anisotropy of Charge Transport in a Uniaxially Aligned and Chain-Extended, High-Mobility, Conjugated Polymer Semiconductor. *Advanced Functional Materials* **21**, 932 (2011).
11. R. Noriega *et al.*, A general relationship between disorder, aggregation and charge transport in conjugated polymers. *Nat. Mater.* **12**, 1038 (2013).
12. J. A. Bartelt *et al.*, The importance of fullerene percolation in the mixed regions of polymer-fullerene bulk heterojunction solar cells. *Adv. Energy Mater.* **3**, 364 (2013).

## **CHAPTER FIVE**

# **Charge Generation in PBDTTPD:PCBM Blends: A Comparison between TA and THz Time-Domain Spectroscopy**

The first part of this chapter (TA results) has been adapted from the following paper: **"The influence of microstructure on charge separation dynamics in organic bulk heterojunction materials for solar cell applications"**, published in the *Journal of Materials Chemistry A*. We compare the dynamics and the process of charge generation in blended and neat PBDTTPD films using THz time domain and transient absorption spectroscopy.

## 5.1 Introduction

In order to better understand the relation between the process of charge generation at the organic polymer:fullerene interface and the specific microstructure of the blend, we investigate in this chapter another type of polymer: a donor-acceptor co-polymer, PBDTTPD. In contrast to the rather crystalline pBTTT polymer (which has long-range ordering) presented in Chapters 3 and 4, the polymer presented in this chapter has different structural properties: there is only short-range ordering in neat PBDTTPD films and in PBDTTPD:PCBM blends, i.e. the microstructure is amorphous.

The PCE of this polymer:fullerene blend is one of the highest amongst the polymers used for photovoltaic application (it goes up to 8.5 %) (1). A lot of work has been recently done on PBDTTPD, showing the importance in understanding the process of charge generation to improve the efficiency of solar cells. Control of morphology, charge-trapping, PCBM percolation, and the effect of excess excitation energy, have been among the most studied issues, using photoluminescence and absorption techniques (2, 3) This chapter specifically addresses the understanding of the characteristic photo-physics behind the charge separation (CS) for an amorphous polymer. In order to obtain complementary information about this process, we used transient absorption spectroscopy and THz time domain spectroscopy.

In fact, TA spectroscopy is not able to give a full characterization of the processes happening in the BHJ, as this technique suffers from overlapping signatures of different kind of species: free charges, excitons and also bound charge pairs (charge transfer states)(4). The dynamics of bound and free charge generation are difficult to be clearly disentangled in the TA spectra. On the other hand, THz time domain spectroscopy is more sensitive to detect directly the contribution of free charges with femtosecond time resolution. Another strength of the THz technique is to have access not only to the amplitude but also to the phase shift of the THz field as it passes through the

photo-excited sample, so that is possible to extract the complex conductivity and from this to obtain the real and the imaginary parts. This permits to distinguish between the presence of bound charges (in the exciton or charge transfer state) and free charges (polaron state) (5, 6). Moreover, THz time domain spectroscopy allows also to detect the intrinsic mobility of generated charges, which is conceptually related to the local mobility of charges: this value of mobility is different from the one obtained applying an external electric field, which gives a long range mobility between the two electrodes (7).

Nevertheless, THz time domain spectroscopy has been a less used technique to study the process of charge generation in conjugated polymer blends, because measurements are technically difficult and yield very weak signals. It has been used to find the mobility of charges (electrons and holes) in P3HT, P3HT:PCBM and PTB7:PCBM (8),(9),(10, 11). Moreover, the charge transport dynamics when changing the molecular weight in APFO-3:PCBM blends (12), the interchain interactions in polymer films and solutions (related to the polarizability) (13), and the dynamics of photo generation in MEH-PPV were also investigated (14). However, most of these measurements have been done using very high excitation fluencies, where phenomena of bimolecular recombination are enhanced and mask the real dynamics of the process of charge generation.

In this chapter, we examine charge generation in neat PBDTTPD films and blends with PCBM, upon excitation at different wavelengths, using TA and THz time domain spectroscopy. We investigate the dynamics in the femtosecond to nanosecond regime, varying the fluence around  $30 \mu\text{J}/\text{cm}^2$ , in order to get rid of the bimolecular recombination and annihilation phenomena. For the THz work, we examine also the photoconductivity spectra at 0.5 ps and 800 ps in the range between 0.2-2 THz (0.8-8 meV). The probe in this wavelength range is at too low energy to be able to promote any electronic transitions and it is below any excitation binding energy or exciton resonances. However, it is sensitive to the dielectric polarization of excitons. This characteristic gives the possibility to better understand the concept of 'polaron' in organic materials, which has a quite different peculiarity with respect to the classical concept of a 'free charge' in an inorganic material.



## 5.2 Experimental Methods

### 5.2.1 Sample preparation details

PBDTTPD was synthesised according to previously published procedures (15, 16). Its chemical structure is shown in Figure 5.1. The PBDTTPD polymer bears alkyl side-chains on both the TBD (thienopyrroledione) and BDT (benzodithieophene) units, which are necessary for solubility. Side-chains of different lengths can be attached on the TPD unit, strongly affecting solar cell efficiency. In this chapter, we use the polymer with the longest side-chain, designated as P3 ( $M_n = 14.7$  kDa, PDI = 2.15).

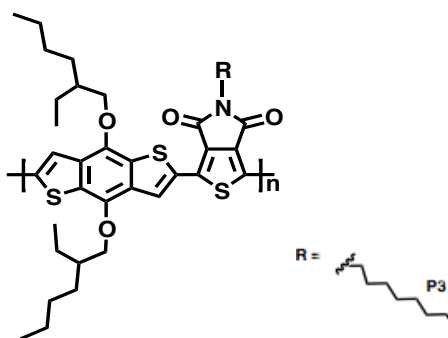


Figure 5.1 Chemical structure of PBDTTPD. P3 is the side-chain placed at the R position.

The PBDTTPD:PCBM mixture (1:2 weight ratio) was dissolved in anhydrous 1,2-*ortho*-dichlorobenzene (*o*DCB) at a 10 mg/mL polymer concentration inside a glovebox. It was stirred for 48 hours at 100-120°C. The hot solutions were spin-coated at 1000 rpm for 2 minutes onto glass substrates that had previously been sonicated in water/acetone/isopropanol and plasma cleaned. The film thickness was around 100 nm, with a maximum visible absorbance about 0.3-0.4. Measurements were carried out in an inert sample chamber. Although microstructural degradation has been reported for PBDTTPD:PCBM (in particular for the high molecular weight samples)(17), we did not notice any effect on the TA measurement recorded immediately, one week and several weeks after film preparation, indicating that any degradation insignificantly influenced the investigated properties. For the THz measurements, the samples were prepared from the same solutions, this time drop casting them on quartz substrates to obtain film thickness of over 500 nm.

## 5.2.2 TA and THz spectroscopy

The TA spectra were recorded using femtosecond pulsed laser pump-probe spectroscopy, as described in the previous chapters. This was done in collaboration with Master student Arun Paraecattil. Excitation at 540 nm was used to excite the PBDTTPD polymer. The pump beam was generated with a commercial two-stage non-collinear optical parametric amplifier (NOPA-Clark, MXR) from the 778 nm output of a Ti:sapphire laser system with a regenerative amplifier providing femtosecond pulses at a repetition rate of 1 kHz. Alternatively, the samples were excited at 390 nm (where there is significant PCBM absorption), after frequency doubling the fundamental 778 nm beam in a BIBO crystal (about 150 fs pulse duration). The pulse energy at the sample was adjusted within the tens of nano-joule range in order to have identical dynamics at slightly higher and lower power, assuring complete absence of any intensity-induced bimolecular effects. For the PBDTTPD blends, a fluence of 2-4  $\mu\text{J}/\text{cm}^2$  ( $2\text{-}6 \times 10^{12}$  photons/ $\text{cm}^2$ ) was necessary. For the comparison of the two excitation wavelengths using the PBDTTPD:PCBM sample, particular care was taken to keep the photon flux constant at  $5.9 \times 10^{12}$  photons/ $\text{cm}^2$ .

In the THz experiments, the photon flux of the pump was changed from a minimum of  $9 \times 10^{13}$  photons/ $\text{cm}^2$  ( $30 \mu\text{J}/\text{cm}^2$ ) to a maximum of  $4.4 \times 10^{15}$  photons/ $\text{cm}^2$  ( $2260 \mu\text{J}/\text{cm}^2$ ) per pulse, using a variable neutral density filter. We worked mainly with 530 nm excitation, but recorded also some spectra at 475 nm and 650 nm excitation wavelengths. In the THz setup, we use an Optical Parametric Amplifier (Opera Solo, Coherent) in order to generate the visible excitation wavelengths. To obtain 530 nm, we used a configuration called the Sum Frequency of the Signal (SFS), where the signal was generated by parametric amplification, overlapping a part of the 800 nm laser fundamental with a temporally chirped white light beam on a BBO crystal.

## 5.3 Steady State Absorption Spectra

The absorption spectra of the PBDTTPD and PBDTTPB:PCBM films, and the emission spectrum of neat PBDTTPD, are shown in Figure 5.2. The emission spectrum is only slightly Stokes shifted (because geometrical relaxation is limited in the rigid polymer) and presents a vibronic side-band at 720 nm.

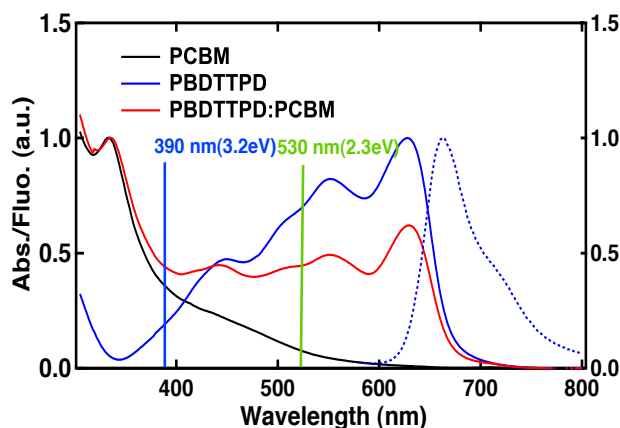


Figure 5.2 Steady state absorption spectra of PBDTTPD, PBDTTPD:PCBM and PCBM (smooth lines), and fluorescence spectrum of neat PBDTTPD film (dotted line, on the right side). The excitation wavelengths of the TA experiments are shown in blue (390 nm excitation) and green (530 nm excitation wavelength).

The absorption spectra of the neat and blended films show also vibronic features, due to the planar backbone conformation in both the ground and the excited state. Quantum calculation confirm that the wave functions are delocalized in the ground state and the excited state (18),(19). Unlike with pBTTT, the broad structured absorption band of PBDTTPD (400-750 nm) does not significantly change between the neat and blended sample, pointing to similar packing of the polymer, which is in agreement with X-ray studies (16).

The photophysical properties of PBDTTPD using different side chains and different molecular weights have been studied in the Ref. (20). According to those results, the spectrum of PBDTTPD with the P3 side chain is the most red shifted compared to the other side chains. This characteristic favours the harvesting of the solar spectrum. Also, the best polymer ordering is obtained with P3, leading to backbone planarization in the solid state (increased conjugation length and delocalization) (16). The highest ordering, short  $\pi$ -stacking distance and face-on orientation on the substrate obtained with the linear P3 side-chain lead to the best solar cell efficiency in the PCBM blend (6.4%), compared to only 3.9% and 2.8% for the others side chains (16). The efficiency can be further enhanced by shortening the TPD alkyl chain by one carbon (up to 8.5%) (17). It was also found that the optimal solar cell efficiency for P3 is obtained with the highest molecular weight (16, 21).

## 5.4 Charge Generation Studied by TA Spectroscopy

### 5.4.1 TA results for neat PBDTTPD films

The photo physics of exciton generation and recombination in neat PBDTTPD measured by TA has already been reported in literature (20). A typical TA spectrum of a neat film shows the ground state bleaching (GSB) and the stimulated emission (SE) as an overlapping structured band peaking at 645 nm (Figure 5.3), as well as an excited state absorption (ESA) band above 740 nm. It has been attributed to singlet ESA with a decay time constant of 150 ps. The global dynamics are associated with additional time constants of 1.6 and 18 ps, due to fast relaxation processes. With high fluence, the global analysis revealed further enhancement of fast components ( $< 22$  ps) due to exciton-exciton and exciton-charge annihilation.

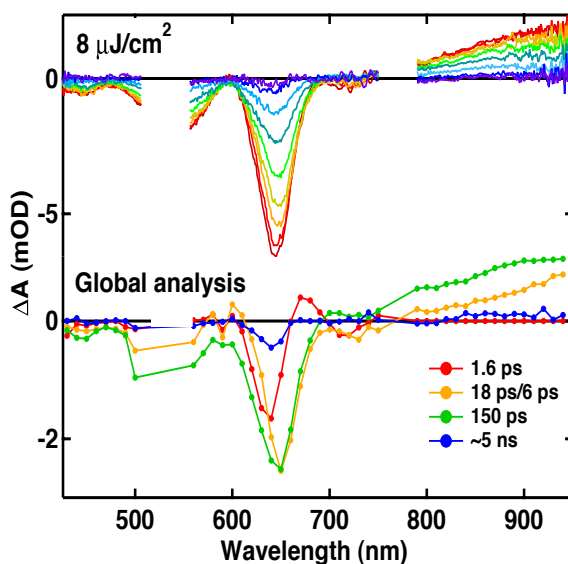


Figure 5.3 Top: TA spectra of neat films of PBDTTPD measured at 530 nm ( $8 \mu\text{J}/\text{cm}^2$ ) at selected time delays between 0.15 ps (red) and 1 ns (violet). Bottom: Amplitude spectra from the global analysis (20).

### 5.4.2 TA results for PBDTTPD:PCBM blends

In this paragraph, we discuss the dynamics of PBDTTPD:PCBM (1:2) studied by TA with 390 nm and 530 nm excitation. Using this polymer:fullerene concentration, the microstructure has been reported to be comparable to the

three phase microstructure of pBTTT:PCBM. In fact, it has been confirmed by X-ray diffraction of the optimized fullerene blend that the microstructure, contains neat polymer aggregates (more disordered than in pBTTT), neat PCBM clusters and regions where the fullerenes mix at molecular level with amorphous PBDTTPD (22). For the P3 side-chain derivative of PBDTTPD, the PCBM clusters appear at a fullerene concentration above 20% by weight. PCBM below this concentration mixes with a limited amount of PBDTTPD, since it was shown that the intermixed regions must be PCBM-rich in order to provide the necessary percolated pathways for electron transport (22). The measurements carried out on this sample were performed at very low fluence (2-4  $\mu\text{j}/\text{cm}^2$ ) in order to avoid the high intensity loss mechanisms: bimolecular recombination, exciton-exciton annihilation (EEA), and exciton-charge annihilation. In these conditions, exciton dissociation is quantitative and most photo-generated charges (80%) survive on the 1 ns time scale. The mechanism of charge generation can then be studied cleanly without artefacts.

In Figure 5.4A and B, the TA spectra of the PBDTTPD:PCBM blend excited at 390 nm (mainly PCBM absorption) and at 530 nm (mainly PBDTTPD absorption) are shown for selected time delays. They were recorded by very carefully keeping the number of absorbed photons constant. Conveniently, the signature of positively charged PBDTTPD is highly characteristic, with a flat absorption in the 660-1000 nm region and a pronounced peak at 880 nm (shown by TA and PIA spectroscopy as well as absorption of the oxidized polymer) (23, 24).

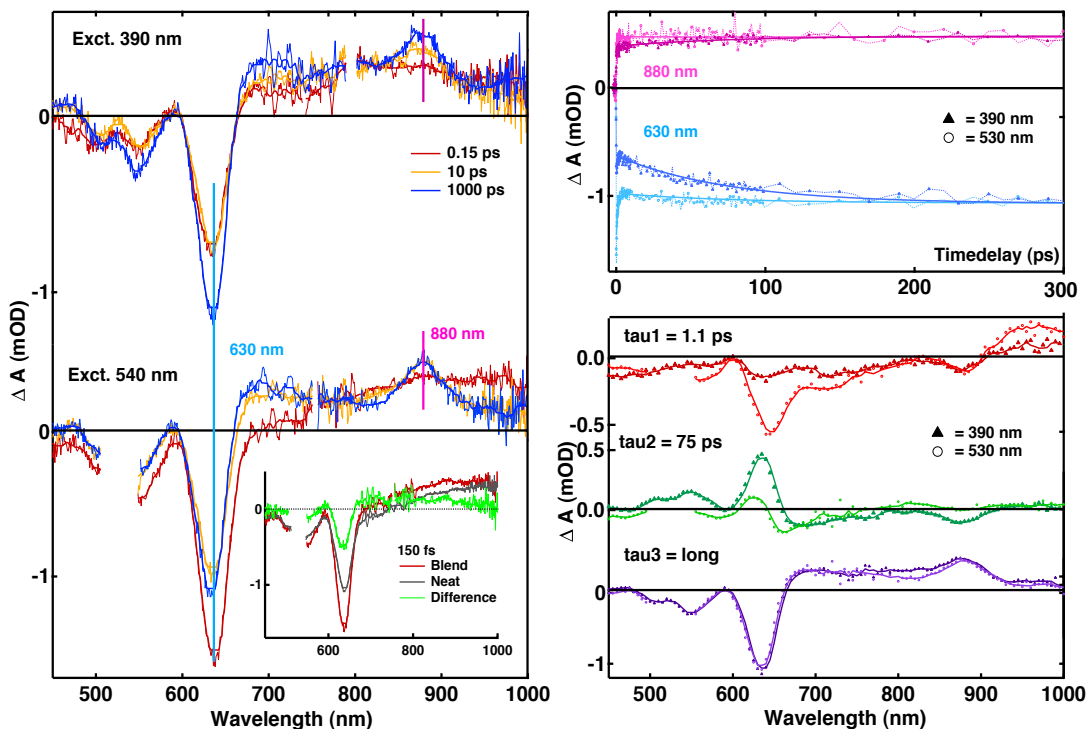


Figure 5.4 (A, B) TA spectra of the P3 derivative of PBDTTPD (14 kDa) blended with PCBM (1:2) recorded at selected time delays following excitation at 390 nm and 540 nm, respectively. Thick solid lines are smoothed and overlaid to the raw experimental data (thin lines). The inset shows an estimation of the spectrum of promptly generated charges at 150 fs, obtained by subtracting the scaled contribution of the neutral exciton measured in the neat PBDTTPD film. (C) TA dynamics probed at 880 nm (charge absorption) and 630 nm (GSB, SE) compared for the two excitation wavelengths (slightly darker colour was used for 390 nm). Solid lines represent the best multiexponential fit. (D) Amplitude spectra associated with the time constants obtained by multi-exponential global analysis of the data.

At the longest time delay (1 ns, blue curve in Figure 5.4), the spectrum of PBDTTPD:PCBM is similar for both excitation wavelengths and is dominated by the polymer's GSB (460-660 nm) and the characteristic charge absorption with the 880 nm peak. This indicates that efficient CS has taken place, either by electron transfer (ET) or by hole transfer (HT), depending on the excitation wavelength. However, in contrast to the 1:1 pBTTT:PCBM blend, where the spectral shape hardly evolved except at ultrafast times, the early TA spectra of PBDTTPD:PCBM are clearly different from the late ones. For both excitation wavelengths, the 880 nm band is only weakly pronounced at 150 fs, pointing to limited prompt CS.

Upon polymer absorption (530 nm, Figure 5.4B), the signatures of the neutral PBDTTPD exciton are visible at early time delays. They include the negative SE band on the red side of the GSB (640-750 nm, coincident with the steady-state emission) (24), and the broad ESA (740-1000 nm, rising at long wavelengths), as identified by comparison to the neat PBDTTPD spectrum shown in Figure 5.3 and in the inset of Figure 5.4B (in grey). The similar aggregation in the neat and blended polymer allows this direct comparison. In the same inset, we subtracted the scaled PBDTTPD signature from the 150 fs spectrum of the blend and obtained the characteristic spectrum of charges. Thus, some ultrafast ET indeed occurs before 150 fs, but the process is not complete. In fact, the amplitude of the 880 nm peak at 150 fs (after subtracting the ESA contribution) is only about 25% of that at late time delays. The small fraction of ET occurring promptly is consistent with the small amount of intimately mixed phase present in the blend (about 20% according to X-ray studies). It confirms that prompt charge generation is related to the intermixed phase. Some prompt HT also occurs in the intermixed regions of the blend upon 390 nm excitation, since the polymer's GSB and charge absorption are partly present at 150 fs, in spite of predominant PCBM excitation (Figure 5.4A).

Most of the ET and HT is nevertheless slower, due to the presence of the neat polymer and fullerene regions, making exciton diffusion to a CS site necessary. This can either be an interface between the neat domains, or between the neat domains and the intermixed regions (for example if the latter form the boundary between the neat domains). At this point we cannot distinguish between the two. In Figure 5.4A (390 nm excitation), there is a rise of the GSB and 880 nm charge peak, mainly between the 10 ps and 1000 ps spectrum. Similarly as with the 1:4 blend of pBTTT:PCBM, this is characteristic of slow HT following diffusion of PCBM excitons through neat fullerene clusters. The slow rise of the GSB (630 nm) and charge peak (880 nm) is clearly visible in the dynamics (Figure 5.4C), as well as in the amplitude spectrum associated with the related 75 ps global time constant (Figure 5.4D). This is an average time scale obtained by exponential analysis, most probably representative of a more multiphasic process caused by different exciton distances from a CS site (25). We note that HT in PBDTTPD:PCBM is overall faster than in the 1:4 pBTTT:PCBM blend, pointing to smaller fullerene clusters. Smaller PCBM domains also explain why the process is less multiphasic (we could use a single time constant), since the distribution of distances is more limited. Based on the reported exciton

diffusion coefficient in C<sub>60</sub> films of  $7.5 \times 10^{-4}$  cm<sup>2</sup>/s, (26) the fullerene excitons diffuse by about 2.5 nm within 75 ps, which allows us to estimate the diameter of the PCBM clusters to 5 nm. This is small enough to ensure complete quenching by HT during the lifetime of the PCBM excitons, unlike in the 1:4 pBTTT:PCBM sample.

In Figure 5.4B (polymer excitation at 530 nm), the spectral changes are clearly different from the ones caused by slow HT. They are dominated by a fast disappearance of the polymer's exciton features (SE, ESA) and a rise of the 880 nm charge band, as expected for delayed ET from neat PBDTTPD domains (see between the 0.15 ps and 10 ps spectra). There is a predominant fast component in the corresponding TA dynamics in Figure 5.4 probed at 630 nm (decay of SE) and at 880 nm (rise of charges). This was globally analysed with a time constant of 1.1 ps. The amplitude spectrum shown in Figure 5.4D confirms the concomitant decay of the negative SE band, rise of the charge absorption and decay of the positive ESA at long wavelengths. The 1.1 ps rise due to delayed ET is even more clearly evident in the dynamics shown in Figure 5.5, measured at 880 nm with 2 μJ/cm<sup>2</sup> fluence. We saw that only about 25% of the ET occurring in PBDTTPD:PCBM is prompt (< 100 fs), while the remaining 75% is delayed (1.1 ps) due to the presence of neat polymer domains. The peculiar efficiency of delayed charge generation in PBDTTPD:PCBM is possible thanks to the planarity of the polymer, which allows the excitons generated in the neat polymer domains to be strongly delocalized, and hence to be able to reach the interface quickly and to be efficiently separated (27).

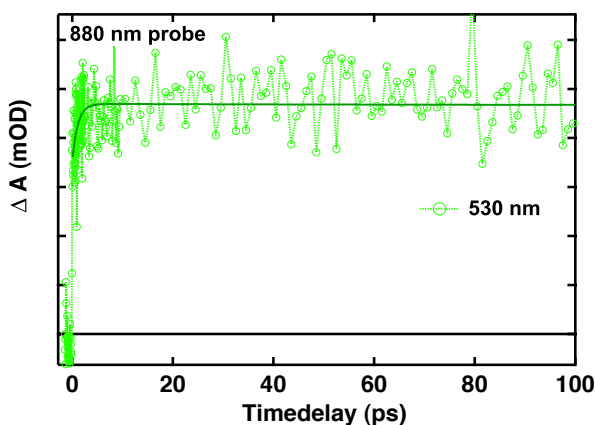


Figure 5.5 Charge dynamics of PBDTTPD:PCBM at a probe wavelength of 880 nm measured for a fluence 2 μJ/cm<sup>2</sup> and excitation wavelength of 530 nm.



We note that the fast component in the dynamics is weakly present also for 390 nm excitation, indicating delayed ET due to residual absorption of the polymer at this wavelength. It was globally analysed using the same 1.1 ps time constant and yields an amplitude spectrum similar in shape as the one associated with ET upon 530 nm excitation (but smaller in size since less PBDTTPD is excited, Figure 5.4D). Analogously, some PCBM is excited at 530 nm, explaining the observed small rise of the polymer GSB by slow HT (between 10 ps and 1000 ps in Figure 5.4B). The amplitude spectrum associated with the corresponding 75 ps time constant has a slightly different shape than upon 390 nm excitation (for example negative indent around 660 nm). We tentatively ascribe this to a weak overlapping contribution of gCR and/or more delayed ET.

Apart from the rather insignificant contribution possibly masked by rise of the signals due to the slow HT (24), we do not see any evidence for decay of the GSB and charges related to gCR, in agreement with high solar cell efficiency of PBDTTPD:PCBM. This shows that excitons initially formed in either the intermixed regions or neat domains are successfully converted to free charges, after their dissociation by ET or HT. In further support of the equally efficient HT and ET pathways, we note the same signal amplitude of the 1 ns spectra recorded at both excitation wavelengths with a similar flux of absorbed photons (Figure 5.4A, B). This also reflects in the converging dynamics at long time delays and the overlapping amplitude spectra related to the long-lived signal (Figure 5.4C, D). Free charges are therefore generated in quasi quantitative yield by both the ET and HT pathways, even if the driving force for HT and ET is different and populates the CT state with more or less excess energy (23, 28). This is evidence that charges formed in the PBDTTPD:PCBM blend (at domain interfaces or in the intermixed phase) are particularly well spatially separated, possibly thanks to the driving force provided by the neat regions, or to the delocalization in the polymer (see below).

Another factor leading to high solar cell efficiency with PBDTTPD is the ability of the polymer to undergo very fast and efficient ET in spite of necessary exciton diffusion out of predominant neat domains. Even if delayed, a time scale of 1.1 ps for ET preceded by exciton migration through PBDTTPD aggregates is still extremely fast. It is not consistent with typical exciton diffusion coefficients of  $2\text{-}3 \times 10^{-3} \text{ cm}^2/\text{s}$  reported for conjugated polymers (29, 30) according to which point-like excitons cover only 0.5 nm within 1 ps. We

therefore suggest that the neat PBDTTPD domains are fairly small (a few nanometers diameter), that exciton migration out of those regions occurs essentially intramolecularly along the same polymer chain, and that it is helped by delocalization. In support of this, we have undertaken elsewhere a very detailed analysis of the distance dependence of the prompt and delayed ET and its interplay with relaxation and delocalization(27). This is summarized in Figure 5.6.

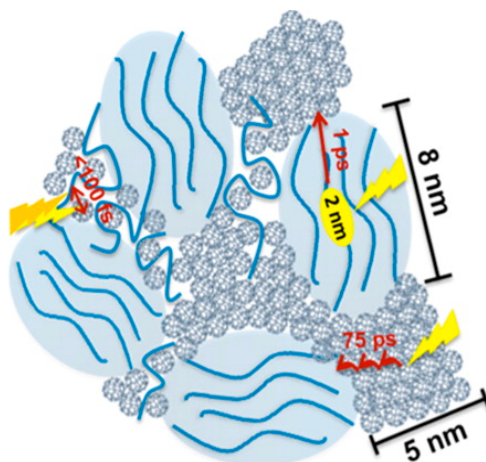


Figure 5.6 Drawing of a three phase microstructure of a PBDTTPD:PCBM (1:2) blend, showing the approximate dimensions of the neat polymer phase, the PCBM phase and the intermixed phase (27).

## 5.5 Results from THz Time-Domain Spectroscopy

The motivation to study the active material of organic solar cells using THz time-domain spectroscopy arises from the peculiarity of this technique: it is particularly appropriate to observe the generation of charges from the exciton on the sub-picoseconds time scales ( $<300 \text{ fs}$ ), since it is sensitive to detect local mobility with a non-contact methodology.

Several papers investigate the process of charge generation and recombination probed in the THz range for neat and blended polymers. The experiments have been performed using very high fluencies ( $\cong 10^{14}\text{-}10^{15}$  photons/cm<sup>2</sup>). The use of high fluencies is usually needed in a THz experiment in order to improve the signal-to-noise ratio and to have a higher amplitude in the THz pump-probe dynamics (the signal amplitude being proportional to the population of photoexcited carriers). The drawback of this

approach is that the real dynamics of charge separation to form free charges is completely masked by artefacts due to the high fluence. In fact, bimolecular recombination in blended samples and exciton-exciton annihilation in neat samples obscure the real dynamics at these fluencies. In addition, several studies presenting the THz dynamics of charge carrier generation for different samples (31-33) show a very similar picture for high fluence measurements: a fast signal rise followed by a decay of a few ps, although we expect a different mechanism for charge generation in different samples. Hence we performed the measurements for the neat and for the blended PBDTTPD samples at very low fluence in the range of  $30 \mu\text{J}/\text{cm}^2$ , where, as also the TA measurements have shown, the annihilation phenomena can be minimized (27). This experimental choice allows to evidence the right dynamics for the electron-hole separation.

### 5.5.1 Neat PBDTTPD: THz dynamics of excitons

The normalized transient THz dynamics for neat and blended PBDTTPD are shown in Figure 5.7, for 530 nm excitation and at high fluence ( $1646 \mu\text{J}/\text{cm}^2$ ). The data was obtained by taking the difference between the pumped and unpumped transmitted THz signal ( $\Delta T$ ) divided by the maximum intensity of the un-pumped THz pulse ( $T$ ).

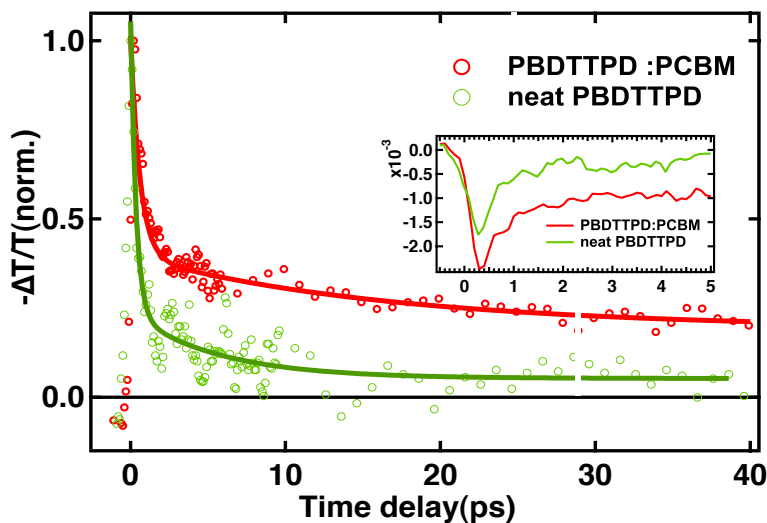


Figure 5.7 Transient THz dynamics of neat PBDTTPD and PBDTTPD:PCBM for high fluence of  $4.4 \cdot 10^{15}$  photons/ $\text{cm}^2$  ( $1646 \mu\text{J}/\text{cm}^2$ ), normalized and not normalized (inset).

Despite the high fluence used for these experiments, the difference in the decay of the transient THz signal between the neat and the blended sample is already very clear: in the neat film after a prompt signal rise, a very fast decay (within a few ps) is observed. In this case, mainly excitons contribute to the (weaker) THz signal, although we cannot exclude the presence of some charges. Although excitons, unlike charges, are not resonant with THz radiation, their polarizability can affect the transmitted THz probe. Fast exciton-exciton annihilation phenomena are prevailing at the high fluence, explaining why the generated excitons have already mostly recombined after 40 ps (there is only a very weak longer-lived offset). In contrast, the natural lifetime of excitons in PBDTTPD is 150 ps, as seen by TA spectroscopy (24).

On the other hand, in the blended sample even at high fluence, it is clear that part of the transient THz signal survives also after 40 ps, most likely due to the generation of charges in the blend. The fast (few picosecond) decay dynamics in this case is mainly due to bimolecular recombination of the charges, although exciton-exciton and exciton-charge annihilation might also contribute. Figure 5.7 shows in the inset the not-normalized transient THz dynamics for the neat and blended samples: surprisingly the amplitude for the neat sample is comparable to the one for the PBDTTPD:PCBM blend. Since the amplitude of the THz signal should be proportional to the population of resonant photoexcited charges, it would be expected that the amplitude in the blend, where charge generation is enhanced, is much higher. This is probably due to the strong artefacts induced by the annihilation phenomena present at this high fluence, which are obscuring the real mechanism of free charges generation.

The transient THz dynamics of the neat PBDTTPD film for lower fluencies ( $90 \mu\text{J}/\text{cm}^2$  and  $30 \mu\text{J}/\text{cm}^2$ ) are shown in Figure 5.8. We note that they were recorded with a different film of PBDTTPD (different polymer batch), which might lead to some differences compared to the data in Figure 5.7.

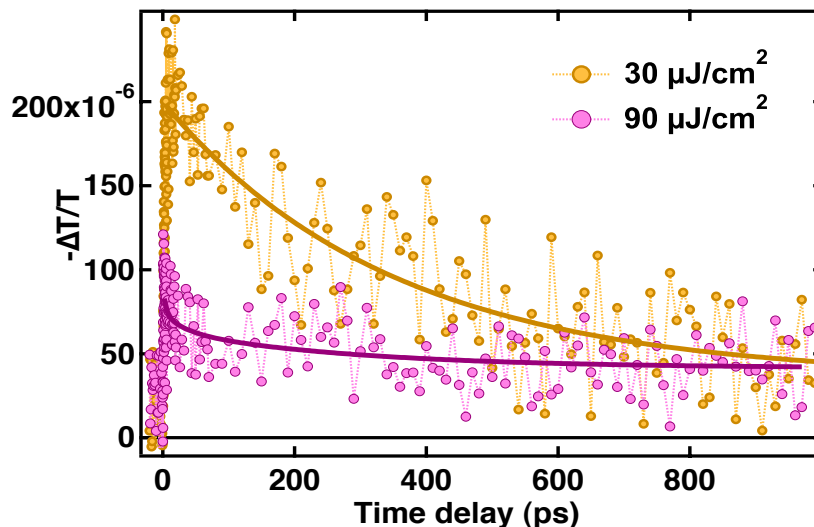


Figure 5.8 Transient THz dynamics of neat PBDTTPD samples excited at 530 nm with 30  $\mu\text{J}/\text{cm}^2$  and 90  $\mu\text{J}/\text{cm}^2$  (not normalized).

The dynamics in Figure 5.8 for the low 30  $\mu\text{J}/\text{cm}^2$  excitation fluence has been analysed using a bi-exponential function with time constants of 6 ps (weak) and 150 ps (predominant). We found similar time constants using TA spectroscopy to study the dynamics of excitons in neat PBDTTPD films (section 5.4.1) (20). This supports that the 150 ps component in the THz data indeed describes the decay of relaxed excitons to the ground state. Also, Laquai et al found a time constant of 200 ps with photoluminescence measurements in PBDTTPD films, which was attributed to the lifetime of intramolecular excited state excitons (3). Hence the THz dynamics in Figure 5.8 are predominantly describing the recombination of exciton species (in the absence of annihilation artefacts), confirming that the bound excitons affect the transmitted THz probe beam and that the dynamics are not only due to photo-generated charges. The confirmation of this picture comes from the photoconductivity spectra recorded at 0.5 ps and 800 ps time delays, shown in the next section.

The transient THz dynamics for the 90  $\mu\text{J}/\text{cm}^2$  fluence present a different behaviour. Surprisingly, the data in Figure 5.8 shows a higher amplitude for the lower fluence (30  $\mu\text{J}/\text{cm}^2$ ) in comparison to the dynamic at 90  $\mu\text{J}/\text{cm}^2$ . The latter has been analysed using a biexponential function with a long component of 1 ns. At this fluence, annihilation phenomena have a more important contribution (27). Banerji et al. have shown that for high fluencies, the dynamics of the neat films can be described with additional fast

components of 0.35 ps and 22 ps. Hence, it is probable that the lower amplitude for the 90  $\mu\text{J}/\text{cm}^2$  fluence can be explained by annihilation processes that are faster than the time resolution of the experiment ( $\approx 300$  fs). Intramolecular excitons thus become “invisible” in the THz data due to ultrafast annihilation. We tentatively suggest that the long 1 ns component is due to more delocalized intermolecular excitons, which are less sensitive to annihilation. Laquai et al. have recently shown the existence of such long-lived species in PBDTTPD films (3).

### 5.5.2 Photoconductivity spectra of neat PBDTTPD films

Photoconductivity spectra in the THz range have been widely used to study inorganic semiconductors (e.g. GaAs) (34), and superconductors. The typical spectral shape found for inorganic materials and for highly doped materials (35) presents a positive real part with a maximum at zero frequency and a positive imaginary part. This shape corresponds to a Drude like model, which describes a material characterized by free charges, as discussed in Chapter 2. A completely different shape has been found in THz spectra of neat conjugated polymers and polymer:fullerene blends that have been recently studied (10-12). In fact, the maximum of the positive real part is no longer at zero frequency and the imaginary part is negative, displaying a minimum value at a non-zero frequency. This behaviour is physically corresponding to a picture in which the charges behave differently compared to inorganic semiconductors. This can come from the presence of bound charges (restoring force) or from backscattered charges.

The commonly reported THz photoconductivity signature for neat polymers in relevant literature presents a monotonical increase with the THz frequency in the positive real and negative imaginary part. This behaviour has been found specifically for semi-crystalline polymers such as P3HT between 0.2 and 2 THz (9) and also for MEH-PPV between 0.2 and 1.2 THz (14). The authors corroborate that this behaviour is characteristic of a dispersive transport in a disordered medium. As the polymers exhibit nanoscale disorder, the model used to describe the spectra is the Drude–Smith model, which accounts for strong carrier localization. It seems that the species observed in P3HT and MEH-PPV are weakly bound excitons. Also Sundstroem et al. observe weakly coulombically bound species in neat APFO polymer.

Figure 5.9 shows the photoconductivity spectra for neat PBDTTPD film recorded at time delays of 0.5 ps and 800 ps, with a high fluence of  $4.4 \cdot 10^{15}$  photons/cm<sup>2</sup> at an excitation wavelength of 530 nm.

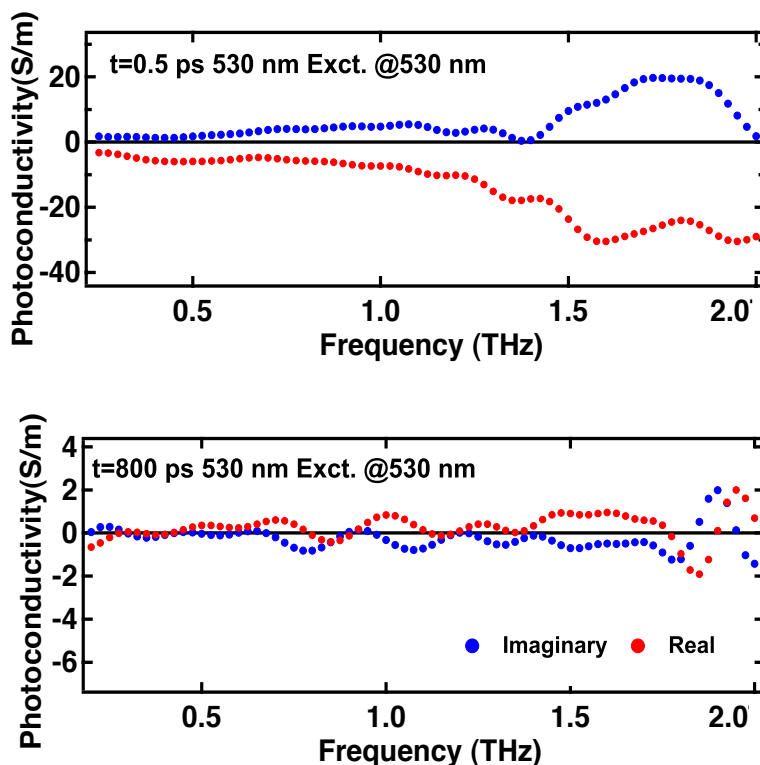


Figure 5.9 THz photoconductivity spectra of neat PBDTTPD film recorded at time delays of 0.5 ps and 800 ps using a fluence of  $4.4 \cdot 10^{15}$  photons/cm<sup>2</sup> at 530 nm excitation wavelength.

Comparing the spectra at 0.5 ps and 800 ps, it is clear that practically all the excitons and charges have recombined after 800 ps, as has been shown already in the transient THz dynamics for high fluences reported in Figure 5.7. The microscopic origin of the photoconductivity signature in organic materials is a recent topic of debate. A close look at the 0.5 ps spectrum reveals that the real part of the photoconductivity is almost zero for low THz frequencies and becomes slightly higher for higher frequencies, reaching a maximum at 1.7 THz. The negative imaginary part is more important than the positive real part, as it has a larger amplitude. It has a minimum at a THz frequency slightly lower than the maximum of the real part. This asymmetrical behaviour between the real part and the imaginary part seems to describe mostly bound species. Among all the theoretical models (36), the presence of a maximum in the real part and a minimum in the imaginary part corresponds to a photophysical situation in which there is the presence of a

restoring force. The latter can come from back-scattering from the end of a polymer segment (Drude-Smith model) or from a torsional disorder (37). In the Drude–Smith model, the negative imaginary part should become zero in correspondence with the maximum of the positive real part. Yet this is not the case, so that we suggest that the observed shape of the photoconductivity spectra is closer to an Oscillator–Lorentzian model. This goes beyond the aim of this thesis and needs further experimental and theoretical investigation. The presence of bound species in the neat PBDTTPD sample is further confirmed if we consider the signal at 0.5 ps shown in Figure 5.10. This is the difference between  $E_{\text{pumped}}$  (THz electric field in the presence of the excitation pump) and  $E_{\text{unpumped}}$  (THz electric field without the pump). The  $E_{\text{unpumped}}$  field is shown as a reference. For samples with an important presence of photogenerated free charges,  $\Delta E$  resembles the mirror image of the unpumped field, indicating absorption of the THz radiation by resonant charges. In contrast, the  $\Delta E$  signal for neat PBDTTPD film (red curve in Figure 5.10a)) is reproducing the same shape as the unpumped field with the maximum shifted to the right. This is due to the presence of bound species in the neat sample, which do not absorb the THz radiation (as free charges do) but shift it temporally. Hence the field appears to be only delayed in time with respect to the unpumped radiation. This physical behaviour is a clear signature of excitons in the neat phase of PBDTTPD. Hence, the shifted THz electric field gives some information about the fact that the species we detect have a large polarizability and in this situation also an important restoring force. The Fourier transformation of  $E_{\text{unpumped}}$  and  $\Delta E$  shown in Figure 5.10 b) gives information about the THz range in which it is possible to obtain useful information and to extract the photoconductivity spectra.



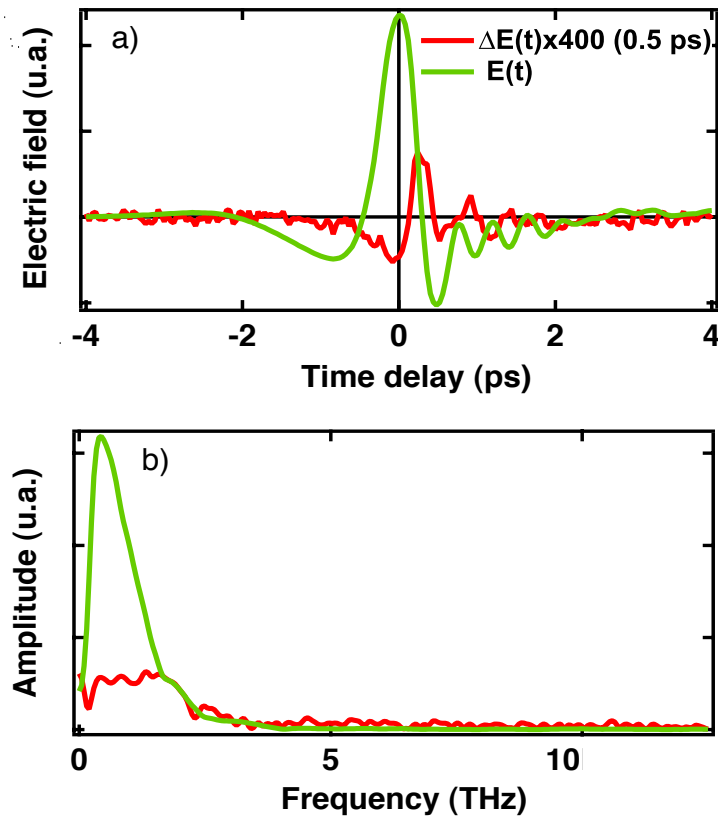


Figure 5.10 a) Transmitted unpumped THz electric field (green) for neat PBDTTPD film and difference between the pumped THz field and the unpumped THz field ( $\Delta E = E_{\text{pumped}} - E_{\text{unpumped}}$ , red), 0.5 ps after excitation at 530 nm with a fluence of  $4.4 \cdot 10^{15}$  photons/cm<sup>2</sup>, multiplied by a factor 400 to allow the comparison. b) Fourier-transformed THz spectrum (frequency domain) of the THz fields shown in panel a).

To confirm that the information in Figure 5.10 is not only related to the high fluence, Figure 5.11 shows the transmitted THz electric field (unpumped and  $\Delta E$  20 ps after excitation) for a lower fluence of  $90 \mu\text{J}/\text{cm}^2$  (the related dynamics are shown in Figure 5.8). Also in this case, the shift of the THz field corresponds to a situation where the generated species are bound. Indeed, as we expect, in the neat PBDTTPD film at 20 ps, the singlet excited state is initially populated and recombines to the ground state. This further supports the link between the THz electric field shift and the presence of bound species.

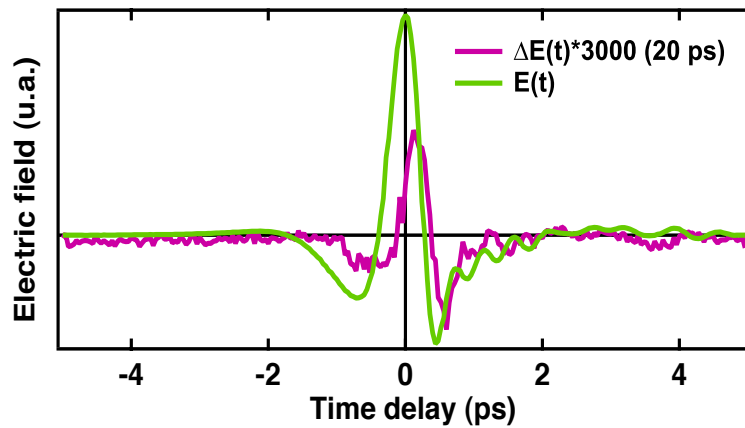


Figure 5.11 Transmitted THz electric field for neat PBDTTPD film, for the unpumped case and  $\Delta E = E_{\text{pumped}} - E_{\text{unpumped}}$ , 20 ps after excitation at 530 nm with  $90 \mu\text{J}/\text{cm}^2$  fluence (corresponding dynamics are shown in dark pink in Figure 5.8).

### 5.5.3 Delayed charge generation in PBDTTPD:PCBM

The normalized transient THz dynamics for the PBDTTPD:PCBM blend are shown in Figure 5.12 for 530 nm excitation at various fluencies. The analysis was done using three-exponential functions. The measurements shown in Figure 5.12 were performed for a second time (first data not shown) after increasing the averaging for a higher number of scans, in order to improve the signal-to-noise ratio (several days accumulation).

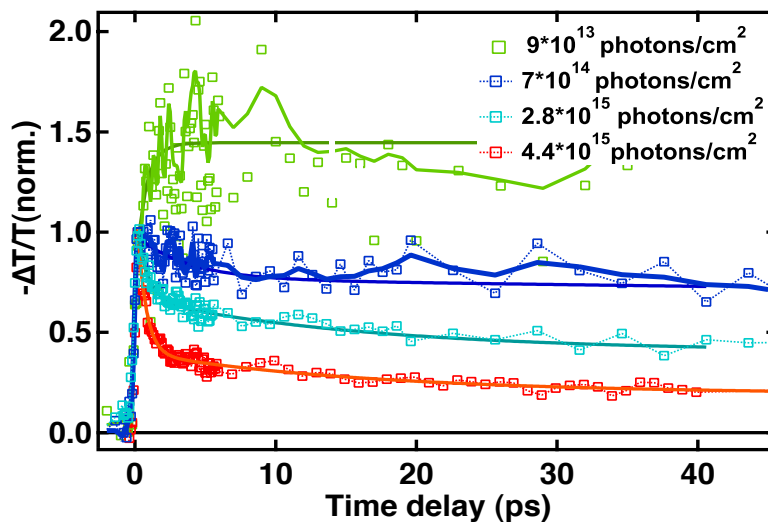


Figure 5.12 Transient THz dynamics for PBDTTPD:PCBM, with varying excitation fluence at 530 nm:  $9 \cdot 10^{13}$  photons/ $\text{cm}^2$  ( $30 \mu\text{J}/\text{cm}^2$ ),  $7 \cdot 10^{14}$  photons/ $\text{cm}^2$  ( $264 \mu\text{J}/\text{cm}^2$ ),  $2.8 \cdot 10^{15}$  photons/ $\text{cm}^2$  ( $1055 \mu\text{J}/\text{cm}^2$ ), and  $4.4 \cdot 10^{15}$  photons/ $\text{cm}^2$  ( $1646 \mu\text{J}/\text{cm}^2$ ). The data have been normalized at 0.2 ps.

The dynamics for the highest intensity shows an instantaneous rise, a fast decay and then a slower decay of 1000 ps, in agreement with the discussion of Figure 5.7. This dynamics confirms the previous measurement, which was carried out on the same sample and in the same range of excitation fluence. Since for the high excitation intensity, we have a higher density of photogenerated excitons and charges, the exciton annihilation and bimolecular charge pair recombination phenomena are prevailing, which causes the very fast decay times. This agrees with the results obtained with TA spectroscopy by Banerji et al. (27). It is probable that we missed part of the ultrafast decay, which occurs faster than the time resolution. By decreasing the fluence, the amplitude of the fast decay in the THz dynamics becomes less pronounced. When the fluence is reduced by two orders of magnitude, we observe instead a 1 ps rise in the dynamics (Figure 5.12). This originates from the generation of charges directly by exciton dissociation. The 1 ps rise is in agreement with the delayed 1 ps CS observed in the TA experiments (visible pump and probe, section 5.4.2) (20). Those experiments showed that CS in PBDTTPD:PCBM is partly prompt (<100 fs) and partly delayed (1 ps), for excitons generated in neat polymer domains that need to diffuse to an interface. To our knowledge, we report here the first observation of delayed charge generation in polymer:fullerene blends by THz spectroscopy. This outlines the importance of using low excitation intensity in THz experiments in order to observe the real dynamics of charge generation.

The fluence dependent study allows us to find the local mobility of photogenerated charges from the non-normalized amplitude of the THz dynamics. In fact, it is possible to extract the product of the mobility ( $\mu$ ) and of the charge generation efficiency ( $\phi$ ), starting from the initial (0.4 picosecond)  $\Delta T/T$  amplitude (not normalized), using the following equation:

$$\mu\phi = \frac{\Delta\sigma_0}{en_0^{photon}} \quad 1)$$

where  $n_0^{photon} = (1 - e^{-\alpha d}) I_0/d$  is the photoexcited carrier density, extracted from the absorption coefficient  $\alpha$ , the number of incident photons  $I_0$  per unit of area, and the film thickness  $d$ .  $e$  is the electronic charge and  $\Delta\sigma_0$  is the photoconductivity, i.e. the change in sample conductivity extracted from the change in THz transmission  $\Delta T/T$  (38):

$$\Delta\sigma_0 = \frac{1+n}{Z_0 d} \left( \frac{1}{1 + \frac{\Delta T}{T}} - 1 \right) \quad 2)$$

where  $Z_0$  is the impedance of free space,  $d$  is the thickness of the sample and  $n$  is the quartz substrate refractive index (39).

The values of the local mobility extracted from the photoconductivity measurements (in Figure 5.12) for PBDTTPD:PCBM are shown in Table 1. These values are of the same order of magnitude of as the ones found by Parkinson et al. in P3HT:PCBM (38), who reported a value of  $\mu\phi = 0.11$  cm<sup>2</sup>/Vs at a fluence of 500  $\mu$ J/cm<sup>2</sup> (after a fitting procedure of photoconductivity as a function of fluence), and by Turchinovich et al. in PTB7:PCBM (11), who found a value of  $\mu\phi = 0.3$  cm<sup>2</sup>/Vs, 0.3 ps after excitation at 530  $\mu$ J/cm<sup>2</sup> (extracted from the Drude-Smith model). We note that the  $\mu\phi$  product gives in our case a lower-limit value of the local mobility, since the charge generation efficiency at the initial time delay is  $< 1$  due to delayed CS. The decrease of  $\mu\phi$  at higher fluencies might be related to a further decrease of  $\phi$  caused by annihilation faster than the time resolution of the experiment. However, the precise connection between local mobility and fluence needs further investigation and a broader range of fluencies, which is out of scope of the present work.

Fluence ( $\mu$ J/cm <sup>2</sup> )	Local mobility(cm <sup>2</sup> /Vs)
264.15	0.066
120.75	0.11
55.09	0.14
30	0.17

Table 1 Local mobility multiplied by the efficiency of charge generation ( $\mu\phi$ ) for different fluencies, found using the equation 1 for PBDTTPD:PCBM.

Long-range mobility measurements have been performed by McGehee et al. on the same polymer:fullerene blend using current-voltage characteristics. They found values orders of magnitude smaller compared to the local mobility that we report using non-contact THz spectroscopy (the long-range hole mobility is of the order of 10<sup>-4</sup> cm<sup>2</sup>/Vs for the neat and 10<sup>-5</sup> cm<sup>2</sup>/Vs in the blended sample). The physical meaning of the local mobility probed by THz spectroscopy has been recently explained by McGehee (40). It is more related to the frequency of attempts for an electron-hole pair to split (the intrinsic hopping rate) and to charge motion on the very short length scale (without

grain boundaries). The local mobility has also been found using a non-contact probe in the microwave range (time-resolved microwave conductivity, TRMC)(41). Their values are lower in relation to the ones found with the THz method. Excitation fluence might have affected the local mobility in the microwave field for neat P3HT.

#### 5.5.4 Photoconductivity spectra of PBDTTPD:PCBM

The photoconductivity spectra shown in Figure 5.13 for the PBDTTPD:PCBM blend, excited at 530 nm at a fluence of  $4.4 \cdot 10^{15}$  photons/cm<sup>2</sup> per pulse confirm that the generated species are charges. In fact the photoconductivity spectra, as discussed above, allow to distinguish bound excitons or charge transfer states from charges. The real and imaginary part of the photoconductivity has been calculated from the amplitude and the phase of the transmitted THz electric field with respect to a reference quartz plate, at two fixed pump-probe delay times. The spectra obtained at 0.5 ps and 800 ps are shown in Figure 5.13.

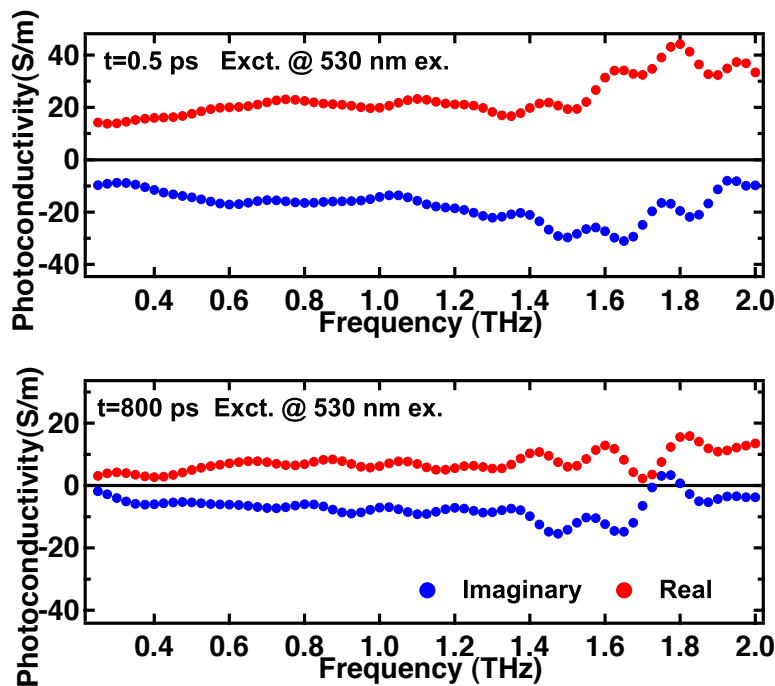


Figure 5.13 Photoconductivity spectra for PBDTTPD:PCBM at a time delay of 0.5 ps and 800 ps following excitation at 530 nm with  $4.4 \cdot 10^{15}$  photons/cm<sup>2</sup> per pulse.

The situation is quite different from the spectra described for the neat polymer (Figure 5.9). In particular, the amplitude of the real part is more important than the corresponding real part in the neat sample, especially at the lower THz frequencies. This is a clear signature of the presence of free charges (polarons) while the presence of the negative part is describing a localization of charges. The latter could come from some backscattering effect (caused by disorder effects) or due to charges that are not completely free (in contrast to an inorganic material), which may be confined polarons. Hence, the photoexcited species observed at 0.5 ps still have some characteristics of a bound system, possibly due to the delayed presence of excitons or to the formation of a charge transfer (CT) state.

At 0.5 ps, it is possible to observe a positive peak for the real part of the photoconductivity around 1.7 THz, and a negative peak for the imaginary part around 1.5 THz. The spectral shape with a maximum and a minimum shown in Figure 5.13 has never been observed for polymer:fullerene blends in the range between 0.2 THz and 2 THz. It needs further confirmation and investigation. Turchinovich et al. found in the same THz range for an amorphous polymer blend (PTB7:PCBM) a spectral shape with the real and imaginary part increasing in amplitude at higher frequency (11). They suggest that this shape originates from a model where the mobile charges are hindered by a potential well created in a polaron pair. The photophysical model used to describe this situation is the Drude-Smith model. They found also that the mobility decreases at higher excitation density with increasing carrier-carrier interaction (11).

In Figure 5.13, it is possible to observe a decrease in the amplitude of the THz photoconductivity going from 0.5 ps to 800 ps, since less charge density survives until 800 ps (annihilation and recombination effects, see Figure 5.7). At 800 ps, there is evidence that the charges are the same kind of species as seen at 0.5 ps. This is also confirmed by looking at Figure 5.14, which shows the ratio between the real and the imaginary part of the photoconductivity at 0.5 ps and 800 ps. It is clear that the ratio has for both time delays almost the same value, indicating that the species detected are similar. The important imaginary part indicates that bound species are somewhat present at long time delays, which could be a contribution of (delocalized interchain) excitons that decay more slowly, or of bound charge pairs, or it could be related to the nature of relatively free charges in disordered polymers.

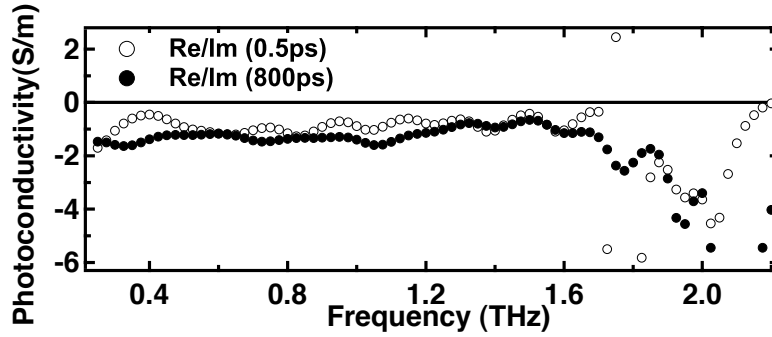


Figure 5.14 Ratio between the real and the imaginary part of the photoconductivity spectra of PBDTTPD:PCBM shown in Figure 5.13, at 0.5 ps and 800 ps.

Figure 5.15 illustrates the photo-modulation of the THz electric field ( $\Delta E = E_{\text{pumped}} - E_{\text{unpumped}}$ ) at 0.5 ps and 800 ps, with respect to the transmitted unpumped THz electric field for the PBDTTPD:PCBM blend. In contrast to the photo-modulated electric field for neat PBDTTPD polymer shown in Figure 5.10, it is clear that the  $\Delta E$  electric fields at both delay times mirror the unpumped electric field, and are only very slightly shifted to the left side by 0.1 ps (the origin of the shift is unclear and possibly within the noise). This characteristic behaviour clearly corresponds to a photophysical picture where the THz field is absorbed by the photo-generated charges in the blended sample, and where the restoring force, which is typical of a strongly polarizable exciton species, is absent. The different amplitude between the  $\Delta E$  field at 0.5 ps and the field at 800 ps is coming from the bimolecular recombination phenomena at high fluence. Finally, it is possible to consider the photo-modulation of the electric field at 0.5 ps and 800 ps displayed in Figure 5.15 as the THz signature of the charges (polarons). A similar signature at 2 ps has been found by Turchinovich et al. (11) on another amorphous polymer (PTB7) blended with PCBM and also by J. Elligson et al. on P3HT:PCBM (31).

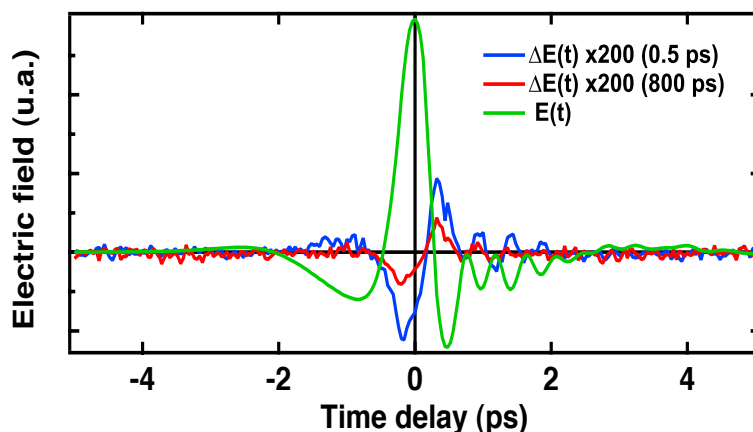


Figure 5.15 Transmitted THz electric field recorded without pump (green), and photo-modulated electric field ( $\Delta E = E_{\text{pumped}} - E_{\text{unpumped}}$ ) for PBDTTPD:PCBM at time delays of 0.5 ps and 800 ps following excitation at 530 nm with  $4.4 \cdot 10^{15}$  photons/cm<sup>2</sup> per pulse.

The above interpretation can be confirmed for a measurement at low fluence ( $9 \cdot 10^{13}$  photons/cm<sup>2</sup>), as shown in Figure 5.16. In fact, the modulated electric fields at 0.5 ps and at 800 ps have the same shape as the ones shown in Figure 5.15 for the highest fluence, and mirror the unpumped field. The amplitude at the two time delays is nevertheless now similar. This is due to the fact that at this fluence, the generated charges do not recombine on the 1 ns time scale because the bimolecular recombination phenomena have been eliminated. They do not undergo a significant decrease in local mobility, either, as this would also affect the THz signal. Figure 5.16 is decisively showing that the charges at 0.5 ps and 800 ps are the same kind of species. Specifically the detected species are related to free charges (polarons), since the characteristic mirrored disposition of the modulated field with respect to the unpumped field clearly describes a situation where the energy contained in the THz electric field is absorbed and not delayed by the generated charges (i.e. the generated charges are relatively free to react to the probe THz field). Hence it is possible to conclude that the process of free charge generation in the blend seems to happen following a direct pathway.



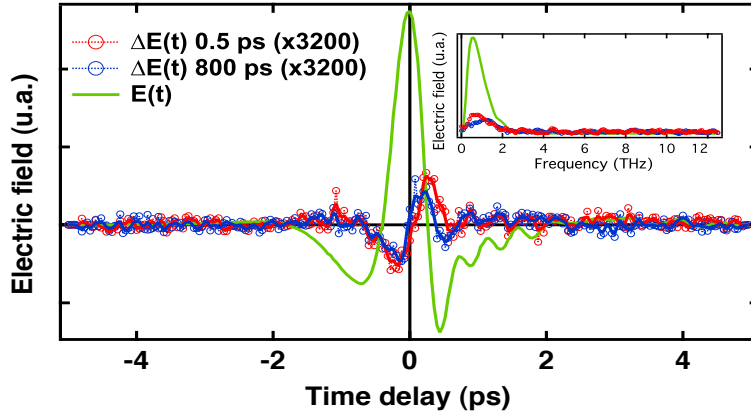


Figure 5.16 Transmitted THz electric field recorded without pump (green), and photo-modulated electric field ( $\Delta E = E_{\text{pumped}} - E_{\text{unpumped}}$ ) for PBDTTPD:PCBM at time delays of 0.5 ps and 800 ps following excitation at 530 nm with  $9 \cdot 10^{13}$  photons/cm<sup>2</sup> ( $30 \mu\text{J}/\text{cm}^2$ ) per pulse.

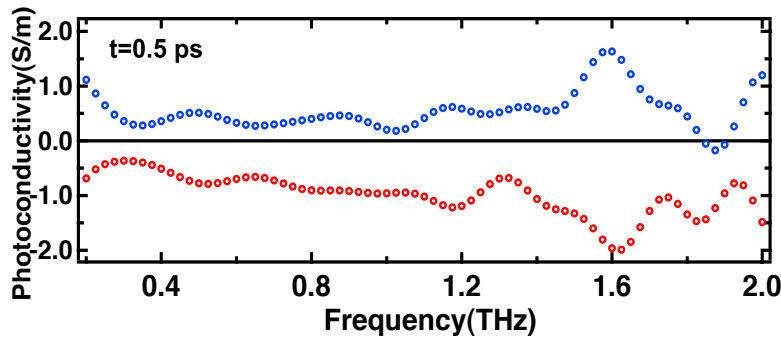


Figure 5.17 Real and imaginary part of the photoconductivity for PBDTTPD:PCBM at a time delay of 0.5 ps after excitation at 530 nm with the lowest fluence ( $30 \mu\text{J}/\text{cm}^2$ ).

The real and the imaginary part of the photoconductivity at the lowest fluence ( $30 \mu\text{J}/\text{cm}^2$ ) is shown in Figure 5.17. Those spectra further corroborate the hypothesis supporting the presence of charges at 0.5 ps. Indeed, not only the presence of the real and the imaginary part can be confirmed with respect to the spectra at highest fluence. In addition, the almost flat shape until 1.6 THz, peaking at 1.7 THz, is still evident at this fluence. The presence of a broad band in the THz range (0.1-3 THz) has been found to be a typical signature of amorphous and non-transparent polymers (42). This seems to be in agreement with the presence of the peak in the real and imaginary part observed for PBDTTPD:PCBM, which has the characteristic to be amorphous and non-transparent. Hence, the theoretical model describing the spectra has strong components coming from the Lorentzian oscillator. To confirm this needs further investigation and is beyond the scope of this thesis.

The connection between the shape of the photo-modulated THz field and the presence of charges can be further confirmed if we study the blended sample after performing an above-gap excitation at 475 nm (2.6 eV), shown in Figure 5.18 for a time delay of 0.5 ps (the energy gap of the PBDTTPD is 1.8 eV). Indeed the THz field  $\Delta E(t, \Delta t = 0.5 \text{ ps})$  shows all the characteristics connected with the presence of charges: it mirrors the unpumped THz field and it is not shifted with respect to it, indicating absorption of the THz probe.

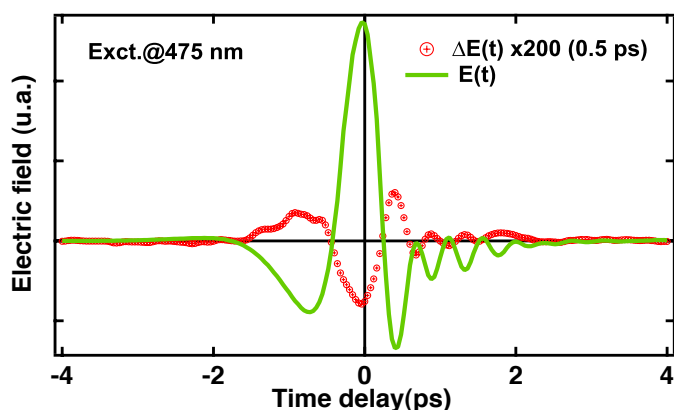


Figure 5.18 Transmitted THz electric field recorded without pump (green), and photo-modulated electric field  $\Delta E(t, \Delta t=0.5 \text{ ps})$  for PBDTTPD:PCBM at a time delay of 0.5 ps after excitation at 475 nm with  $4.4 \cdot 10^{15}$  photons/cm<sup>2</sup> per pulse.

The photoconductivity spectra for the 475 nm excitation wavelength are shown in Figure 5.19 and are compared with the ones for the 530 nm excitation wavelength. It is obvious that the amplitude of the real part of the photoconductivity is more important than the imaginary part, which is almost zero at 475 nm. Also, the shape of the real part is different in relation to the one at 530 nm: it increases linearly with the frequency and it does not have any peak. This behaviour is more similar to the signature of the real part of the photoconductivity for P3HT:PCBM (38). The important amplitude of the real part, and quasi absence of the imaginary part, correspond to a picture where the charges are not bound. Specifically, the increase of the real part with frequency could describe a situation where the charges are free to respond to the THz probe, in contrast to the real part at 530 nm excitation wavelength. This suggests that excess excitation energy can have some effect on the nature of photo-generated charges.

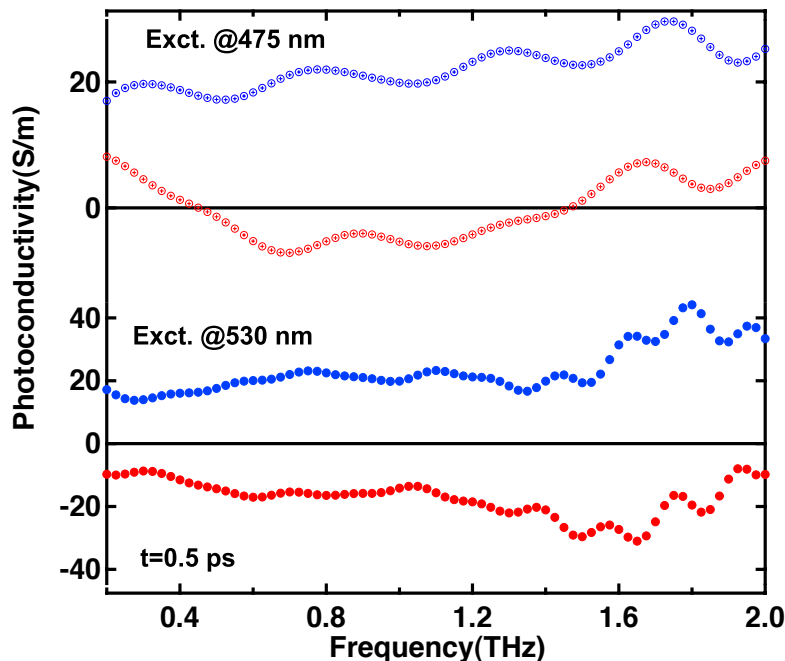


Figure 5.19 Comparison between the frequency dependence of the real part (blue circles) and the imaginary part (red circles) of the THz photoconductivity in PBDTTPD:PCBM measured for 530 nm excitation wavelength (full circles) and 475 nm excitation wavelength (empty circles) at time delay of 0.5 ps for  $4.4 \cdot 10^{15}$  photons/cm<sup>2</sup> per pulse.

## 5.6 Conclusion

In Chapter 5, we have investigated the charge generation and dynamics in neat PBDTTPD and PBDTTPD:PCBM blends with well-characterized three-phase microstructure upon selective excitation of either the fullerene (390 nm) or the polymer (530 nm) with transient absorption (TA) spectroscopy. These results have been compared with the THz time domain measurements for excitation at 530 nm and 475 nm on the same samples. The TA results emphasize that a low fluence is needed for the blended sample in order to be able to observe the photo-physical process of charge generation without interference of annihilation and bimolecular recombination artefacts. The low fluencies, which allow the removal of the bimolecular recombination phenomena, are also needed in the THz measurements to provide evidence the accurate process of charge generation, the useful dynamics and the correct value of local mobility (which seems to be fluence dependent). Both techniques confirm that the charge generation in the blended sample has a delayed component originating from excitons created in neat polymer domains which, thanks to delocalization, can reach the interface and dissociate to charges (polarons) on a time scale of 1 ps. From the TA results, it

is clear that the charges are also generated from the dissociation of excitons from the PCBM domains (75 ps), and from the intermixed phase (100 fs). The comparison of the TA results with the THz results confirms both the dynamics of charge generation and also clearly differentiates coulombically bound excitons/charges from free charges (polarons). In fact, although the THz spectroscopy seems to not be the most suitable technique in order to measure polymers charge generation processes (because excessively long accumulation is necessary at low fluence), it is an effective tool to detect the presence of strongly coulombically bound species, and thus to investigate the nature of charge carriers in polymer:fullerene blends.

## 5.7 References

1. C. Cabanetos *et al.*, Linear Side Chains in Benzo[1,2-b:4,5-b']dithiophene-Thieno[3,4-c]pyrrole-4,6-dione Polymers Direct Self-Assembly and Solar Cell Performance. *J. Am. Chem. Soc.* **135**, 4656 (2013).
2. J. A. Bartelt *et al.*, The importance of fullerene percolation in the mixed regions of polymer-fullerene bulk heterojunction solar cells. *Adv. Energy Mater.* **3**, 364 (2013).
3. C. Dyer-Smith, Howard, I. A., Cabanetos, C., Labban, A. E., Beaujuge, P. M. and Laquai, F. , *Adv. Energy Mater.*, Interplay Between Side Chain Pattern, Polymer Aggregation, and Charge Carrier Dynamics in PBDTTPD:PCBM Bulk-Heterojunction Solar Cells. *Adv. Energy Mater.*, (2015).
4. X. Jiang *et al.*, Spectroscopic studies of photoexcitations in regioregular and regiorandom polythiophene films. *Adv. Funct. Mater.* **12**, 587 (2002).
5. O. Esenturk, J. S. Melinger, E. J. Heilweil, Terahertz mobility measurements on poly-3-hexylthiophene films. Device comparison, molecular weight, and film processing effects. *J. Appl. Phys.* **103**, 023102/1 (2008).
6. F. Wang *et al.*, Exciton polarizability in semiconductor nanocrystals. *Nat. Mater.* **5**, 861 (2006).
7. R. Mauer, M. Kastler, F. Laquai, The Impact of Polymer Regioregularity on Charge Transport and Efficiency of P3HT:PCBM Photovoltaic Devices. *Adv. Funct. Mater.* **20**, 2085 (2010).
8. O. Esenturk, R. J. Kline, D. M. DeLongchamp, E. J. Heilweil, Conjugation Effects on Carrier Mobilities of Polythiophenes Probed by Time-Resolved Terahertz Spectroscopy. *J. Phys. Chem. C* **112**, 10587 (2008).
9. P. D. Cunningham, L. M. Hayden, Carrier Dynamics Resulting from Above and Below Gap Excitation of P3HT and P3HT/PCBM Investigated by Optical-Pump Terahertz-Probe Spectroscopy. *J. Phys. Chem. C* **112**, 7928 (2008).
10. C. S. Ponseca *et al.*, Ultrafast Terahertz Photoconductivity of Bulk Heterojunction Materials Reveals High Carrier Mobility up to Nanosecond Time Scale. *J. Am. Chem. Soc.* **134**, 11836 (2012).
11. Z. Jin *et al.*, Ultrafast Terahertz Photoconductivity of Photovoltaic Polymer-Fullerene Blends: A Comparative Study Correlated with Photovoltaic Device Performance. *J. Phys. Chem. Lett.* **5**, 3662 (2014).

12. C. S. Ponseca *et al.*, Electron and Hole Contributions to the Terahertz Photoconductivity of a Conjugated Polymer: Fullerene Blend Identified. *J. Phys. Chem. Lett.* **3**, 2442 (2012).
13. E. Hendry *et al.*, Interchain effects in the ultrafast photophysics of a semiconducting polymer: THz time-domain spectroscopy of thin films and isolated chains in solution. *Phys. Rev. B: Condens. Matter Mater. Phys.* **71**, 125201/1 (2005).
14. E. Hendry, J. M. Schins, L. P. Candeias, L. D. A. Siebbeles, M. Bonn, Efficiency of exciton and charge carrier photogeneration in a semiconducting polymer. *Phys. Rev. Lett.* **92**, 196601/1 (2004).
15. Y. P. Zou *et al.*, A Thieno[3,4-c]pyrrole-4,6-dione-Based Copolymer for Efficient Solar Cells. *J Am Chem Soc* **132**, 5330 (Apr 21, 2010).
16. C. Piliego *et al.*, Synthetic Control of Structural Order in N-Alkylthieno[3,4-c]pyrrole-4,6-dione-Based Polymers for Efficient Solar Cells. *J Am Chem Soc* **132**, 7595 (2010).
17. C. Cabanetos *et al.*, Linear Side Chains in Benzo[1,2-b:4,5-b']dithiophene-Thieno[3,4-c]pyrrole-4,6-dione Polymers Direct Self-Assembly and Solar Cell Performance. *J Am Chem Soc* **135**, 4656 (2013).
18. C. Risko, M. D. McGehee, J.-L. Bredas, A quantum-chemical perspective into low optical-gap polymers for highly-efficient organic solar cells. *Chem. Sci.* **2**, 1200 (2011).
19. I. Hwang, S. Beaupre, M. Leclerc, G. D. Scholes, Ultrafast relaxation of charge-transfer excitons in low-bandgap conjugated copolymers. *Chem. Sci.* **3**, 2270 (2012).
20. A. A. Paraecattil, S. Beaupre, M. Leclerc, J.-E. Moser, N. Banerji, Intensity Dependent Femtosecond Dynamics in a PBDTPD-Based Solar Cell Material. *J. Phys. Chem. Lett.* **3**, 2952 (2012).
21. B. R. Aich, J. Lu, S. Beaupre, M. Leclerc, Y. Tao, Control of the active layer nanomorphology by using co-additives towards high-performance bulk heterojunction solar cells. *Organic Electronics* **13**, 1736 (2012).
22. J. A. Bartelt *et al.*, The importance of fullerene percolation in the mixed regions of polymer-fullerene bulk heterojunction solar cells. *Adv. Energy Mater.* **3**, 364 (2013).
23. E. T. Hoke *et al.*, Recombination in polymer:fullerene solar cells with open-circuit voltages approaching and exceeding 1.0 V. *Adv. Energy Mater.* **3**, 220 (2013).

24. A. A. Paraecattil, S. Beaupré, M. Leclerc, J.-E. Moser, N. Banerji, Intensity Dependent Femtosecond Dynamics in a PBDTTPD-Based Solar Cell Material. *Journal of Physical Chemistry Letters* **3**, 2952 (2012/10/18, 2012).
25. A. Siemiarczuk, B. D. Wagner, W. R. Ware, Comparison of the Maximum-Entropy and Exponential Series Methods for the Recovery of Distributions of Lifetimes from Fluorescence Lifetime Data. *J Phys Chem-Us* **94**, 1661 (Feb 22, 1990).
26. M. C. Fravventura *et al.*, Determination of Singlet Exciton Diffusion Length in Thin Evaporated C-60 Films for Photovoltaics. *Journal of Physical Chemistry Letters* **3**, 2367 (Sep 6, 2012).
27. A. A. Paraecattil, N. Banerji, Charge Separation Pathways in a Highly Efficient Polymer: Fullerene Solar Cell Material. *J. Am. Chem. Soc.* **136**, 1472 (2014).
28. A. A. Bakulin *et al.*, Charge-Transfer State Dynamics Following Hole and Electron Transfer in Organic Photovoltaic Devices. *The Journal of Physical Chemistry Letters* **4**, 209 (2013/01/03, 2012).
29. P. E. Shaw, A. Ruseckas, I. D. W. Samuel, Exciton diffusion measurements in poly(3-hexylthiophene). *Adv Mater* **20**, 3516 (Sep 17, 2008).
30. A. J. Lewis *et al.*, Singlet exciton diffusion in MEH-PPV films studied by exciton-exciton annihilation. *Organic Electronics* **7**, 452 (Dec, 2006).
31. X. Ai *et al.*, Photoinduced Charge Carrier Generation in a Poly(3-hexylthiophene) and Methanofullerene Bulk Heterojunction Investigated by Time-Resolved Terahertz Spectroscopy. *J. Phys. Chem. B* **110**, 25462 (2006).
32. H. Nemeč *et al.*, Ultrafast conductivity in a low-band-gap polyphenylene and fullerene blend studied by terahertz spectroscopy. *Phys. Rev. B: Condens. Matter Mater. Phys.* **79**, 245326/1 (2009).
33. D. G. Cooke, F. C. Krebs, P. U. Jepsen, Direct observation of sub-100 fs mobile charge generation in a polymer-fullerene film [Erratum to document cited in CA156:286020]. *Phys. Rev. Lett.* **108**, 079901/1 (2012).
34. M. C. Beard, G. M. Turner, C. A. Schmuttenmaer, Transient photoconductivity in GaAs as measured by time-resolved terahertz spectroscopy. *Phys. Rev. B: Condens. Matter Mater. Phys.* **62**, 15764 (2000).

35. T.-I. Jeon, D. Grischkowsky, A. K. Mukherjee, R. Menon, Electrical characterization of conducting polypyrrole by THz time-domain spectroscopy. *Appl. Phys. Lett.* **77**, 2452 (2000).
36. J. Lloyd-Hughes, T.-I. Jeon, A Review of the Terahertz Conductivity of Bulk and Nano-Materials. *J. Infrared, Millimeter, Terahertz Waves* **33**, 871 (2012).
37. F. C. Grozema, P. T. van Duijnen, Y. A. Berlin, M. A. Ratner, L. D. A. Siebbeles, Intramolecular Charge Transport along Isolated Chains of Conjugated Polymers: Effect of Torsional Disorder and Polymerization Defects. *J. Phys. Chem. B* **106**, 7791 (2002).
38. P. Parkinson, J. Lloyd-Hughes, M. B. Johnston, L. M. Herz, Efficient generation of charges via below-gap photoexcitation of polymer-fullerene blend films investigated by terahertz spectroscopy. *Phys. Rev. B: Condens. Matter Mater. Phys.* **78**, 115321/1 (2008).
39. K. P. H. Lui, F. A. Hegmann, Ultrafast carrier relaxation in radiation-damaged silicon on sapphire studied by optical-pump-terahertz-probe experiments. *Appl. Phys. Lett.* **78**, 3478 (2001).
40. T. M. Burke, M. D. McGehee, How high local charge carrier mobility and an energy cascade in a three-phase bulk heterojunction enable >90% quantum efficiency. *Adv. Mater. (Weinheim, Ger.)* **26**, 1923 (2014).
41. O. G. Reid *et al.*, The influence of solid-state microstructure on the origin and yield of long-lived photogenerated charge in neat semiconducting polymers. *J. Polym. Sci., Part B: Polym. Phys.* **50**, 27 (2012).
42. E. V. Fedulova *et al.*, Studying of dielectric properties of polymers in the terahertz frequency range. *Proc. SPIE* **8337**, 833701/1 (2012).





# **CHAPTER SIX**

## **Conclusions**

This thesis presents research work in the context of the recent field of organic photovoltaics (OPV). We have studied bulk heterojunction donor:acceptor blends using conjugated polymers as donors and fullerene derivative PCBM as acceptor. Recently, the research in this field has been focused on the improvement of the efficiency of charge generation and collection by improving the device architecture and the morphology of the active layer. However, the essential problem still remains to understand the photo-physical mechanisms and the time scales of charge generation at the donor:acceptor interface. It has become clear that the microstructure of the bulk heterojunction blends plays a significant role in the photo-physical process of charge generation. Indeed, the dynamics, times and mechanisms of charge generation change according to the microstructure. The way in which the donor and the acceptor arrange in the bulk heterojunction depends on the polymer used, on the temperature of processing and it can be manipulated using processing additives. The characteristic packing of neat polymer chains (amorphous or ordered) plays also a very important role.

In the following, the main findings of the thesis are summarized. The results have been obtained using transient absorption (TA) spectroscopy and THz time domain spectroscopy on neat polymer films and polymer:fullerene samples prepared with two different polymers: more ordered pBTTT and more amorphous PBDTTPD. We have investigated the charge generation dynamics upon selective excitation of either the fullerene (390 nm) or the polymer (540/530 nm). We found a strong correlation of the electron and hole transfer rates, as well as of the subsequent generation of free charges, with the presence of phase-pure regions and intermixed domains. Our work identifies ultrafast spectroscopy as a potential tool to predict the microstructure of blends when it is not previously known.

- **The importance of neat PCBM domains for free charge generation**

In order to understand the mechanism of charge generation at the donor:acceptor interface, it is necessary to investigate the nature and the characteristics of the driving force allowing to separate the interfacial electron-hole pair ("charge transfer state") into free charges no longer bound by the Coulomb force. In order to investigate the role played by neat PCBM domains in this process, a fully intercalated microstructure with a single co-crystalline phase (pBTTT:PCBM in 1:1 weight ratio) has been compared with a two-phase microstructure consisting of the intermixed phase and neat

PCBM domains (pBTTT:PCBM in 1:4 weight ratio). The TA measurements highlight that the majority of interfacial electron-hole pairs are promptly generated within less than 100 fs in the co-crystalline phase, but are recombining in the 1:1 blend following a geminate pathway on the 200 ps time scale. However, in the two-phase microstructure, the presence of long-lived charges could be shown. This is due to the neat fullerene domains, which provide the driving energy to spatially separate the electron-hole pairs. We found that the exciton dissociation in the 1:4 blend had slow components with 390 nm excitation, because the PCBM excitons have to travel through the neat PCBM regions prior to charge separation. However with 530 nm excitation, the electron transfer is prompt in the 1:1 and 1:4 blends. We observed an electro-absorption signature in the TA data as a tool allowing to follow the presence of holes in the co-crystal phase. In the 1:1 and 1:4 microstructures, the holes are remaining in the co-crystal phase until 1000 ps, because there are no neat polymer domains. Finally the neat pBTTT sample was investigated by TA spectroscopy to reveal the behaviour of excitons in the absence of an electron acceptor.

- **The role of the neat pBTTT domains in three-phase microstructures**

The use of fatty acid methyl esters as processing additives of different lengths allows to phase separate the pBTTT:PCBM blends in order to obtain a three-phase morphology. This microstructure category includes 1:1 pBTTT:PCBM blends processed at room temperature, with different amounts of Me 7, or with 1 molar equivalent of Me 12. Differently from the microstructures in the 1:1 and 1:4 blends without processing manipulation, this phase morphology provides the possibility to investigate the case when not only the co-crystal phase and the neat PCBM regions are present, but also neat pBTTT domains, in order to study their role in the process of charge generation. The TA results show that the total efficiency of charge separation is reduced: in fact, some excitons generated in the neat polymer phase recombine before being able to reach the PCBM interface and thus constitute a loss path. However, the neat pBTTT phase, in the same way as the neat PCBM domains, is also contributing positively to provide the driving force to split the electron-hole pairs created at the interface within the co-crystal phase. The electro-absorption signature originating from the Stark effect was present also for the three-phase microstructure. It is a clear signature of the presence of the hole in the co-crystal phase. The time evolution of the electro-absorption is monitoring the migration of the hole from the co-crystal phase to the neat

polymer phase, where the electro-absorption signal is very weak. This process happens in less than 1 ps, thanks to the high nanoscale charge mobility and possibly thanks to tie-molecules (polymer chains extending from the co-crystal phase to the neat phase).

- **Mostly phase-separated samples: importance of the intermixed phase**

The predominantly phase-separated microstructure includes 1:1 pBTTT:PCBM blends processed with 10 molar equivalents of Me 12 or Me 14. These samples have large neat regions of PCBM and neat polymer domains, with only a small amount of intermixed phase. The rate of charge separation in these samples is very low: in fact most excitons have to diffuse large distances to the interface through the neat regions and recombine during this path. This underlines the importance of having intermixed regions for efficient exciton dissociation in the optimal three-phase microstructure, while the PCBM and/or pBTTT domains are necessary for the spatial separation of interfacial electron-hole pairs.

- **Prompt and delayed charge generation in PBDTTPD:PCBM blends**

As the microstructure has turned out to have a determining contribution in exciton diffusion, exciton dissociation, and interfacial electron-hole pair dissociation, we have measured also the PBDTTPD polymer blended with PCBM (in 1:2 weight ratio) in order to confirm our findings. This blend has very high power conversion efficiency and thanks to its low band gap is able to capture a broad part of solar light. Differently from the rather ordered pBTTT, the PBDTTPD polymer chains are more amorphous in neat and in blended samples. Using a 1:2 weight ratio without any further processing manipulation already allows to have a three-phase microstructure: it contains amorphous neat polymer aggregates (about 8 nm diameter), neat fullerene regions (5 nm), and amorphous intermixed domains. In spite of the same microstructure, the mechanism of charge generation is different from that in three-phase pBTTT:PCBM blends. Thanks to the characteristic delocalization and longer lifetime of the excitons generated in the neat polymer regions, the excitons are able to reach a PCBM interface without recombining, yielding efficient delayed charge separation. In the TA results, this mechanism can be visualized as a 1 ps rise of the charge absorption, which is clear only when the pump fluence is really low. The latter experimental condition is needed in

order to avoid bimolecular recombination phenomena. There is also an ultrafast component of charge separation in  $< 100$  fs corresponding to the intermixed phase. The 1 ps rise could be confirmed by transient THz measurements (time resolution of 300 fs), which are more sensitive to detect charges and to identify their nature (bound or free). Moreover, we were able to identify a THz signature for bound excitons in neat PBDTTPD films and to investigate the nature and local mobility of charges in the PBDTTPD:PCBM blend as a function of excitation wavelength, fluence and pump-probe time delay. From the THz measurements it was possible to confirm that the excitons split directly into relatively free charges within the time resolution of the experiment.



# Curriculum Vitae

## PERSONAL INFORMATION

Name: Mariateresa  
Surname: Scarongella  
Place of birth: Terlizzi (Bari)  
Date of birth: February 5<sup>th</sup>, 1982  
Nationality: Italian  
Email address: mariateresa.scarongella@epfl.ch  
Professional address: EPFL SB ISIC GR-MO CH G0 625 (Bâtiment CH)  
Station 6 CH-1015 Lausanne

## EDUCATION

- **2012-2015:** Ph.D project in Prof. J. E. Moser's group, Photochemical Dynamics Group, Ecole Polytechnique Fédérale de Lausanne (EPFL), under the supervision of Prof. Natalie Banerji.
- **2011-2012:** Ph.D project in Majed Chergui's group, LSU EPFL.
- **2009-2010:** Master in Materials Science, Pavia (IUSS Istituto Universitario degli Studi Superiori di Pavia) with an internship at EPFL in the LSU (Ultrafast Spectroscopy Laboratory).
- **2007-2009:** University of Bologna (Italy), Master Degree in Physics.
- **2001-2007:** University of Bari (Italy), Bachelor in Physics.

## RESEARCH PROJECT AND COLLABORATIONS

- **2012-2015: PhD thesis,** Charge carrier dynamics at organic interfaces for polymer photovoltaics
- **Fall 2013:** Collaboration project the Imperial College (London) in Prof. N. Stingelin's group
- **Spring 2010: Master project** on ultrafast optical properties of novel superconductors



## TEACHING EXPERIENCES

- Teaching assistant at EPFL for General Physics I, General Physics II (Bachelor students)

## LIST OF SCIENTIFIC PUBLICATIONS

- Scarongella, M.; De Jonghe-Risse, J.; Buchaca-Domingo, E.; Causa, M.; Fei, Z.; Heeney, M.; Moser, J.-E.; Stingelin, N.; Banerji, N.: A Close Look at Charge Generation in Polymer:Fullerene Blends with Microstructure Control. *J. Am. Chem. Soc.* **2015**, *137*, 2908-2918.
- Scarongella, M.; Paraecattil, A. A.; Buchaca-Domingo, E.; Douglas, J. D.; Beaupre, S.; McCarthy-Ward, T.; Heeney, M.; Moser, J. E.; Leclerc, M.; Frechet, J. M. J.; Stingelin, N.; Banerji, N.: The influence of microstructure on charge separation dynamics in organic bulk heterojunction materials for solar cell applications. *J. Mater. Chem. A* **2014**, *2*, 6218-6230.
- Scarongella, M.; Laktionov, A.; Rothlisberger, U.; Banerji, N.: Charge transfer relaxation in donor-acceptor type conjugated materials. *J. Mater. Chem. C* **2013**, *1*, 2308-2319.
- Yuen, J. D.; Wang, M.; Fan, J.; Sheberla, D.; Kemei, M.; Banerji, N.; Scarongella, M.; Valouch, S.; Pho, T.; Kumar, R.; Chesnut, E. C.; Bendikov, M.; Wudl, F.: Importance of unpaired electrons in organic electronics. *J. Polym. Sci., Part A: Polym. Chem.* **2015**, *53*, 287-293.
- Mansart, B.; Lorenzana, J.; Mann, A.; Odeh, A.; Scarongella, M.; Chergui, M.; Carbone, F.: Coupling of a high-energy excitation to superconducting quasiparticles in a cuprate from coherent charge fluctuation spectroscopy. *Proc. Natl. Acad. Sci. U. S. A.* **2013**, *110*, 4539-4544, S4539/1-S4539/6.
- Brown, M. A.; Huthwelker, T.; Beloqui Redondo, A.; Janousch, M.; Faubel, M.; Arrell, C. A.; Scarongella, M.; Chergui, M.; van Bokhoven, J. A.: Changes in the Silanol Protonation State Measured In Situ at the Silica-Aqueous Interface. *J. Phys. Chem. Lett.* **2012**, *3*, 231-235.

- Conference paper: O. Levrini, P. Fantini., B. Pecori, M. Gagliardi, M . T . Scarongella, G. Tasquier, "A Longitudinal Approach to Appropriation of Science Ideas: A Study on Students' Trajectories in Thermodynamics", Proceedings 9th International Conference of the Learning Sciences, "Learning in the Disciplines", June 29 - July 2, 2010 Chicago, IL.

## **PRESENTATIONS**

### **ORAL PRESENTATION**

- "THz-Time Domain Spectroscopy of Charge Carrier Dynamics in Conjugated Polymers" Physical Chemistry of Interfaces and Nanomaterial's XII-Conference- SPIE , San Diego 2013.

### **POSTER PRESENTATION**

- EPFL Photonics Day, Switzerland, 2011, 2012, 2013, 2014
- NCCR MUST meetings, Switzerland, 2011, 2012, 2013, 2014
- Swiss Chemical Society meetings, Switzerland, 2013



## Acknowledgements

At the end of this path I would like to acknowledge all the people who have supported me in all these years of my PhD. First of all, I'm very thankful to my supervisors Prof. Natalie Banerji and Prof. Jacques-Edouard Moser for giving me the opportunity to enter in the beautiful world of photochemistry and photovoltaics.

I would really like to thank Prof. Natalie Banerji for having me in as the first PhD student in her group. I would like to thank her for supporting me in these years, for her advice, for all the time that she spent for me. Thanks for the scientific and life discussions and for teaching the importance of rigor and accuracy in experimental scientific research as well as a critical approach for the data analysis.

I would like to thank also Prof. Jacques Moser for welcoming me into his group and allowing me to use the laboratory in the Photochemical Dynamics's group. I particularly appreciate his photochemistry lectures, which have fascinated me and encouraged me to continue in the field of photochemistry.

Particular thanks go to Jan Brauer and Ahmad A. Oskouei for their patience in teaching me everything about the THz technique.

I would also like to thank all the people who I worked with in the Photochemical Dynamics Group: Jelissa de Jonghe, Marine Bauduban, Arianna Marchioro, Joël Teuscher, Elham Ghadiri, Yuri Ichinose. Thanks for the scientific and life discussions and for helping me over lasers and technical laboratory problems as well as for sharing nice coffee break moments.

A special thanks goes to Arun and Andrius who shared the office with me and for supporting and encouraging me during the hard moments in the lab.

Special thanks to Prof. Natalie Stingelin, one of the most passionate and enthusiastic people I have met, for welcoming me into her group during the collaboration period in London (Imperial College). Thanks especially to Ester, for all the transmitted knowledge in processing sample techniques and for the scientific discussions.

Thanks to all the lab-mates in Imperial College: Alberto, Irene, Michele, Manuela. Thanks for having been friendly and to have shared nice and convivial moments together.

Thanks to all people in Laboratory of Ultrafast Spectroscopy: Susanne, Gerard, Roberto, Andrè, Cristina and Olivier for all the patience in teaching me chemistry knowledge and to have been friendly and helpful.

Thanks to all the people who emotionally supported me and for their sincere friendship: thanks to Martina who supported me in the last period, to Marta and Giulia who were always available to support me in the difficult moments and for all the life discussions we had together.

Un ringraziamento particolare va alla mia famiglia e in particolare a mio fratello e mi a madre che mi sono stati sempre vicini in questi anni. Ringrazio particolarmente mio padre che mi ha trasmesso il piacere e la bellezza della scienza. Ringrazio anche il gruppo giovani della Rete Loyola, del Poggeschi di Bologna che mi ha incoraggiato a credere nella bellezza della scienza come manifestazione della presenza di Dio ("Grandi sono le opere dell'Eterno, ricercate da tutti coloro che si diletano in esse" Salmo 111). Grazie anche al gruppo della Missione Cattolica Italiana a Losanna per essere stato la mia famiglia qui a Losanna.